# Satellite cloud and precipitation property retrievals for climate monitoring and hydrological applications

**Erwin Wolters**

**ISBN:** 978-90-393-5731-6
**©2012 E.L.A. Wolters**
**Cover picture:** Mixture of clouds in a turbulent late-summer atmosphere on 10 September 2011. The clouds with well-defined edges contain water droplets, while the clouds with feather-like patterns contain ice crystals. Picture taken by author.

# Satellite cloud and precipitation property retrievals for climate monitoring and hydrological applications

Satellietbepalingen van wolken- en neerslageigenschappen ten behoeve van klimaatmonitorings- en hydrologische toepassingen
**(met een samenvatting in het Nederlands)**

**PROEFSCHRIFT**

ter verkrijging van de graad van doctor aan de Universiteit Utrecht op gezag van de rector magnificus, prof. dr. G.J. van der Zwaan, ingevolge het besluit van het college voor promoties in het openbaar te verdedigen op

donderdag 29 maart 2012 des middags te 2.30 uur.

door

**Erwin Leonardus Antonius Wolters**

geboren op 1 februari 1976 te Roermond

**Promotor:** Prof. dr. ir. B. J. J. M. van den Hurk

**Co-promotor:** Dr. ir. R. A. Roebeling

The work presented in this thesis was funded through EUMETSAT's Climate Monitoring Satellite Application Facility (CM-SAF) and ESA's Water Cycle Multi-Mission Observation Strategy (WACMOS, contract number 22086/08/I-EC).

# Contents


**Samenvatting** **v**

**1 Introduction** **1**
1.1 Climate and climate change 1
1.2 Clouds in the climate system 3
1.2.1 The role of clouds in the radiation budget 3
1.2.2 The role of clouds in the hydrological cycle 4
1.3 Satellite remote sensing of clouds and precipitation 6
1.4 This thesis 8

**2 Theory, data, and retrieval algorithms** **11**
2.1 Theory 11
2.1.1 Radiative transfer in a cloudy atmosphere 11
2.1.2 Radiative transfer models 16
2.1.3 Precipitation formation theory 17
2.2 Data 18
2.2.1 Spinning Enhanced Visible and Infrared Imager (SEVIRI) 19
2.2.2 Moderate-Resolution Imaging Spectroradiometer (MODIS) 19
2.2.3 Tropical Rainfall Measurement Mission - Precipitation Radar (TRMM-PR) 20
2.2.4 Advanced Microwave Scanning Radiometer - Earth Observing System (AMSR-E) 21
2.3 Retrieval algorithms 21
2.3.1 Reflectance Lookup Tables 21
2.3.2 Cloud detection algorithm 22
2.3.3 Retrieval of cloud physical properties (CPP) 23
2.3.4 Precipitation Properties retrieval algorithm (CPP-PP) 25

**3 SEVIRI cloud-phase retrieval evaluation using ground-based observations** **27**
3.1 Introduction 28
3.2 Cloud-phase determination algorithms 30
3.2.1 Satellite algorithms 30
3.2.2 Cloud-phase determination from ground-based measurements 33

| | | |
|---|---|---|
| 3.3 | Data and methods | 35 |
| 3.3.1 | Satellite data analysis | 35 |
| 3.3.2 | Ground-based data analysis | 36 |
| 3.3.3 | Comparison of satellite to ground-based cloud-phase observations | 37 |
| 3.4 | Results | 40 |
| 3.4.1 | Instantaneous cloud-phase retrievals | 40 |
| 3.4.2 | Monthly liquid water and ice cloud occurrence frequency | 41 |
| 3.4.3 | Daytime diurnal cycle of cloud phase | 45 |
| 3.5 | Conclusions | 46 |
| **4** | **Broken and inhomogeneous cloud impact on satellite cloud property retrievals** | **49** |
| 4.1 | Introduction | 50 |
| 4.2 | Data and methods | 52 |
| 4.2.1 | MODIS data | 52 |
| 4.2.2 | CPP retrieval algorithm | 53 |
| 4.2.3 | Synthetic datasets | 55 |
| 4.2.4 | Aggregation of MODIS observations | 58 |
| 4.3 | Results | 59 |
| 4.3.1 | Description of observed cloud-type occurrence over ATL and EUR | 59 |
| 4.3.2 | Simulations with synthetic data | 61 |
| 4.3.3 | MODIS observations | 64 |
| 4.4 | Discussion and conclusions | 68 |
| **5** | **SEVIRI precipitation retrieval evaluation over West Africa using TRMM-PR and CMORPH** | **71** |
| 5.1 | Introduction | 72 |
| 5.2 | Data and methods | 75 |
| 5.2.1 | CPP-PP precipitation retrieval technique | 75 |
| 5.2.2 | Precipitation retrieval from TRMM-PR | 76 |
| 5.2.3 | CMORPH precipitation retrieval technique | 76 |
| 5.2.4 | Evaluation of SEVIRI precipitation intensities | 77 |
| 5.2.5 | Evaluation of the monsoon progression over West Africa | 79 |
| 5.3 | Results | 80 |
| 5.3.1 | Validation of SEVIRI precipitation retrievals with TRMM-PR | 80 |
| 5.3.2 | Monitoring of the monsoon progression | 82 |
| 5.3.3 | Daytime diurnal cycle of precipitation | 88 |
| 5.4 | Summary and conclusions | 90 |
| **6** | **A soil moisture–precipitation feedback study over West Africa** | **93** |
| 6.1 | Introduction | 93 |
| 6.2 | Soil moisture and precipitation datasets | 95 |
| 6.2.1 | CPP-PP retrieval algorithm | 95 |
| 6.2.2 | AMSR-E soil moisture retrieval algorithm | 96 |
| 6.2.3 | Data analysis | 97 |

6.3 Results 99
6.4 Discussion and conclusions 100

**7 Perspectives 103**
7.1 Algorithm improvements 104
7.2 Applications 106

**Summary 109**

**Bibliography 113**

**Dankwoord 131**

**Curriculum vitae 135**

# Samenvatting

Wolken spelen een belangrijke rol in de stralingsbalans en hydrologische cyclus op aarde. Het kortgolvige deel van het spectrum van de zonnestraling wordt door wolken effectief gereflecteerd en zorgt voor een koelend effect. Uitgaande langgolvige straling vanaf het aardoppervlak wordt door wolken vastgehouden en dit resulteert in een verwarmend effect. Wolken dragen daarnaast bij aan het horizontale en verticale transport van waterdamp en verdampingswarmte. In grote delen van de wereld is de ruimtelijke schaal waarop wolken- en neerslageigenschappen vanaf de grond worden gemeten onvoldoende om de gewenste nauwkeurigheid te kunnen waarborgen. Nauwkeurige en wereldwijde metingen zijn nodig om te kunnen bepalen of genoemde eigenschappen op enige termijn veranderen binnen het veranderende klimaatsysteem. Geostationaire satellieten zijn geschikt om nauwkeurige metingen aan wolken en neerslag te verrichten. Uiteindelijk kunnen datasets van wolken- en neerslageigenschappen gebruikt worden voor het evalueren van wolkenparameterisaties in weer- en klimaatmodellen, het onderzoeken van land–atmosfeerinteracties en het detecteren van veranderingen in de dagelijkse gang van wolken en neerslag.

Dit proefschrift beschrijft de afleiding, evaluatie en toepassing van de thermodynamische fase, wolkendeeltjesgrootte, neerslagfrequentie en -intensiteit uit metingen van gereflecteerde zonnestraling in het visuele en nabij-infrarode deel van het zonnespectrum door middel van het op het KNMI ontwikkelde Cloud Physical Properties (CPP) algoritme. Het algoritme wordt voor het grootste gedeelte toegepast op reflectanties gemeten door de Spinning Enhanced Visible and Infrared Imager (SEVIRI), die zich op de geostationaire Meteosat Second Generation (MSG) satellieten bevindt. De reflectanties worden elke 15 minuten gemeten met een ruimtelijke resolutie variërend van $3\times3$ km$^2$ boven Centraal-Afrika tot ongeveer $4\times7$ km$^2$ boven West-Europa, waardoor ontwikkelingen zoals dagelijkse gang van wolken- en neerslageigenschappen te volgen zijn.

Hoofdstuk 1 beschrijft een algemeen overzicht van het veranderende klimaat en verduidelijkt de invloed van wolken op het klimaat. Een aantal terugkoppelingsmechanismen in het klimaatsysteem, zoals de invloed van een stijgende temperatuur op wolken en atmosferisch waterdamp worden uitgelegd. Verder wordt in dit hoofdstuk ook het belang van wolken in de hydrologische cyclus besproken. Tot slot worden de te beantwoorden onderzoeksvragen van dit proefschrift geformuleerd.

De theorie die ten grondslag ligt aan de afleiding van wolken- en neerslageigenschappen uit gemeten reflectanties en de gebruikte methodieken voor het in dit proefschrift uitgevoerde onderzoek worden in Hoofdstuk 2 uitgelegd. Het hoofdstuk begint met de uitleg van stralingstransport door de aardse atmosfeer en wolken en een kort overzicht van een aantal modellen om dit stralingstransport te berekenen. Vervolgens worden de verschillende satellietinstrumenten die in dit proefschrift zijn gebruikt besproken. Tot slot wordt het CPP-algoritme, dat wordt gebruikt om vanuit gemeten reflectanties de wolken- en neerslageigenschappen te bepalen, uitgelegd.

Hoofdstuk 3 beschrijft de evaluatie van verschillende satellietmethoden voor de bepaling van wolkenfase. Deze evaluatie is uitgevoerd door de wolkenfase te vergelijken met een dataset van wolkenfase bepaald vanaf het aardoppervlak bij Cabauw. Aangezien SEVIRI voornamelijk gevoelig is voor de gereflecteerde zonnestraling vanaf de wolkentop en de instrumenten aan het aardoppervlak de gehele wolkenkolom observeren, moest een correctie op de grondwaarnemingen worden toegepast. De nauwkeurigheid en precisie van de CPP-wolkenfasebepalingen zijn voor alle methoden respectievelijk ongeveer 5% en 10%. Verder is het vermogen voor het volgen van de opbouw van ijswolken tijdens het West-Europese zomerseizoen voor elk van de methoden onderzocht. Het blijkt dat alle gebruikte methoden hiertoe in staat zijn.

Hoofdstuk 4 bespreekt de invloed van gebroken wolkenvelden op de afleiding van de wolkendeeltjesgrootte bij verschillende ruimtelijke meetresoluties. Hiertoe zijn bij verschillende wolkenfracties zowel simulaties van de bepaling van wolkendeeltjesgrootte als bepalingen uit waargenomen Moderate-Resolution Imaging Spectroradiometer (MODIS) reflectanties uitgevoerd. Het blijkt dat de afgeleide wolkendeeltjesgrootte bij lage resolutie voor gebroken wolkenvelden met ongeveer 5 $\mu$m kan worden overschat ten opzichte van de bepaling bij hoge resolutie. De grootste overschattingen komen voor boven oceaanoppervlakken, omdat hier het contrast tussen oppervlakte- en wolkenreflectantie het grootste is. Het effect van een te hoge afgeleide wolkendeeltjesgrootte kan ook leiden tot een verkeerd afgeleide wolkenfase.

In Hoofdstuk 5 zijn de uit SEVIRI-reflectanties afgeleide neerslageigenschappen vergeleken met neerslagobservaties uit andere satellietinstrumenten en met regenmeters op het aardoppervlak. Het onderzoek heeft zich gericht op West-Afrika. Deze regio kenmerkt zich door een afwisseling van droge en natte perioden, de West-Afrikaanse moesson. Uit de vergelijkingen blijkt dat de neerslagfrequentie en -intensiteit die is afgeleid een nauwkeurigheid heeft die voldoende is om de ontwikkeling van neerslag voor periodes van een dag tot een seizoen te monitoren.

Hoofdstuk 6 beschrijft het gebruik van een satellietafgeleide bodemvocht- en neerslagdataset voor het onderzoeken van een aardoppervlak–atmosfeerinteractie. Voor West-Afrika is de samenhang tussen bodemvocht en het optreden van neerslag gedurende de moesson onderzocht. Op basis van gemeten bodemvocht werden dagelijks droge van natte bodems onderscheiden, waarna de boven deze gebieden door SEVIRI geobserveerde neerslagfrequentie en -intensiteit van de volgende dag met elkaar zijn vergeleken. Boven zowel droge als natte bodems nemen neerslagfrequentie en -intensiteit gedurende de dag toe, wat op basis van

toenemende instraling in combinatie met atmosferische onstabiliteit mag worden verwacht. Echter, de neerslagfrequentie boven droge bodems is in de middag significant hoger dan boven natte bodems. Een mogelijke verklaring hiervoor is een grotere hoeveelheid voelbare warmte, die in combinatie met voldoende waterdamp hoger in de atmosfeer kan leiden tot diepere convectie en bijgevolg meer buienvorming.

De belangrijkste conclusies van dit proefschrift zijn samengevat in Hoofdstuk 7. Tevens zijn een aantal aanbevelingen voor verbeteringen aan het CPP-algoritme en mogelijke toepassingen van de uit SEVIRI-metingen afgeleide satellietwolkendatasets in toekomstig onderzoek gegeven. Mogelijke verbeteringen zijn het toevoegen van een methode waarmee ook 's nachts wolkenfase, neerslagfrequentie en -intensiteit kan worden afgeleid. Hiermee kan de volledige dagelijkse gang van wolkenfase en neerslag bestudeerd worden. Daarnaast kan het algoritme verbeterd worden door het corrigeren van de wolkendeeltjesgroottebepaling bij gebroken wolkenvelden. Hiervoor kan gebruik worden gemaakt van het SEVIRI High-Resolution Visible (HRV) kanaal. Toepassingen van de afgeleide wolken- en neerslagdatasets liggen onder andere in het monitoren van veranderingen in genoemde eigenschappen over lange tijd, de ondersteuning voor meteorologen in het maken van weersverwachtingen, onderzoek van de waterbalans aan het aardoppervlak, van land–atmosfeerinteracties en assimilatie in weer- en klimaatmodellen. Vooral de hoge tijds- en ruimtelijke resolutie van het SEVIRI-instrument geven hierbij een grote toegevoegde waarde.

# Chapter 1

## Introduction

### 1.1 Climate and climate change

The way humans arrange their lives and their societies has been and still is for a large part imposed by the climate. As weather has a very tangible meaning to people, the meaning of "climate" is more abstract. It is mostly defined as the average weather over a time period of 30 years or more, supposed to be long enough to average out year-to-year fluctuations and short enough not to be influenced by any long-term trend.

Obviously, global climate has not been constant throughout time. It has been subject to fluctuations resulting from external forcings, such as changes in the Earth's orbital parameters, the most important of them being the periodical change of the Earth's axial tilt and precession. However, these changes take place at time scales of 10,000–100,000 years. Another external forcing is the change in solar activity, which acts on time scales in the order of one hundred years. For example, the relatively cold period during the largest part of the 17th century has likely been caused by low solar activity (Lockwood et al. 2010; Yamaguchi et al. 2010).

In the latter part of the 20th century, climate has rapidly changed due to the increase of various anthropogenic greenhouse gas emissions, most particularly carbon dioxide ($CO_2$), methane ($CH_4$), and nitrous oxide ($N_2O$), as stated by the Intergovernmental Panel on Climate Change (IPCC) in their fourth Assessment Report [AR4, Solomon et al. (2007)]. Global warming resulting from the increase in $CO_2$ concentration and the subsequent enhanced greenhouse effect was already predicted by Arrhenius (1896). One of the first reliable estimates on the $CO_2$-induced increase in global mean temperature was reported to be about 0.05 K per decade by Callendar (1938). However, by 2010, the global-mean temperature had increased by 0.8 K relative to the late 19th century (see Figure 1.1) and warming presently continues at a rate of about 0.2 K per decade (Hansen et al. 2010).

The implications of a continuous increase in global-mean temperature are manyfold. As the polar regions have the largest susceptability to an increase in global-mean temperature, the extent of the Arctic sea ice and Greenland ice sheet rapidly decreases.

Especially the Arctic sea ice extent has sharply decreased during the last decades and model simulations have shown that an ice-free Arctic summer could be possible from about 2030 onwards (Wang and Overland 2009).

A warming climate also implies that water vapor will be more abundant in the atmosphere, as the water-holding capacity increases with temperature. From the so-called Clausius-Clapeyron relation it follows that per degree temperature change the amount of water vapor increases by ≈7%. On a global scale, it has been shown through modeling efforts that the amount of precipitation increases by only 2-3% (Held and Soden 2006; Stephens and Hu 2010), which was recently confirmed by global precipitation observations (Arkin et al. 2010). However, on a regional scale and at temperatures exceeding 20°C extreme rain intensities could increase by even more than 15% $K^{-1}$ (Lenderink and van Meijgaard 2010).

An important aspect in climate research is the uncertainty associated with various climate feedback mechanisms. From the increase in global-mean temperature resulting from the enhanced greenhouse effect, myriad feedback mechanisms come into play. These feedback mechanisms may either strengthen or diminish the initial temperature increase and are referred to as positive and negative feedback, respectively. For example, due to the temperature increase more water will evaporate from the surface and is thereby added to the atmospheric water vapor burden. Because water vapor itself absorbs the outgoing longwave terrestrial radiation, this water vapor increase enhances the temperature increase (positive feedback). On the other hand, part of the extra water vapor added to the atmosphere will condensate into clouds, which may dampen the temperature increase, because of the increased reflectance of incoming solar radiation (negative feedback). At present, not all of the various feedback mechanisms are entirely understood, nor is their impact on the climate system quantified with sufficient accuracy. In addition, the feedback mechanisms affecting clouds, radiation, and various land surface characteristics are mutual relationships, which adds to the complexity of climate research.

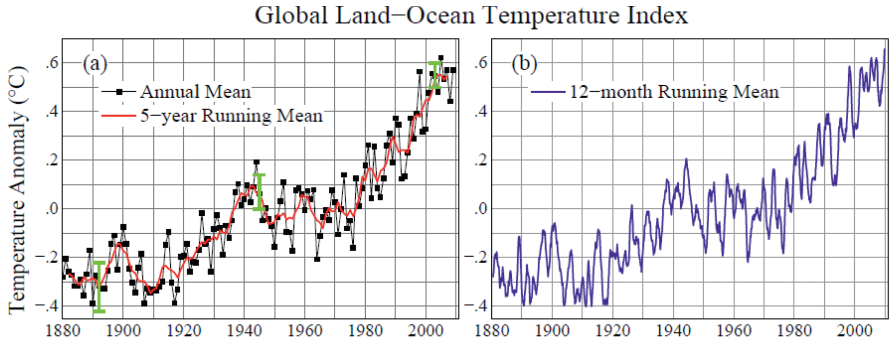


**Figure 1.1** *Global surface temperature anomalies relative to the 1951–1980 mean for (a) annual (black line) and 5-year (red line) running means through 2009 and (b) 12- month running mean using data through June 2010. Green bars denote 2σ error estimates. From Hansen et al. (2010).*

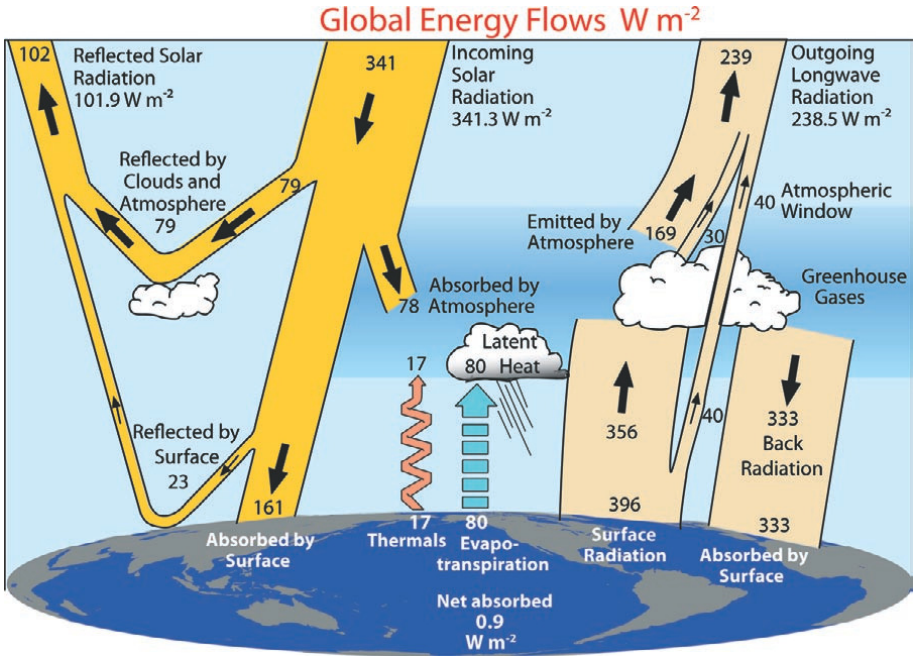


**Figure 1.2** *The global annual mean Earth's energy budget for March 2000–May 2004. From Trenberth et al. (2009).*

## 1.2 Clouds in the climate system

### 1.2.1 The role of clouds in the radiation budget

Clouds govern the radiation budget of the Earth-atmosphere system by playing a role in both the shortwave and longwave spectrum. The difference between the top-of-atmosphere (TOA) net radiation for clear-sky and cloudy situations is generally referred to as cloud radiative forcing (clear sky minus cloudy). It can be decomposed into a shortwave and a longwave component.

Figure 1.2 shows the main components of the Earth energy budget, with the arrows on the left- and righthand side representing the shortwave and longwave components, respectively. The amount of solar energy received by the Earth at the top of atmosphere (TOA) is about 1366 W $m^{-2}$ (Liou 2002). As the area of the Earth is four times its projected area, the amount of solar irradiance at TOA is 341 W $m^{-2}$. About 79 W $m^{-2}$ of the total incoming radiation is reflected by clouds and atmospheric molecules, while about the same amount is absorbed, mainly by oxygen ($O_2$), ozone ($O_3$), water vapor ($H_2O$), and carbon dioxide ($CO_2$). The total amount of solar energy being reflected by the atmosphere and the Earth's surface is about 30% (Kiehl and Trenberth 1997), and is generally referred to as the planetary albedo. The averaged amount of solar energy received at the surface is 161 W $m^{-2}$.

Because the Earth–atmosphere system is in an equilibrium, the amount of net incoming shortwave energy should be equalled by the amount of outgoing longwave energy. This energy is transferred to the atmosphere through convection (thermals), evapotranspiration, and absorption of outgoing terrestrial radiation by clouds and atmospheric gases. In turn, the absorbed energy by the atmosphere is radiated to both the surface and outer space. As can be seen in Figure 1.2, atmospheric gases account for the largest part of the outgoing longwave emission (169 W $m^{-2}$). Clouds emit an amount of energy comparable to the atmospheric window emission (about 40 W $m^{-2}$). However, the modeled and observed estimates of longwave emission by clouds differ.

In general, warm, low-level clouds, which are mostly composed of water droplets, have a negative shortwave cloud radiative forcing due to their reflection of incoming shortwave solar radiation (Arking 1991; Hansen et al. 1997). However, the impact of these clouds on the longwave radiation balance is only marginal, because their temperature, and thus the amount of longwave radiation emitted to space, does not differ much from the surface temperature. Large amounts of water clouds are found in the subtropics west of the continents. These cloud areas cover about 8% of the Earth's surface (Karlsson et al. 2008) and are thus of significant importance to the global energy balance. However, Global Climate Models (GCMs) do not always accurately predict both the low-level cloud fraction and the accompanying cloud radiative forcing of these clouds (Karlsson et al. 2008).

High, cold (cirrus) clouds, which are located at heights of ~10 km or higher, have a positive (warming) effect on the radiation budget by absorbing and re-emitting outgoing longwave terrestrial radiation back to the surface. The higher ice clouds are located in the atmosphere, the larger their impact on the longwave radiation budget, because the amount of outgoing longwave radiation to space is reduced compared to a clear sky situation. In contrast, the presence of cirrus clouds causes a warming of the surface and atmosphere, because the amount of re-emitted radiation is larger than for a clear sky situation. Ice clouds are abundant in tropical convective systems (anvils) and in mid-latitude frontal weather systems.

From the above it follows that identification of the cloud thermodynamic phase of clouds is important to assess the effect of clouds to the radiation budget. Water droplets and ice crystals have different scattering and absorption properties, which implies a different shortwave transmission and longwave radiation absorption/emission. In the shortwave spectrum, water droplets scatter the incident radiation more forward than ice crystals, while in the longwave spectrum water droplets absorb and re-emit radiation less efficiently compared to ice crystals.

### 1.2.2 The role of clouds in the hydrological cycle

Clouds are also an important factor in the hydrological cycle. They are generated through the transition of water from the gaseous to the liquid or solid state (condensation). As a consequence, latent heat is released, which warms the surrounding air and in turn stabilizes the atmosphere. In contrast, the surrounding air is cooled if clouds evaporate, thereby destabilizing the atmosphere.

Therefore clouds not only play a role in the horizontal and vertical water transport, but also in the latent heat transport. When the condensated water precipitates to the surface, clouds have acted as a recycler of water, although the majority of the water evaporated is advected at least 100 km before it precipitates (Douville et al. 2002). In addition, if precipitation evaporates before reaching the surface, which may add up to ~40% depending on among others cloud base height and below-cloud relative humidity (Rosenfeld and Mintz 1988), the surrounding air is cooled. The various components and estimates of the exchange and storage terms within the hydrological cycle are presented in Figure 1.3.

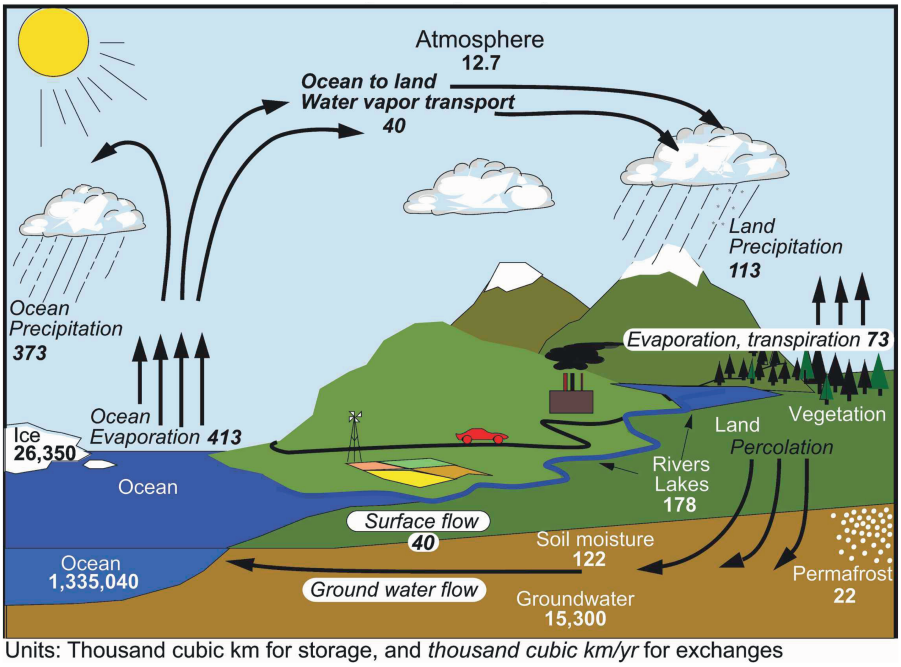


**Figure 1.3** *Schematic representation of the hydrological cycle. Estimates of the main water reservoirs and the flow of moisture through the sytem are given in $10^3$ $km^3$ and $10^3$ $km^3$ $yr^{-1}$, respectively. From Trenberth et al. (2007).*

As for the effect on cloud physical properties, a warming climate also has an impact on the hydrological cycle. A direct effect of higher temperatures is enhanced evaporation, as the atmosphere can contain more water vapor at higher temperatures. On time scales in the order of an hour, evaporation and precipitation are expected to increase in the order of 10% $K^{-1}$ or more (Allan and Soden 2008; Lenderink and van Meijgaard 2008). However, more evaporation also leads to an increased cloudiness. The latter will cause a decrease in the amount of net radiation reaching the surface and subsequently a decrease in evaporation.

## 1.3 Satellite remote sensing of clouds and precipitation

In order to obtain accurate information on the role of clouds in the climate system and the hydrological cycle, its properties need to be measured. Due to clouds' large variability in both time and space, they need to be observed at a sufficient temporal and spatial resolution. Satellites are capable of regularly sampling a given location at the Earth at least once a day. They have already been exploited for more than 50 years in supporting meteorologists on a qualitative basis for making their weather forecasts, starting with the Television Infrared Observation Satellite 1 (TIROS-1) in 1960. It was not until the late 1970s that ideas to study clouds more quantitatively were conceived. As a result, over the last three decades various efforts were taken to compose satellite-based long-term cloud property datasets.

With a history of continuous cloud observations from 1981 onwards, the Advanced Very High Resolution Radiometer (AVHRR) onboard the National Oceanic and Atmospheric Administration (NOAA) satellites was the first instrument to enable the retrieval of cloud properties at a high spatial resolution (1×1 km) using observed reflectances and radiances from five channels within the spectral range 0.6-12.0 $\mu$m. The AVHRR Pathfinder Atmospheres Extended project [PATMOS-x, Jacobowitz et al. (2003)] solely uses AVHRR data to construct global cloud climatologies from 1981 onwards, thereby recalibrating the observed radiances of the various AVHRR instruments and correcting for drifts in equator overpass times. Another large effort to construct accurate and long-term cloud climatologies has come from the International Satellite Cloud Climatology (ISCCP) project (Rossow and Schiffer 1999; Schiffer and Rossow 1983), which uses radiances observed from both polar orbiting and geostationary satellites to obtain global cloud climatologies at a 3-hourly temporal and ~280×280 km spatial resolution.

Recently, the development of more sophisticated radiometer instruments, enabling observations mainly at a higher spectral resolution, have been utilized. An example is the Moderate-Resolution Imaging Spectroradiometer (MODIS) on the Terra (1999) and Aqua (2002) NASA Earth Observing System (EOS) satellites. MODIS observes the Earth using 36 spectral channels in the range 0.4–14.4 $\mu$m with a nominal spatial resolution of 1×1 km$^2$ and even better for the channels in the visible spectral range. From the MODIS-observed radiances, different cloud physical property climatologies are made by various research groups, using separate and well-developed retrieval algorithms [e.g. Minnis et al. (2003); Platnick et al. (2003)].

In 2002 and 2005, two satellites of the Meteosat Second Generation (MSG) series operated by the European Organization for the Exploitation of Meteorological Satellites (EUMETSAT) were launched. These satellites carry the Spinning Enhanced Visible and Infreared Imager [SEVIRI, Schmetz et al. (2002)], which enables to date the highest possible temporal and spatial sampling, which, in combination with an increased number of narrowband spectral channels, enables detailed quantitative studies on clouds.

With the launch in 2006 of the Cloud Profiling Radar (CPR) and the Clouds and Aerosol Lidar with Orthogonal Polarization (CALIOP) onboard the Cloudsat and Calipso satellites, respectively (Stephens et al. 2002), a new era in cloud research from space was started.

The CPR and CALIOP instruments enable detailed vertical profile information of clouds and aerosols using active remote sensing instruments (radar and lidar), rather than obtaining cloud-top information from passively observed radiances. Despite the ability to observe clouds from space actively, this advantage of CPR and CALIOP is counterpointed by both a limited lifetime and a limited spatial coverage compared to passive satellite instruments.

The retrieval of precipitation occurrence and precipitation intensity from passive satellite imagery has been researched since the 1970s. The first retrieval schemes relied on thermal infrared (TIR) radiances and were based on the assumption that clouds start to precipitate if the thermal infrared brightness temperature (BT) becomes lower than a certain threshold value. This principle is generally referred to as Cold Cloud Duration technique (CCD). The rationale is that precipitation is more likely to occur if ice crystals are abundant in the cloud top, because the saturation vapor pressure of ice crystals is lower than that of water droplets (Pruppacher and Klett 1997). However, the relation between BT and precipitation intensity is indirect, because e.g. thick cirrus clouds have low temperatures, but generally do not produce any (surface-observed) rain. This overestimation due to attributing rain rates to non-precipitating cirrus is partly compensated for by an underestimation of rain rates from shallow convection.

Various rainfall retrieval techniques have been based on thermal infrared temperatures only, mostly using the 10–12 $\mu$m atmospheric window spectrum (Adler and Negri 1988; Arkin and Meisner 1987; Ba and Gruber 2001; Negri and Adler 1993; Negri et al. 1984). Most CCD techniques are calibrated locally or regionally with rain gauge and/or passive microwave (PMW) data to obtain an optimum accuracy. Such a calibration is for example used by Huffman et al. (2001) in their Global Precipitation Climatology Project One-Degree Daily (GPCP-1DD) product. Recently, Behrangi et al. (2009) emphasized that combining water vapor channel information with TIR radiances can significantly improve the accuracy in retrieving rain occurrence and intensity from SEVIRI.

During the last decade, the development of precipitation retrieval algorithms has more focused on incorporating information from multiple satellite sensors and combinations of visible, TIR, and passive microwave (PMW) brightness temperatures, with the latter being largely dependent on the emission–absorption process of hydrometeors. For example, the TRMM Multi-Satellite Precipitation Algorithm [TMPA, Huffman et al. (2007)] combines data from PMW imaging, sounding instruments, and geostationary-observed TIR radiances to obtain a single precipitation product. In the Climate Prediction Center Morphing Technique [CMORPH, Joyce et al. (2004)], TIR radiances are used to advect/morph cloud systems between two consecutive PMW instrument overpasses to obtain intermediate rain rate estimates. The Precipitation Estimation from Remotely Sensed Information using Artificial Neural Networks [PERSIANN, Hsu et al. (1997); Sorooshian et al. (2000)] system is a computer-based neural network algorithm that uses both visible reflectances and infrared brightness temperature of clouds from geostationary satellites as the basic input variables to retrieve surface precipitation intensity.

In this thesis, mainly observations from the SEVIRI on the MSG satellites are used to retrieve information on cloud physical properties and precipitation. The retrievals are performed using the Cloud Physical Properties (CPP) algorithm developed at KNMI which uses visible and near-infrared reflectances. A detailed description of the instrument characteristics, its spectral channels, and the CPP retrieval algorithm will be given in Chapter 2.

## 1.4 This thesis

The research performed in this thesis focuses on the retrieval of cloud phase, cloud particle effective radius, and precipitation from passive satellite imagery. The former two cloud properties largely determine the onset of precipitation. For clouds that do not contain any ice in the cloud top, water droplets need to exceed a certain critical size before falling to the surface (Rosenfeld and Gutman 1994). If ice is present in the cloud top, the precipitation formation process becomes more efficient.

Therefore the first part of this thesis focuses on cloud phase and cloud particle effective radius. In order to properly determine whether clouds are precipitating, their thermodynamic phase needs to be accurately determined. Subsequently, the sensitivity of cloud particle size and cloud-phase retrievals to broken and inhomogeneous clouds is of importance, because precipitating clouds are often of inhomogeneous nature.

Cloud-phase, cloud particle effective radius, and condensed water path information are then used to infer if clouds are precipitating and if so, what the precipitation intensity is. These precipitation retrievals are evaluated against several reference datasets to assess whether the retrievals are of sufficient accuracy.

Finally, a precipitation dataset obtained from SEVIRI reflectance measurements is used to investigate the relation between soil moisture and convective activity over the Sahel region in West Africa. This area has been chosen for several reasons. First, this area is very sensitive to year-to-year changes in precipitation, due to its location at the northernmost latitudinal reach of the West African Monsoon. Second, a steep soil moisture gradient exists in this region, with a corresponding change in vegetation. Lastly, the SEVIRI viewing geometry and pixel resolution over the Sahel region are nearly optimal for studying cloud processes in this area.

In connection to the above, the following research questions addressed in this thesis are:

1) Is the CPP cloud-phase retrieval of sufficient accuracy and precision to construct reliable long-term cloud-phase climatologies for mid-latitude coastal climates?

2) What is the impact of different horizontal resolutions to the retrieval of cloud particle effective radius and cloud phase using CPP?

3) Is the accuracy of precipitation occurrence frequency and precipitation intensity as retrieved from CPP sufficient to monitor the seasonal monsoon progression and the rainfall dynamics

at sub-daily scale over West Africa?

4) Is there a significant difference in the precipitation occurrence frequency and intensity over wet and dry surfaces during the West African Monsoon?

Therefore the main aim of this thesis is to compose cloud-phase and precipitation datasets and to evaluate their accuracy for assessing the effect of clouds on the radiation and hydrological balance. It is noted that the actual assessment of the net effect on these balances is beyond the scope of this thesis and will be subject of future research.

The thesis is outlined as follows. Chapter 2 discusses the Earth's energy balance and highlights the radiative transfer in the atmosphere, as well as the retrieval principle of the various cloud physical properties relevant to this thesis.

The first research question, the evaluation of one year of cloud-phase retrievals with ground-based cloud radar and lidar cloud-phase observations is addressed in Chapter 3. It is demonstrated that the accuracy and precision of the CPP cloud-phase retrieval algorithm are best during the summer half-year and that during summer the daytime evolution of convection, i.e., the development from water clouds into ice clouds, can be well followed.

The research on the effect of a variable satellite sensor resolution on the retrieval of cloud particle effective radius and cloud phase is presented in Chapter 4. It is shown from both theoretical calculations and real observations at various satellite sensor resolutions that the cloud particle effective radius and to a lesser extent cloud-phase retrieval are affected by the presence of partially cloud-filled and inhomogeneous overcast satellite pixels.

The evaluation of precipitation retrievals over West Africa during the monsoon season is outlined and discussed in Chapter 5 using precipitation observations from other satellite platforms as reference. Furthermore, the ability of the CPP precipitation retrieval algorithm to monitor both the seasonal progression of the West African Monsoon and the daytime evolution of precipitation intensity is highlighted.

An investigation on the interaction between soil moisture and convection over the Sahel region in West Africa is presented in Chapter 6. This investigation is performed using the cloud-phase and precipitation retrievals from SEVIRI reflectances, as well as soil moisture observations from the Advanced Microwave Scanning Radiometer - Earth Observing System (AMSR-E).

Finally, Chapter 7 reflects on the current status of satellite cloud research and its applications and provides some recommendations for future research directions on among others land surface–atmosphere interactions and climate model evaluation.

# Chapter 2

## Theory, data, and retrieval algorithms

This Chapter presents an overview of the theoretical framework that is used for the retrieval of cloud physical and precipitation properties from satellite-observed radiances. First, the concepts of radiative transfer as well as the models that solve the radiative transfer equation are highlighted. Second, the theory of precipitation formation is shortly touched upon. Finally, detailed information on the satellite instruments used in this thesis is presented, concluded with a description of the Cloud Physical Properties (CPP) and Precipitation Properties (CPP-PP) algorithms.

### 2.1 Theory

#### 2.1.1 Radiative transfer in a cloudy atmosphere

The sun constantly emits electromagnetic radiation into all directions. This electromagnetic energy is carried through photons. The photons radiated by the sun interact in various ways with the Earth's atmosphere. On their way to the surface, photons can be either scattered or absorbed by various atmospheric constituents, such as water droplets or ice crystals, with typical sizes of ~10-30 $\mu$m and up to 100 $\mu$m, respectively. Other atmospheric constituents are the atmospheric molecules ($N_2$, $O_2$, and $H_2O$, with sizes ~$10^{-4}$ $\mu$m) and aerosol particles (size ~1 $\mu$m). At visible wavelengths, scattering is the dominant radiative process, while in the thermal solar infrared radiation is mostly absorbed and emitted.

*Scattering of incident sunlight by clouds*

The scattering of sunlight is a physical process taking place at all wavelengths, in which a cloud particle continuously abstracts energy from the incident beam of sunlight and reradiates this energy into all directions. Because in the visible spectrum scattering is dominant over absorption, photons are scattered numerous times before leaving a cloud. The amount of scattering events within a cloud is largely dependent on both cloud microphysics, such as the particle shape, and macrophysics, such as the amount of particles (optical thickness). The scattering and absorption of sunlight by atmospheric particles over a distance $ds$ is mathematically described by the radiative transfer equation:

$$\frac{dI_\lambda}{k_{\lambda,ext}ds} = -I_\lambda + J_\lambda, \tag{2.1}$$

in which $I_\lambda$ is the intensity of radiation at wavelength $\lambda$, $k_{\lambda,ext}$ is the volume extinction coefficient for radiation of wavelength $\lambda$, and $J_\lambda$ the source function. The latter can be physically interpreted as the increase in radiation intensity resulting from emission and multiple scattering.

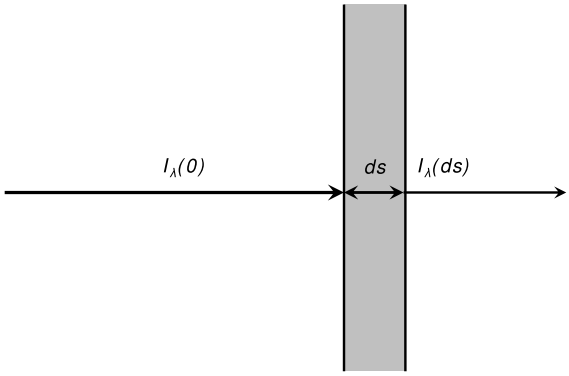


**Figure 2.1** *The principle of the Beer-Bouguer-Lambert law; a beam of electromagnetic radiation passes through a medium, extinction outside the medium is neglected for simplicity.*

Neglecting the diffuse radiation from multiple scattering, $J_\lambda$, the solution of Equation 2.1 leads to the Beer-Bouguer-Lambert law, which describes the intensity of a beam of direct sunlight with intensity $I_\lambda(0)$ after passing through an extinction medium at a distance $ds$:

$$I_\lambda(s) = I_\lambda(0)\exp(-\int_0^s k_{\lambda,ext}ds), \tag{2.2}$$

with $I_\lambda(0)$ being the incident intensity and $s$ the traversed distance.

For a plane-parallel (horizontally homogeneous) atmosphere, integration of the volume extinction coefficient results in the optical thickness $\tau_\lambda$:

$$\tau_\lambda = \int_0^z k_{\lambda,ext}(z)dz. \tag{2.3}$$

The volume extinction coefficient can be decomposed into a scattering and an absorbing part:

$$k_{\lambda,ext} = k_{\lambda,sca} + k_{\lambda,abs}. \tag{2.4}$$

The ratio of the scattering to the extinction coefficient is defined as the single scattering albedo:

$$\omega = \frac{k_{\lambda,sca}}{k_{\lambda,ext}}. \tag{2.5}$$

$\omega$ is virtually 1.0 at visible wavelengths for any droplet or ice crystal size, which implies that at these wavelengths the absorption by clouds does not play a significant role. However, in the near infrared $\omega$ becomes substantially lower than 1, with the lowest values for large ice crystals, as can be seen from Figure 2.2, which presents $\omega$ for various water droplets and ice crystal sizes at 1.63 $\mu$m, being near the center wavelength of the SEVIRI 1.6-$\mu$m channel.

The decrease in single scattering albedo with particle size in the near-infrared enables the retrieval of the cloud particle effective radius, which is defined as the ratio of the third to the second moment of a particle size distribution (Hansen and Travis 1974):

$$r_e = \frac{\int_0^\infty r^3 n(r) dr}{\int_0^\infty r^2 n(r) dr}, \tag{2.6}$$

where $r$ is the particle radius and $n(r)$ is the cloud particle radius distribution function.

As a result of the decrease in single scattering albedo, a lower reflectance for a cloud with a given optical thickness is observed in the near infrared compared to in the visible, with increasingly less reflectance for larger particles. In addition, the observed near-infreared reflectance of an ice cloud is lower than that of a water cloud, which is the key principle of the cloud-phase retrieval. It will be shown in Section 2.3 that from the observations of the SEVIRI 0.6 $\mu$m and 1.6 $\mu$m spectral channels the most important cloud physical properties relevant to the research in this thesis are obtained.

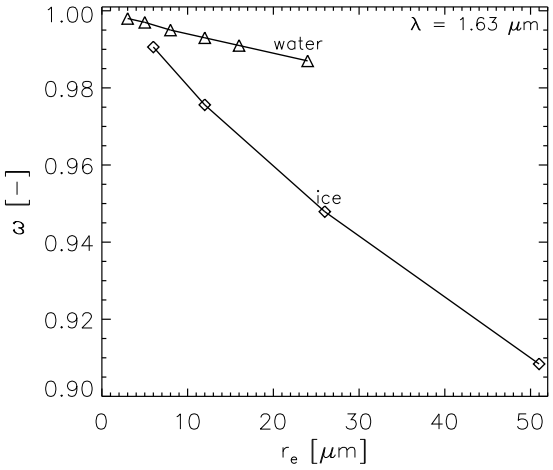


**Figure 2.2** *Single scattering albedo at 1.63 µm for water droplets with effective radii 3–24 µm (triangles) and roughened imperfect hexagonal ice crystals with effective radii of 6–51 µm (diamonds).*

The effect of the cloud particle size on the scattering properties is indicated by the size parameter, $x$, defined as the ratio of the cloud particle perimeter to the wavelength of the incident radiation ($x = 2\pi r/\lambda$). For $x \ll 1$, scattering is called Rayleigh scattering, which implies that sunlight is equally scattered into forward and backward directions. If the size parameter is of the order unity and particles are spherical, scattering is referred to as Lorenz–Mie scattering. In this scattering regime the largest part of the incident solar radiation is scattered into the forward direction. This scattering regime holds in principle for all particle sizes. For very large particles, especially ice crystals, which have $x \gg 1$ geometric optics can be applied.

The angular distribution of the scattered sunlight intensity is described by the phase function. Figure 2.3 shows examples of phase functions for a range of water droplet and ice crystal sizes at 0.64 $\mu$m and 1.63 $\mu$m. As can be seen, for water droplets the complexity of the phase function increases with increasing particle size. For example, the cloud bow feature around 138° becomes more pronounced with increasing cloud droplet size (Figure 2.3, upper left panel). Furthermore, for larger particles the backscatter features become more pronounced, while less energy is scattered to the sides (~80°–120°).

The lower panels show the phase functions for imperfect hexagonal columns (Hess et al. 1998), which are the ice crystal types that are used in the CPP retrieval algorithm. It was shown by Knap et al. (2005) that these imperfect hexagonal crystals are appropriate for calculating ice cloud reflectances for satellite cloud retrievals. The most striking difference compared to the water droplet phase functions is that the cloud bow and backscatter peaks are absent, because these are phenomena related to the spherical shape of water droplets. Ice crystals have halos at 22° and 48° scattering angles. However, these do not show up here, which is a consequence of an applied roughening factor to the hexagonal columns, which tends to distribute scattered light more evenly over the scattering angles outside the forward peak.

An important quantity for satellite remote sensing that is derived from the phase function is the asymmetry parameter $g$, defined as the average cosine of the scattering angles (the angle between direction of scattering and direction of incidence) found by integration over the entire scattering phase function. For particles that scatter sunlight into forward directions (0°–90°), $0 < g < 1$, while $-1 < g < 0$ when sunlight is scattered more into backward directions (90°–180°). For most water droplet sizes, the asymmetry parameter is about 0.85, whereas values for ice crystals are 0.75–0.80, depending on ice crystal type and particle roughening. The behavior of the assymetry parameter for various water and ice crystal effective radii is shown in Figure 2.4.

### *Emission and absorption of thermal radiation by clouds*

While scattering is the dominant extinction process taking place in the shortwave spectrum, emission and absorption dominate over scattering in the thermal infrared part of the spectrum. In the thermal infrared the single scattering albedo of both water droplets and ice crystals is low (<0.5). This implies that within 4-5 scatter events more than 90% of the incident solar radiation is absorbed.

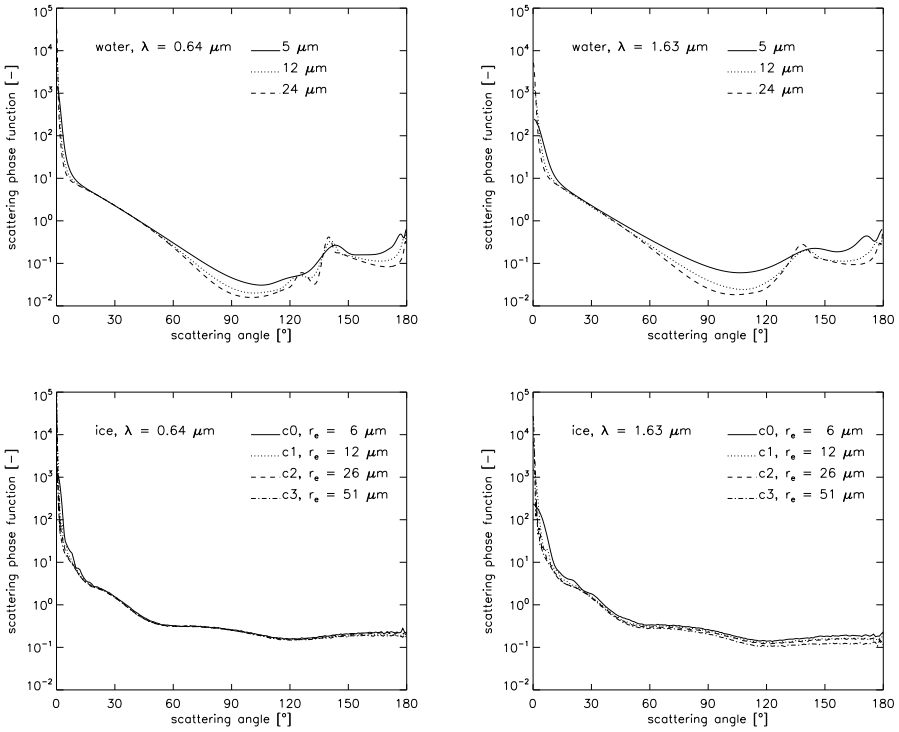


**Figure 2.3** *Scattering phase functions for (upper panels) spherical water droplets with effective radii 3–24 μm and (lower panels) roughened hexagonal ice crystals with effective radii of 6–51 μm. Phase functions are shown for 0.64 μm and 1.63 μm in the left and right panels, respectively.*

The Planck function describes the amount of emitted radiance assuming a perfect black body, i.e., a body that emits all of the absorbed radiance:

$$B_\lambda(T) = \frac{2hc^2}{\lambda^5(e^{hc/K\lambda T}) - 1}, \tag{2.7}$$

where $B_\lambda(T)$ is the emitted Planck radiance at a given temperature [W m$^{-2}$ sr$^{-1}$ $\mu$m$^{-1}$], $h$ is Planck's constant ($6.63\times10^{-34}$ J s), $K$ denotes the Boltzmann constant ($1.38\times10^{-23}$ J K$^{-1}$), and $c$ is the speed of light ($3.00\times10^{8}$ m s$^{-1}$). In general, a body emits less than a perfect black body, and the ratio of the thermal radiation emitted by a body at a temperature $T$ to the radiation emitted if the body obeyed Planck's radiation law is defined as emissivity.

The cloud-top temperature ($T_c$) is mostly retrieved from measured atmospheric window channel radiances (~10–12 $\mu$m, which is the spectral region in which atmospheric gas absorption is virtually absent). For optically thick clouds, the black body assumption is valid, as these clouds have an emissivity close to unity. However, for optically thin clouds the measured window channel radiance is an emissivity-weighted average of the surface and cloud contributions:

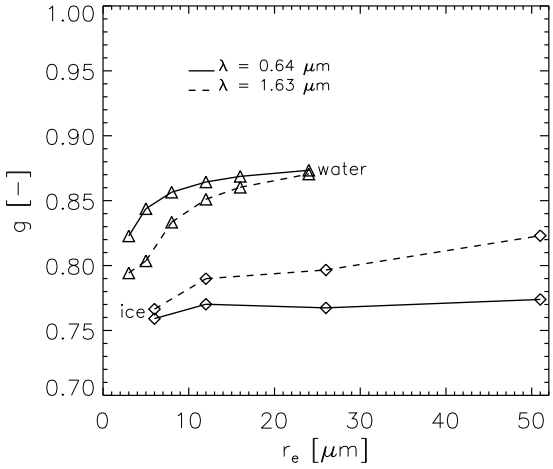


**Figure 2.4** *Asymmetry parameter for water droplets and roughened imperfect hexagonal ice crystals at 0.64 μm (solid lines) and 1.63 μm (dashed lines). Water droplets and imperfect hexagonal ice crystals are denoted by triangles and diamonds, respectively.*

$$I_\lambda = \varepsilon_{\lambda,c} B_\lambda(T_c) + (1-\varepsilon_{\lambda,c}) B_\lambda(T_s), \tag{2.8}$$

in which $I_\lambda$ is the measured upwelling radiance at top-of-atmosphere at the specific infrared wavelength, $\varepsilon_{\lambda,c}$ the cloud emissivity and $B_\lambda$ the Planck radiance at the given wavelength for cloud-top ($T_c$) and surface temperature ($T_s$). In the above equation, the cloud emissivity needs to be extracted in order to solve for the cloud-top temperature.
When neglecting thermal infrared scattering, the cloud emissivity at the window channel wavelength, $\varepsilon_{ir}$, is calculated from $\tau_{ir}$ (Minnis et al. 1998):

$$\varepsilon_{ir} = 1 - e^{-\tau_{ir}/\mu}, \tag{2.9}$$

with $\mu$ the cosine of the satellite viewing zenith angle and $\tau_{ir} \approx 0.5\tau_{vis}$ for most cloud particle sizes.

### *2.1.2 Radiative transfer models*

Solving the radiative transfer equation in a multiple scattering atmosphere is computationally expensive. During the last half century, numerous radiative transfer models (RTMs) have been developed to numerically or analytically solve this equation.

The discrete-ordinates method (Chandrasekhar 1960) is an efficient and powerful method for the calculation of the radiation fields in aerosol and cloudy atmospheres. It involves the discretization of the radiative transfer equation and uses a set of first-order differential equations to

numerically solve this equation for a discrete number of zenith angles. The discrete-ordinates method is used as a solver in several radiative transfer models, such as the Discrete Ordinates Radiative Transfer Model for a Multi-Layered Plane-Parallel Medium [DISORT, Stamnes et al. (1988)], the Spherical Harmonics Discrete Ordinates Model [SHDOM, Evans (1998)], and the Moderate-Resolution Atmospheric Transmission model [MODTRAN, Berk et al. (1987)].

In Monte Carlo methods (Macke et al. 1999), multiple scattering of sunlight is considered to be a stochastic process. Therefore the cloud particle phase function, as shown in Figure 2.3 is treated as a probability of scattering into a specific direction. Photons are emitted by a source, e.g. the sun, and are scattered and absorbed within a three-dimensional atmosphere containing clouds. The calculations continue until either the photon intensity becomes too low, photons leave the medium or become absorbed by clouds or the underlying surface. The Monte Carlo approach is useful for studying radiative transfer in complex media or to study 3D cloud effects. However, Monte Carlo methods are still computationally expensive and are hence less appropriate to be utilized in an operational environment.

The Doubling Adding KNMI (DAK) model has been developed to solve the multiple scattering problem in an efficient way. It is based on the doubling-adding method (van de Hulst 1980), that applies a physical approach to obtain a numerical solution of the multiple scattering problem. The atmosphere is assumed to consist of a number of homogeneous layers. To calculate the reflectance and transmission of each homogeneous layer, one starts with a very thin layer with small optical thickness in which no more than two scattering events are allowed to occur. Subsequently, layers with identical optical properties are doubled until the desired layer optical thickness is obtained. At each doubling step, the multiple reflections between two overlapping layers are calculated. The atmosphere is built up by adding layers on top of each other and by calculating the multiple reflections between the layers. More details can be found in De Haan et al. (1987) and Stammes (2001). DAK calculates the radiation field in a multi-layer atmosphere, in which the surface is assumed to be a Lambertian reflector. Further, clouds are considered to be plane-parallel and horizontally homogeneous. Rayleigh scattering, which is the scattering of sunlight by atmospheric molecules, as well as absorption by various gases ($CO_2$, $O_2$, $O_3$, $H_2O$) are taken into account.

### 2.1.3 Precipitation formation theory

The condensation of water vapor into water droplets or ice crystals and thus the formation of clouds and subsequently precipitation is taking place through various processes. The spontaneous transition from the gaseous into the solid or liquid phase (homogeneous nucleation), without aerosol particles acting as cloud condensation nuclei (CCN) would occur only at a supersaturation of 100% or more. Therefore heterogeneous nucleation of water vapor, in which CCNs are involved, into water droplets or ice crystals is the dominant process.

The concentration of CCNs is larger over continents than over oceanic areas. As a consequence, the concentration of water droplets and/or ice crystals in clouds will be larger over continental areas, which in most cases suppresses the precipitation formation and extends cloud lifetime (Albrecht 1989; Lohmann 2006). This suppression is found in both modeling studies on the effect of aerosol size and abundance on precipitation formation (Roelofs and Jongen 2004; Tao et al. 2007) and satellite observations (Rosenfeld and Lensky 1998).

The precipitation formation in clouds is generally divided into two types. The first type is coalescence, which is the growth of water droplets through collision. The second type is generally referred to as the Wegener-Bergeron-Findeisen process and occurs when water droplets and ice crystals coexist.

The coalescence process mostly takes place in 'warm' clouds with cloud-top temperatures above 0°C and is generally distinguished into three operating modes. The auto-convection process refers to collisions between droplets generally smaller than 20 $\mu$m. A second mode is when these smaller droplets collide with drizzle droplets (radius >20 $\mu$m), while the third mode is the collision between drizzle-sized droplets that form rain drops. The time between the start of coalescence and precipitation is in the order of one hour, although also time periods of 20–30 minutes have been observed (Stephens and Haynes 2007). Rosenfeld and Gutman (1994) translated the above process into a threshold of 14 $\mu$m for satellite-derived cloud particle effective radius to distinguish raining from non-raining clouds.

The Wegener-Bergeron-Findeisen process occurs when ice crystals and supercooled water droplets coexist. At equal temperatures and provided that the temperature is low enough for ice crystals to exist, the equilibrium water vapor pressure with respect to ice is lower than with respect to water, with the largest difference at 261 K (Pruppacher and Klett 1997). As a result, ice crystals will gain mass through water vapor deposition at the expense of liquid droplets losing mass through evaporation (Glickman 2000). When the ice particles have sufficient weight, they fall through the cloud as snow flakes and gain mass through collision with other ice crystals and/or supercooled water droplets.

In recent years, several techniques to trace the precipitation formation process in clouds from satellites have been developed. Most of these techniques rely on tracing $r_e$ information (Rosenfeld and Gutman 1994) or the combination of $r_e$ and infrared cloud-top temperature (Rosenfeld and Lensky 1998). The latter technique describes the development of $r_e$ versus $T_c$ and attributes this development to various formation modes, such as coalescence and the Wegener-Bergeron-Findeisen process.

## 2.2 Data

A number of satellite instruments were introduced in Chapter 1. Most of these instruments fly onboard polar orbiting satellites. The advantage of these satellite instruments is that due to their low altitude (700–800 km) they observe the Earth at a high spatial resolution.

However, polar orbiting satellite instruments observe the same location at the surface only 2-8 times per day, with the highest revisit frequencies over the polar regions. This implies that for the largest part of the Earth various cloud development processes, such as the initiation and maturing stage of convective clouds, cannot be properly observed. Geostationary satellite instruments, which are placed at such a distance that their orbital velocity equals that of the Earth (at ~35800 km distance), observe a given location continuously at 15-30 minute intervals and are thus suited to not only monitor possible long-term trends in cloud physical properties, but also to observe several cloud development processes at sub-daily time scales, such as the growth of convective clouds before they start to produce preciptation (Carbajal Henken et al. 2011).

### 2.2.1 Spinning Enhanced Visible and Infrared Imager (SEVIRI)

Since the launch of SEVIRI onboard the MSG Meteosat-8 and Meteosat-9 satellites in 2002 and 2005, respectively, the cloud research community has been provided with reflectances and radiances observed at a to date unprecedented high spatial and temporal resolution. Compared to the first generation of Meteosat satellites, the temporal resolution was improved from 30 to 15 minutes. In addition, the spatial resolution was improved from 5×5 $km^2$ to 3×3 $km^2$ at nadir, while the amount of spectral channels increased from 3 broadband to 12 narrowband channels. The availability of numerous narrowband channels enables detection of specific cloud and surface characteristics. A further improvement of the spatial resolution to 1×1 $km^2$ and 2×2 $km^2$ for the visible and infrared spectral channels, respectively, and a temporal resolution of 10 minutes is foreseen for the imager onboard the upcoming Meteosat Third Generation (MTG) satellites, of which the first is expected to be launched in 2017.

The research described in this thesis mainly uses observations from SEVIRI. The measured visible and near-infrared channel reflectances are used to retrieve several cloud physical properties important to the climate system and the hydrological cycle, such as cloud phase, cloud particle effective radius, and precipitation intensity. The SEVIRI 0.6-$\mu$m, 1.6-$\mu$m, 8.7-$\mu$m, and 10.8-$\mu$m spectral channels are the most frequently used in this thesis. Their spectral response functions are shown in Figure 2.5 together with the imaginary index of refraction (an indicator of the absorption efficiency of a material) of water droplets and ice crystals. It can clearly be seen that at 0.6 $\mu$m the amount of absorption for both water droplets and ice crystals is negligible, while at 1.6 $\mu$m absorption of solar radiation has become significant, with ice crystals absorbing radiation more efficiently than water droplets.

### 2.2.2 Moderate-Resolution Imaging Spectroradiometer (MODIS)

As already briefly touched upon in Chapter 1, the MODIS instrument flies onboard the Terra (local overpass time at 10:30) and Aqua (local overpass time at 13:30) satellites that were launched in 1999 and 2002, respectively. MODIS comprises 36 spectral narrowband channels in the range 0.4–14.4 $\mu$m.

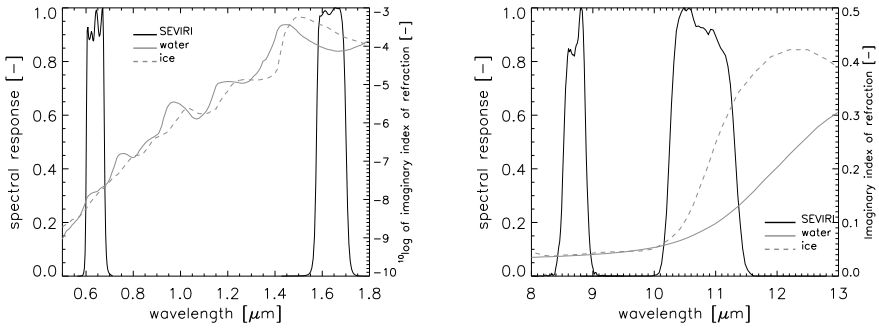


**Figure 2.5** *SEVIRI spectral response functions for (left) the 0.6-μm, 1.6-μm, and (right) 8.7-μm and 10.8-μm spectral channels. The imaginary index of refraction for water droplets (solid line) and ice crystals (dashed line) is plotted in grey, with scaling on the right-hand axis. Note the logarithmic scaling for the imaginary index of refraction in the left panel.*

Two visible channels (centered at 0.65 $\mu$m and 0.86 $\mu$m) observe at a nominal resolution of 250 $m^2$, five other visible and near-infrared channels observe at 500 $m^2$, while the remaining 29 channels have a spatial resolution of 1 $km^2$. A +/- 55° scanning pattern at an orbit of 705 km results in a 2,330-km swath and provides global coverage every one to two days. Both Terra and Aqua MODIS carry onboard calibration modules for the solar channels, which maintains the longterm stability of the measured reflectances within 1% (Xiong et al. 2011).

### 2.2.3 Tropical Rainfall Measurement Mission - Precipitation Radar (TRMM-PR)

The Tropical Rainfall Measurement Mission [TRMM, Kummerow et al. (1998)] satellite was launched in November 1997 and carries a Microwave Imager (TRMM-TMI) and a Precipitation Radar (TRMM-PR) to obtain more detailed information on the spatial and temporal distribution of precipitation in the tropics, which are largely undersampled by ground observations. For example, over the Netherlands the rain gauge density is such that for every ~120 $km^2$ precipitation is recorded, while in certain West African regions this density is sometimes as low as one rain gauge per >1000 $km^2$ (Ali et al. 2005). Furthermore, a considerable amount of precipitation is reported as pentadal (5-day) or decadal (10-day) sums, in which information at e.g. the diurnal cycle of precipitation is lacking. Therefore it was chosen to have the TRMM satellite fly in a non sun-synchronous orbit between 37°S and 37°N. In other words, a given location at the surface is sampled at different times of the day at each overpass. As a result, a full diurnal cycle of precipitation is observed once every 47 days. A disadvantage of this approach is that several years of data are required to obtain reliable statistics.

TRMM-PR is the first radar instrument to obtain precipitation information from space. Because the TRMM satellite flies at an altitude of about 402 km, the Precipitation Radar should have sufficient power to detect the weak return echo of hydrometeors.

Further, to obtain high-resolution three-dimensional information on precipitation, a higher radar frequency about three times higher as typical ground-based weather radars was chosen. The PR provides precipitation information at a horizontal and vertical resolution of 4.3 km$^2$ and 250 m, respectively. Due to the restrictions with respect to the returned echo from precipitation at off-nadir directions, its swath width is limited to 247 km, which results in a longer revisit time for a given surface location.

### 2.2.4 Advanced Microwave Scanning Radiometer - Earth Observing System (AMSR-E)

The AMSR-E instrument (Kawanishi et al. 2003) is a passive microwave instrument that flies onboard the Aqua satellite and measures brightness temperatures at six frequencies ranging from 7–89 GHz with a precision (RMSE) of 1 K. The horizontal resolution varies from about 5×5 km$^2$ at the highest frequency to about 56×56 km$^2$ at the lowest frequency. AMSR-E contains all the separate channels of its precursors, the Scanning Multichannel Microwave Radiometer (SSMR) and the Special Sensor Microwave/Imager (SSM/I) in one. The swath width is about 1450 km. The instrument was developed to measure key variables of the water cycle, such as cloud water content, water vapor, snow depth, and soil moisture. In this thesis, soil moisture retrievals from observed AMSR-E microwave brightness temperatures are used.

## 2.3 Retrieval algorithms

The retrieval of cloud physical and precipitation properties is performed in four steps. First, it is assessed whether a pixel contains clouds, which is performed using a separate algorithm. Second, if pixels are cloud-filled, the cloud physical properties are retrieved using the CPP algorithm. Third, once these cloud physical properties are retrieved, the distinction between raining and non-raining pixels is done and finally the rain rate for raining pixels is computed. The CPP algorithm was developed by Roebeling et al. (2006a) and retrieves cloud optical thickness ($\tau$), cloud particle effective radius ($r_e$), condensed water path (CWP), and cloud thermodynamic phase (CPH) from measured SEVIRI 0.6-$\mu$m and 1.6-$\mu$m reflectances. It uses a Lookup Table (LUT) approach based on the work of Nakajima and King (1990) and Nakajima and Nakajima (1995).

### 2.3.1 Reflectance Lookup Tables

The earlier described DAK model was used for the computation of the lookup tables (LUTs) for SEVIRI 0.6-$\mu$m and 1.6-$\mu$m water and ice cloud reflectances. First, the phase function for water droplets was calculated using Mie theory for spherical shapes assuming a Gamma size distribution with a fixed effective variance $v_e$ (a measure for the spread around the particle effective radius, $r_e$) of 0.15, while the phase function for ice crystals was calculated using ray tracing. Reflectances for the 0.6-$\mu$m and 1.6-$\mu$m spectral channels were stored in LUTs for cloud optical thicknesses of 0–256 and droplet effective radii of 1–24 $\mu$m.

Reflectances for ice clouds were computed using imperfect hexagonal columns (Hess et al. 1998) with volume equivalent effective radii of 6, 12, 26, and 51 $\mu$m. The volume equivalent effective radius is defined as the radius an ice crystal would have if the columnar volume were converted into a sphere.

To obtain accurate reflectance calculations, the amount of integration points in the azimuth direction (Fourier terms) and zenith angle direction (Gaussian $\mu$ points) used in the radiative transfer calculations needs to be sufficiently large. The largest number of Fourier terms and Gaussian $\mu$ points are required in the calculation for large cloud particles that are observed in the vicinity of the backscatter region (Wolters et al. 2006). The LUTs used in this thesis were generated with 140 Fourier terms and 180 Gaussian $\mu$ points.

The 0.6-$\mu$m and 1.6-$\mu$m reflectances were calculated by DAK for a black surface. The contribution of the surface albedo to the reflectance measured by a satellite instrument was computed following a procedure given by Chandrasekhar (1960). Over land, the surface albedo was obtained using a climatology derived from MODIS white-sky albedo data, which represents the bi-hemispherical surface reflectance that occurs below optically thick clouds. Over ocean surfaces, at both 0.6 $\mu$m and 1.6 $\mu$m an albedo of 0.05 was assumed.

Finally, the monochromatically calculated DAK reflectances were converted into the respective SEVIRI spectral channel reflectances using line-to-band conversion factors obtained from MODTRAN simulations (Meirink et al. 2009). Figure 2.6 shows an example of calculated water and ice cloud reflectances for fixed solar zenith, viewing zenith, and relative azimuth angles of 20°, 30°, and 100°, respectively. From this figure a number of features important to the cloud physical property retrievals can be gleaned. First, for $\tau$ >4 the lines of $\tau$ and $r_e$ dissect nearly orthogonally, which implies that these two cloud physical properties can be independently retrieved. Second, the retrieval of $\tau$ becomes extremely sensitive at large 0.6-$\mu$m reflectances, which follows from the decreasing distance between the optical thickness lines. Last, the $r_e$ retrieval for optically thin clouds becomes unreliable due to a large sensitivity to a change in 1.6-$\mu$m reflectance, the contribution of the underlying surface to the measured reflectances, and a decreased orthogonality with the optical thickness curves. The latter implies that the retrieval of $r_e$ is also sensitive to errors in the observed 0.6-$\mu$m reflectance.

### 2.3.2 Cloud detection algorithm

The distinction between cloud-filled and cloud-free pixels is based on an algorithm comprising several spectral threshold and spatial coherence tests, which was developed by the MODIS science team (Platnick et al. 2003). This algorithm has been adapted for use on SEVIRI data and is available through www-loa.univ-lille1.fr/~riedi. The SEVIRI cloud detection algorithm is different from the MODIS algorithm in that some of the threshold values have been modified taking into account the differences in spectral channel characteristics, calibration, and spatial resolution. In addition, the SEVIRI algorithm has been simplified from MODIS by reducing the number of tests.

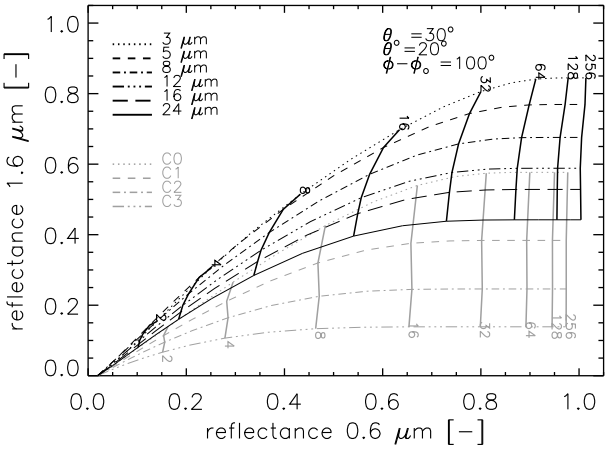


**Figure 2.6** *Transect through the water and ice reflectance LUT for $\theta$=20°, $\theta_\circ$=30°, and $\varphi$-$\varphi_\circ$=100°. The horizontally oriented lines denote a constant cloud particle effective radius, whereas the vertically oriented lines denote a constant cloud optical thickness. Lines are set in black and gray for the water and ice cloud particles, respectively.*

Finally, the decision logic in the SEVIRI algorithm is different from the one used in the MODIS algorithm. The SEVIRI cloud detection algorithm uses 0.6-, 0.8-, and 1.6-$\mu$m reflectances and 3.9-, 10.8-, and 12.0-$\mu$m brightness temperatures. In addition, the algorithm uses ancillary data on solar and viewing geometry and a land/sea map. The spectral threshold and spatial coherence cloud detection tests are different for land and ocean surfaces. The output of the cloud detection algorithm contains three categories: clear, cloud-contaminated, and cloud-filled.

### 2.3.3 Retrieval of cloud physical properties (CPP)

The CPP algorithm retrieves $\tau$ and $r_e$ from measured SEVIRI reflectances at 0.6 $\mu$m and 1.6 $\mu$m. The principle to retrieve these two cloud physical properties is that cloud reflectance at non-absorbing wavelengths in the visible spectral region (0.6 $\mu$m and 0.8 $\mu$m) is strongly related to the scattering optical thickness and only to a minor extent to $r_e$, while in the near infrared (1.6 $\mu$m, 2.2 $\mu$m, and 3.9 $\mu$m) the measured cloud reflectance is largely dependent on $r_e$.

Due to the increasing absorption efficiency of both water droplets and ice crystals with increasing wavelength, which determines the photon penetration depth, the $r_e$ retrieval is more weighted to the cloud top as wavelength increases (Platnick et al. 2001; Rosenfeld et al. 2004). However, the SEVIRI 3.9-$\mu$m channel is less favorable for retrieving $r_e$, because the observed radiance contains both reflected solar irradiance and thermally emitted radiance. Moreover,

the signal-to-noise-ratio is lower as a result of the significantly lower solar irradiance at 3.9 $\mu$m compared to at 1.6 $\mu$m. Especially for the $r_e$ retrieval of ice crystals this implies a very limited sensitivity. Lastly, due to the retrieved $r_e$ being more representative of the cloud top it will be less representative of the cloud bulk in case of optically thick clouds.

The retrieval of cloud physical properties is performed in an iterative manner. The measured 0.6- and 1.6-$\mu$m reflectances are alternately compared to the precalculated LUT values for given cloud optical thickness and particle effective radius, respectively. During the iteration, the $\tau$ ($r_e$) value is used to update the $r_e$ ($\tau$) retrieval from the 1.6-$\mu$m (0.6-$\mu$m) reflectance. This iteration procedure is continued until both $\tau$ and $r_e$ converge to within an absolute value of 0.05 relative to the previous iteration step. On average, about four iteration steps are required to meet the convergence criteria. Roebeling et al. (2005) showed that the retrieval of $\tau$ is susceptible to errors of up to 10% per percent measurement error in the 0.6-$\mu$m reflectance, especially for optically thick clouds, while the error in retrieved $r_e$ is much less sensitive to measurement errors in the 1.6-$\mu$m channel. The large sensitivity for $\tau$ is explained by the asymptotic behavior of the 0.6-$\mu$m reflectance for large $\tau$ (see the decreased distance between the $\tau$ lines in Figure 2.6). Because the $r_e$ retrieval is rather unreliable for optically thin clouds ($\tau$ <8), the retrieved $r_e$ is smoothed to climatological values of 8 $\mu$m and 26 $\mu$m for water and ice clouds, respectively, using a weighting function.

Cloud thermodynamic phase is retrieved through a consistency check of the difference between the measured 0.6- and 1.6-$\mu$m reflectances for water and ice clouds and a cloud-top temperature check from the observed 10.8-$\mu$m brightness temperature. In the consistency check the observed and precalculated difference between the 0.6- and 1.6-$\mu$m reflectances are compared. As a result of stronger absorption in the 1.6-$\mu$m spectral channel, the observed reflectance is expected to be lower at 1.6 $\mu$m than at 0.6 $\mu$m. In addition, at 1.6 $\mu$m ice crystals are more efficient absorbers of incident sunlight than water droplets, which implies that ice clouds have a lower 1.6-$\mu$m reflectance than water clouds.

In order to avoid erroneous cloud-phase retrievals for optically thin water clouds (e.g. at cloud edges or in case of broken cumuli clouds), an additional $T_c$ check is applied if a cloud-flagged pixel is labeled “ice" by the reflectance consistency test. If the retrieved cloud-top temperature exceeds 265 K, the initial “ice" retrieval is changed into “water". The $T_c$ is calculated from the measured 10.8-$\mu$m brightness temperature, which is corrected for cloud emissivities lower than unity. The cloud emissivity is in turn estimated using Equation 2.9.

From the retrieved $\tau$ and $r_e$ the Condensed Water Path (CWP, in units of g m$^{-2}$) is calculated (Stephens 1978):

$$\mathrm{CWP} = \frac{2}{3}\rho_w \tau r_e, \tag{2.10}$$

with $\rho_w$ the density of liquid water. At present, Equation 2.10 is used for calculating the CWP for both liquid water and ice clouds.

### 2.3.4 Precipitation Properties retrieval algorithm (CPP-PP)

The CPP-PP retrieval algorithm was developed by Roebeling and Holleman (2009). It has been adapted from a method originally developed for use on the Special Sensor Microwave/Imager (SSM/I) by Wentz and Spencer (1998) to make it suitable for use on SEVIRI data. The original algorithm is only applicable to water clouds, as microwave radiation is only to a minor extent scattered by ice crystals. Therefore Roebeling and Holleman (2009) have extended the applicability to ice clouds by including CWP. In other words, the CPP-PP algorithm is capable of retrieving precipitation intensity for both stratiform and convective precipitation.

The separation of precipitating from non-precipitating clouds is the first step in the retrieval of precipitation intensity. Precipitating clouds are detected from CWP, $r_e$, and cloud-phase information. Water cloud pixels with CWP larger than 150 g m$^{-2}$ and $r_e$ values larger than 16 $\mu$m are flagged "precipitating", while for ice clouds all pixels with CWP larger than 150 g m$^{-2}$ are flagged "precipitating".

For the pixels that are flagged "precipitating", the precipitation intensity ($P$, in mm h$^{-1}$) is calculated using the following equation (Roebeling and Holleman 2009):

$$P = \frac{c}{\Delta H}\left[\frac{\mathrm{CWP_a} - \mathrm{CWP_o}}{\mathrm{CWP_o}}\right]^{1.6}, \tag{2.11}$$

with $\mathrm{CWP_a}$ the actual condensed water path. $\mathrm{CWP_o}$ is an offset CWP value that is currently set at 125 g m$^{-2}$, the constant factor $c$ has a value of 1 and is of unit mm h$^{-1}$ km, and $\Delta H$ is the height of the rain column (in km), which is defined as:

$$\Delta H = \frac{T_{c,m} - T_{c,a}}{\gamma} + dH, \tag{2.12}$$

in which $T_{c,a}$ and $T_{c,m}$ denote the $T_c$ of the actual pixel and the maximum $T_c$ in a 100×100 pixel area around the actual pixel, respectively. The pixel with maximum $T_c$ is assumed to represent a low, thin cloud and thus gives an estimate of the cloud base. The denominator $\gamma$ represents the mean adiabatic lapse rate of 6.0 K km$^{-1}$ and $dH$ represents the minimum height of the raining column in km, which is currently set at 0.6 km.

# Chapter 3

## SEVIRI cloud-phase retrieval evaluation using ground-based observations

Three cloud-phase determination algorithms [Moderate-Resolution Imaging Spectroradiometer (MODIS)-like thermal infrared cloud-phase retrieval method, the Satellite Application Facility on Climate Monitoring (CM-SAF) method, and an International Satellite Cloud Climatology Project (ISCCP)-like method] are explored to assess their suitability for climate monitoring purposes in mid-latitude coastal climate zones. Using one year (May 2004–April 2005) of data from SEVIRI onboard Meteosat-8, retrievals of the methods are compared to collocated and synchronized ground-based cloud-phase retrievals obtained from cloud radar and lidar observations at Cabauw, the Netherlands. Three aspects of the satellite retrievals are evaluated: 1) Instantaneous cloud-phase retrievals, 2) monthly averaged water and ice cloud occurrence frequency, and 3) daytime diurnal cycle of cloud phase for May–August 2004. For the instantaneous cases, all methods show very small bias for thick water and ice cloud retrievals (~5%). The ISCCP-like method has a larger bias for pure water clouds (~10%), which is likely due to the 260 K threshold leading to misdetection of water clouds existing at lower temperatures. For the monthly averaged water and ice cloud occurrence frequency, the CM-SAF method is best capable of reproducing the annual cycle, mainly for the water cloud occurrence frequency, for which an almost constant positive bias of ~8% was found. The ISCCP- and MODIS-like methods have more problems to detect the annual cycle, especially during the winter months. The difference in annual cycle detection between the three methods is most probably related to the use of visible/near-infrared reflectances which enable a more direct observation of cloud phase. The daytime diurnal cycle of cloud phase is well reproduced by all methods. The MODIS-like method reproduces the daytime diurnal cycle best, with correlations of 0.89 and 0.86 for water and ice cloud occurrence frequency, respectively.

Based on: Wolters, E.L.A., R.A. Roebeling, and A.J. Feijt, 2008: Evaluation of cloud-phase retrieval methods for SEVIRI on Meteosat-8 using ground-based lidar and cloud radar data, *J. Appl. Meteorol. Clim.*, **47**, 1723–1738, doi:10.1175/2007JAMC1591.1.

## 3.1 Introduction

The interaction between clouds and radiation is of great importance to the Earth's surface energy balance. Clouds reflect and absorb solar radiation and emit and absorb terrestrial radiation. The cloud–radiation interaction is of a complex nature and is dependent upon properties such as cloud particle size, cloud temperature, cloud phase, water vapor and aerosol abundance, and surface reflectivity. Accurate detection of cloud phase is important because water and ice clouds influence the surface energy balance differently. Water clouds reflect shortwave irradiance, while ice clouds absorb and emit outgoing terrestrial radiation back to the Earth's surface. Cloud-phase determination can be regarded as the subsequent step to cloud masking in retrieving cloud properties from satellite measurements.

During the past decades, several approaches to infer cloud phase from satellite imagery have been developed. Based on the type of spectral information used, these methods can be divided into three groups. The first group uses thermal infrared radiances, the second group utilizes visible and near-infrared reflectances, whereas the third group uses a combination of visible, near-infrared, and thermal infrared radiances.

The advantage of using only thermal infrared radiances is the capability of obtaining cloud-phase information during both daytime and nighttime, which enables detection of the full diurnal cycle of cloud phase. In contrast, visible and near-infrared methods can only be applied during daytime. Because outgoing surface radiance significantly contributes to the radiance measured by a satellite instrument, thermally based cloud-phase retrievals are sensitive to errors in case of optically thin and broken clouds. In addition, brightness temperature thresholding affects the cloud-phase retrieval by assuming a sudden transition from water to ice clouds below a certain temperature threshold, whereas in reality this transition depends on e.g. cloud dynamics and the cloud condensation nuclei concentration. Arking and Childs (1985) obtained information on cloud thermodynamic phase based primarily on 3.7- and 10.8-$\mu$m channel radiances measured by the Advanced Very High Resolution Radiometer (AVHRR) onboard the National Oceanographic and Atmospheric Administration (NOAA) satellites. Strabala et al. (1994) developed a trispectral method to determine cloud phase using 8.5-, 11- and 12-$\mu$m radiances observed by the Moderate-Resolution Imaging Spectroradiometer (MODIS), which was adopted for operational use within the MODIS scientific cloud datasets (Platnick et al. 2003). Rossow and Schiffer (1999) defined a threshold for the cloud-top temperature derived from 10.8-$\mu$m brightness temperature to discriminate water from ice clouds within the International Satellite Cloud Climatology Project (ISCCP).

The methods of the second group are based on visible and near-infrared reflectances, which directly depend on the optical properties of liquid and solid cloud particles. At visible wavelengths, reflectance is primarily a function of cloud optical thickness, whereas at longer wavelengths (such as the cloud particle absorption bands around 1.6 $\mu$m) reflectance is dominated by particle size (Nakajima and King 1990). Hansen and Pollack (1970) used the differences between visible and near-infrared reflectances to derive cloud particle phase and size. Pilewskie and Twomey (1987) performed ground-based reflectance measurements between 0.63 and 1.9 $\mu$m to derive the cloud phase of convective clouds. Knap et al. (2002) developed a

method using 1.64- and 1.70-$\mu$m reflectances from the Airborne Visible and Infrared Imaging Spectrometer (AVIRIS) to obtain accurate cloud-phase retrievals over ocean surfaces.

The methods of the third group utilize combinations of visible, near-infrared, and thermal infrared radiances. The strength of combining visible with thermal infrared information is that the quality of the retrievals can be improved through the combination of different tests, while a disadvantage is still the limitation to daytime cloud scenes due to the usage of visible and near-infrared data. Baum et al. (2000) improved the trispectral thermal infrared method of Strabala et al. (1994) by adding 0.63-, 1.63- and 1.90-$\mu$m reflectances to increase the cloud-phase retrieval accuracy for thin cirrus clouds. The cloud-phase determination method used within the Satellite Application Facility on Climate Monitoring (CM-SAF) of the European Organization for the Exploitation of Meteorological Satellites (EUMETSAT) combines 0.6- and 1.6-$\mu$m reflectance with an additional cloud-top temperature check for the retrieval of ice clouds.

Although good progress in the theoretical understanding of retrieving cloud-phase information from passive imagers has been made, most validation efforts have been performed on a small number of cases. Little is known about the accuracy of the various cloud-phase determination methods when applied to long-term datasets, which form the basis for climate monitoring applications, such as obtained by ISCCP, CM-SAF, and the MODIS Atmosphere group. Although several ground-based measurement campaigns focusing on the radiative importance of supercooled water or mixed-phase clouds from ground-based measurements have been performed (Hogan et al. 2003; Turner 2005; Turner et al. 2003), little research has been done to explore the quality of satellite water and ice phase retrievals. In this Chapter, we investigate the suitability of three widely used satellite cloud-phase retrieval methods for climate monitoring purposes in a mid-latitude coastal climate, using data from the Spinning Enhanced Visible and Infrared Imager (SEVIRI) onboard the first Meteosat Second Generation satellite (Meteosat-8). The methods investigated are: (i) a MODIS-like method using the brightness temperature difference 8.7-10.8 $\mu$m combined with the 10.8-$\mu$m brightness temperature, (ii) an ISCCP-like method using a 260 K cloud-top temperature threshold, and (iii) a combined 0.6/1.6 $\mu$m reflectance method with an additional cloud-top temperature check, which is used within the CM-SAF.

The accuracy of the satellite water and ice phase retrievals is assessed by comparing retrievals to ground-based cloud phase obtained from cloud radar and lidar using an algorithm described by Illingworth et al. (2007). First, the accuracy of the three methods is assessed for homogeneous water or ice cloud cases. Subsequently, it is investigated whether the methods are able to reproduce both the annual cycle and the daytime diurnal cycle in liquid water and ice cloud occurrence frequency as observed from the surface.

The paper is organized as follows. Section 3.2 describes the satellite cloud-phase determination methods evaluated, as well as the method for retrieving cloud phase from ground-based lidar and cloud radar measurements. In section 3.3, satellite and surface data processing is presented. Validation results for the different satellite cloud-phase determination methods are shown in section 3.4 and conclusions are drawn in section 3.5.

## 3.2 Cloud-phase determination algorithms

### 3.2.1 Satellite algorithms

#### MODIS thermal infrared cloud-phase determination algorithm

The MODIS bispectral infrared cloud-phase retrieval algorithm is part of the MODIS Atmosphere Science Dataset (SDS Collection 5, see http://modis.gsfc.nasa.gov). It uses the combination of 8.5-11.0 $\mu$m brightness temperature difference (hereafter referenced as $BTD_{8.5\text{-}11}$) and 11.0-$\mu$m brightness temperature to determine cloud phase (Platnick et al. 2003). The method relies on the fact that for water and ice the absorption efficiency coefficients are nearly equal in the water vapor absorption region around 8 $\mu$m, while around 11 $\mu$m ice is a more efficient absorber than water and thus has a lower brightness temperature (see Figure 3.1).

Strabala et al. (1994) showed that $BTD_{8.5\text{-}11}$ values around zero can be expected for clear sky scenes, whereas $BTD_{8.5\text{-}11}$ is positive and negative for ice and water clouds, respectively. Because SEVIRI has a spectral channel centered at 8.7 $\mu$m instead of 8.5 $\mu$m, the spectral difference between the two channels affects the brightness temperature difference. Due to less water vapor absorption in the SEVIRI 8.7 $\mu$m spectral band, the SEVIRI 8.7-$\mu$m brightness temperature is higher than the MODIS 8.5-$\mu$m brightness temperature. To account for this effect, all $BTD_{8.5\text{-}11}$ thresholds used by the MODIS group were adjusted for use on SEVIRI data (see Table 3.1). Furthermore, errors in the SEVIRI thermal infrared radiance to brightness temperature conversion (EUMETSAT 2007) necessitated an additional correction to both the 8.7- and 10.8-$\mu$m brightness temperatures.

The MODIS cloud-phase determination method classifies cloud-flagged pixels into four categories: water, ice, mixed phase, and undefined. As this paper focuses on the quality of water and ice detection, undefined classifications were discarded from the dataset, while mixed phase classifications (~8% of all cloud phase retrievals) were added to the ice category, because visual image inspection of one month of MODIS images over Europe revealed that mixed phase is mainly retrieved from the (optically thin) edges of ice clouds.

**Table 3.1** *Thresholds for the MODIS thermal infrared cloud-phase determination method using MODIS (left column) and SEVIRI data (right column). $\Delta T$ refers to the brightness temperature difference 8.5-11.0 $\mu$m and 8.7-10.8 $\mu$m for MODIS and SEVIRI, respectively.*

| | MODIS | SEVIRI |
|---|---|---|
| water | ($T$ > 238 K and $\Delta T$ < -1.0) or ($T \geq$ 285 K and $\Delta T \leq$ -0.5 K) | ($T$ > 238 K and $\Delta T$ < -0.5) or ($T \geq$ 285 K and $\Delta T \leq$ 0.0 K) |
| ice | ($T \leq$238 K) and ($\Delta T$ > 1.0 K) | ($T \leq$ 238 K) and ($\Delta T$ > 1.5 K) |
| mixed | (238 K < $T$ < 268 K) and (-0.25 K $\leq \Delta T$ <0.5 K) | (238 K < $T$ < 268 K) and (0.25 K $\leq \Delta T$ <1.0 K) |
| undefined | (238 K < $T$ < 268 K) and (-1.0 K < $\Delta T$ < -0.25 K) | (238 K < $T$ < 268 K) and (-0.5 K < $\Delta T$ < 0.25 K) |

#### ISCPP-like cloud-phase determination algorithm

A widely used way to infer cloud-phase information is by thresholding thermal infrared brightness temperatures. That is, a cloud-flagged pixel having a brightness temperature lower than

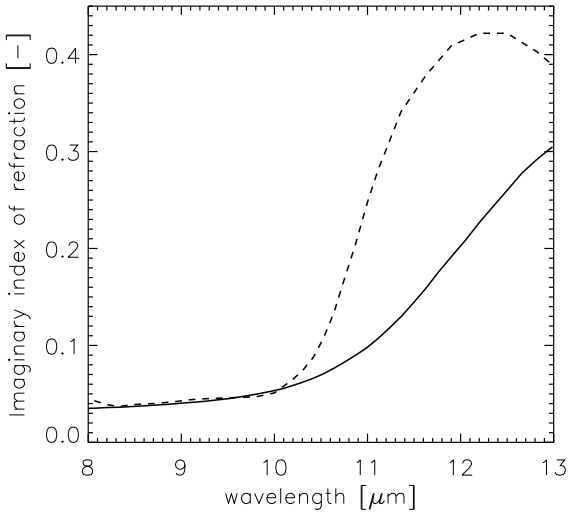


**Figure 3.1** *Imaginary index of refraction for water (solid) and ice (dashed) between 8 and 13 μm. Water indices are from Downing and Williams (1975), ice indices are from Warren (1984).*

a certain threshold value is attributed to the ice phase. The water vapor saturation pressure difference in clouds between water and ice reaches its maximum near 261 K (Pruppacher and Klett 1997), which implies that below these temperatures ice particles are more easily formed than water particles. For opaque clouds, the measured 10.8-$\mu$m brightness temperature can be regarded as the thermodynamic temperature from the uppermost part of the cloud, because the cloud emissivity, $\varepsilon$, approaches unity. Furthermore, absorption by water vapor in the atmospheric column above the cloud is negligible in the 10.8 $\mu$m spectral channel.

For semi-transparent or broken cloud cases, the thermal infrared radiation emitted by the cloud is approximated as follows:

$$B_m = \varepsilon_{\lambda,cl} B_{cl} + (1 - \varepsilon_{\lambda,sur}) B_{sur}, \tag{3.1}$$

with $B_m$, $B_{cl}$, and $B_{sur}$ the measured, cloud, and surface Planck radiation measured at 10.8 $\mu$m, with the latter to be estimated from the near-surface temperature. $\varepsilon_{\lambda,cl}$ and $\varepsilon_{\lambda,sur}$ are the cloud emissivity at wavelength $\lambda$ for the cloud and surface, respectively. From Equation (3.1) it follows that for semi-transparent and broken clouds the brightness temperature obtained from the measured 10.8-$\mu$m radiance is not representative for the real cloud temperature, due to the contribution of the surface radiance.

In order to account for $\varepsilon_{\lambda,cl} < 1$, the 10.8-$\mu$m radiance is corrected. The correction uses the cloud absorption optical thickness at 10.8 $\mu$m, $\tau_{10.8}$, which is related to the cloud scattering optical thickness at 0.6 $\mu$m, $\tau_{0.6}$, obtained directly from visible reflectance measurements:

$$\tau_{10.8} = \tau_{0.6} \frac{Q_{10.8}}{Q_{0.6}}, \tag{3.2}$$

with $Q_{10.8}$ and $Q_{0.6}$ the extinction efficiency coefficients at 10.8 $\mu$m and 0.6 $\mu$m, respectively. Generally, $\tau_{10.8} \approx 0.5\tau_{0.6}$. When neglecting thermal infrared scattering, the cloud emissivity at 10.8 $\mu$m, $\varepsilon_{10.8}$, can be calculated using $\tau_{10.8}$ (Minnis et al. 1998):

$$\varepsilon_{10.8} = 1 - \exp(\frac{-\tau_{10.8}}{\mu}), \tag{3.3}$$

with $\mu$ the cosine of the satellite viewing zenith angle. A consequence of using $\tau_{0.6}$ is that this correction can only be applied during daytime.

A similar approach is utilized by the ISCCP method to obtain cloud phase for low and midlevel clouds, using 260 K as threshold temperature (Rossow and Schiffer 1999). Riédi et al. (2001) found a sharp transition from pure water to pure ice clouds at 240 K when they compared Polarization and Directionality of the Earth's reflectances (POLDER) cloud-phase retrievals to lidar and radar cloud-top retrievals at the Atmospheric Radiation Measurement (ARM) site at Oklahoma (USA). It was suggested to change the temperature threshold used in ISCCP accordingly. These results were contradicted by Hogan et al. (2003), who found a more gradual decrease in (supercooled) water occurrence at temperatures from 268 K down to 238 K using ground-based lidar measurements at Chilbolton (United Kingdom).

### *CM-SAF cloud-phase determination method*

The CM-SAF cloud-phase determination method was developed at the Royal Netherlands Meteorological Insitute (KNMI) as part of the Cloud Physical Properties algorithm (Jolivet and Feijt 2005; Roebeling et al. 2006a) within the framework of the CM-SAF. The method uses differences in the water and ice absorption characteristics to discern water from ice clouds. At near-infrared wavelengths, ice particles absorb sunlight more efficiently than water particles and will thus have a lower reflectance. The retrieval of cloud phase is done iteratively by comparing observed satellite reflectances at 0.6 $\mu$m and 1.6 $\mu$m to lookup tables (LUTs) of Radiative Transfer Model (RTM) simulated reflectances. Water and ice are assigned to those cloudy pixels for which the measured 0.6- and 1.6-$\mu$m SEVIRI reflectances correspond to the respective simulated LUT reflectance. Cloud-flagged pixels initially assigned to 'ice' are labeled as 'water' if the emissivity-corrected cloud-top temperature exceeds 265 K.

The LUT reflectances are modeled using the Doubling Adding KNMI (DAK) RTM (De Haan et al. 1987; Stammes 2001), which calculates shortwave reflectance at top-of-atmosphere assuming plane-parallel homogeneous clouds above a Lambertian surface. The phase function of water droplets is calculated using Mie theory for spherical particles assuming a Gamma size distribution (Hansen and Travis 1974) with an effective variance, $\nu_{\text{eff}}$, of 0.15 and effective radii ranging from 1–24 $\mu$m. Ray tracing is used to calculate the ice particle phase function for imperfect hexagonal crystals of type C0 ($r_{\text{eff}}$=6 $\mu$m), C1 ($r_{\text{eff}}$=12 $\mu$m), C2 ($r_{\text{eff}}$=26 $\mu$m), and C3 ($r_{\text{eff}}$=51 $\mu$m) of the Cirrus Optical Properties (COP) ice crystal library (Hess et al. 1998). Surface albedo information is obtained from the MODIS white sky surface albedo product (Platnick

et al. 2003).

A cross section of the DAK ice and water LUTs is shown in Figure 3.2. Solar zenith angle, $\theta_\circ$, viewing zenith angle, $\theta$, and azimuth difference angle, $\varphi$-$\varphi_\circ$, were chosen at 30°, 20°, and 100°, respectively. The upper part of Figure 3.2 represents cloud reflectances modeled for water particles with effective radii of 3–24 $\mu$m, whereas cloud reflectances for ice crystals of type C0, C1, C2, and C3 are displayed in the lower part. Cloud optical thickness for the SEVIRI 0.6-$\mu$m spectral channel, hereinafter referenced as cloud optical thickness, $\tau_{0.6}$, and $r_{\text{eff}}$ can be retrieved independently for $\tau_{0.6} > 4$, because their LUT contours intersect (nearly) orthogonally. Further, the plots show that the 0.6- and 1.6-$\mu$m reflectances of small ice crystals and large water droplets overlap for $\tau_{0.6} >\sim 4$. For these cases, the emissivity-corrected cloud-top temperature with threshold value 265 K is used as a cloud-phase indicator.

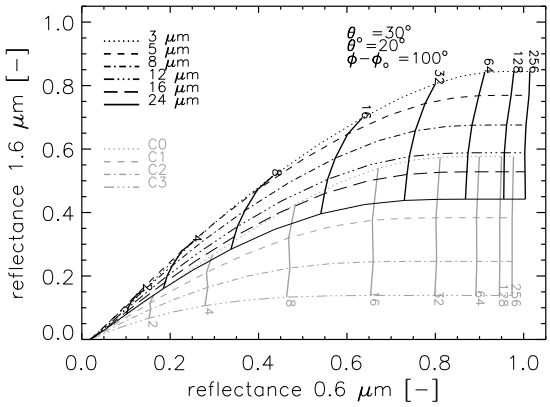


**Figure 3.2** *Modeled 0.6- and 1.6-$\mu$m reflectances for $\theta_\circ$=30°, $\theta$=20°, and $\phi$-$\phi_\circ$=100°. Cloud optical thickness is denoted by the vertically oriented lines, effective radius by horizontally oriented lines. Water particles are represented in the upper part of the graph, ice particles in the lower part.*

### 3.2.2 Cloud-phase determination from ground-based measurements

A method to determine cloud phase from lidar and cloud radar measurements described by Illingworth et al. (2007) is applied to measurements of the CloudNET site of Cabauw (The Netherlands, 51.97°N, 4.93°E). The algorithm simultaneously uses cloud radar vertical Doppler velocity, lidar attenuated backscatter profiles, and Numerical Weather Prediction (NWP) model temperature profiles.

Cloud radar measures both the reflectivity of (cloud) particles and the convolution of particle velocity and vertical air motion. The wavelength of cloud radar instruments is such that in

most cases the size of cloud particles is much smaller than the wavelength of the incident beam, which means that the Rayleigh scattering regime applies. Within this regime, radar reflectivity ($Z$) is proportional to the second moment of particle mass. The cloud radar at Cabauw is operated at a frequency of 35 GHz ($\lambda$=8.6 mm) with a beamwidth of 0.36° and a vertical resolution of about 90 m. Due to its proportionality to particle mass, the cloud radar reflectivity signal is dominated by large cloud particles. Optically thin layers consisting of large ice crystals may show up as geometrically very thick layers in the cloud radar reflectivity signal.

Furthermore, in case of heavy rain the signal becomes saturated due to the large reflectivity from rain droplets, which implies that no cloud property information can be derived from higher cloud levels.

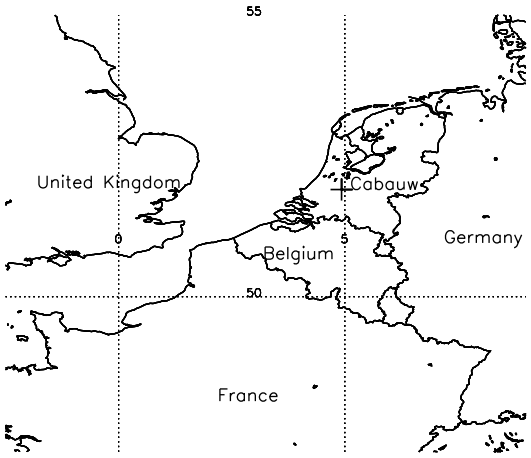


**Figure 3.3** *Location of the Cabauw measurement site.*

Lidar instruments are mostly used to identify the cloud base of liquid water clouds. For cloud optical thickness values lower than about 4 also the cloud top height can be detected with an accuracy of tens to hundreds of meters (Chepfer et al. 2000). The backscatter coefficient, $\beta$, is the amount of emitted photons scattered back to the lidar instrument by atmospheric particles, such as cloud droplets or aerosols. The attenuated backscatter coefficient, $\beta'$, which is usually reported, is the backscatter coefficient corrected for gaseous absorption. The majority of the lidar instruments operate from ultraviolet up to near-infrared wavelengths. At Cabauw, a 0.905 $\mu$m lidar with a vertical resolution of ~30 m is operated.

Determination of cloud phase is performed in three steps. First, the algorithm estimates the cloud melting layer height, taking the level where the NWP model wet-bulb temperature ($T_{\mathrm{W}}$) equals 0° C. Subsequently, this estimate is refined using the cloud radar vertical Doppler velocity profile, as in general a large and sharp increase in the fall speed of cloud particles can be detected below the melting layer. It is noted here that the Doppler vertical velocity is only

searched when the model wet-bulb temperature is between -5° C and +5° C. If the melting layer is outside this temperature region the altitude of the melting layer height is assumed at level $T_W$=0° (R. Hogan, personal communication, 2007). The probability of the model wet-bulb temperatures being outside this region is very small. Mittermaier and Illingworth (2003) showed that for the Met Office Unified mesoscale model (UM) the obtained 0° C wet-bulb temperature level has a bias of +15 m compared to radar-obtained values for the $t$+0h to $t$+5h forecast, with an rms error of 147 m. Finally, if available, the attenuated lidar backscatter coefficient is evaluated to determine the presence of thin supercooled water layers within ice clouds. The method described above enables cloud-phase determination for the vertical profile up to ~12 km with a vertical resolution of ~90 m.

The following output categories from the ground-based algorithm are considered: "cloud liquid droplets", "drizzle/rain & cloud droplets", "ice", "ice & supercooled droplets", "melting ice", and "melting ice & cloud droplets". For the comparison of satellite cloud-phase retrievals with ground-observed cloud phase, the above categories were binned into three new categories for each sampling period: the "cloud droplets" and "drizzle/rain & cloud droplets" categories were labeled as water, the "ice" and "melting ice" categories were labeled as ice, and "ice & supercooled droplets" and the "melting ice & cloud droplets" categories were labeled as mixed phase.

Note that simultaneously using active cloud radar and lidar provides information on the vertical geometrical extent of a cloud and its properties, while passive satellite radiometers are mainly sensitive to the optical thickness of a cloud. In particular, the sensitivity of cloud radar reflectivity to large cloud particles requires attention. If an ice cloud contains large particles, radar reflectivity is high due to the proportionality with particle mass. However, if the ice water content of the cloud is low, the extinction and hence the cloud optical thickness is low.

Due to this low extinction, SEVIRI may not be capable of detecting ice clouds with relatively low ice water contents, which increases the likelihood of cloud-phase misclassification when such a cloud overlays a water cloud. Moreover, it should be noted that the quality of the ground-based cloud-phase observations is best when both cloud radar and lidar data are available. That is, when the lidar is unavailable or attenuated due to thick low level water clouds, higher levels cannot be searched for supercooled water. Therefore these ground-based retrievals should be carefully interpreted when used for evaluation of satellite-derived cloud phase.

## 3.3 Data and methods

### 3.3.1 Satellite data analysis

All satellite algorithms were tested using one year (May 2004–April 2005) of data from SEVIRI. The SEVIRI instrument contains 12 spectral channels: one visible, three near-infrared, seven thermal infrared, and one high-resolution visible channel. For this study, the 0.6-, 1.6-, 8.7-, and 10.8- $\mu$m spectral channels were used. SEVIRI daytime data was archived at a 15-minute

resolution. The SEVIRI 0.6- and 1.6-$\mu$m reflectances were cross-calibrated with the corresponding reflectances from MODIS-Terra, which carries in-flight absolute calibration instruments with an expected uncertainty of about 2% for the visible channels (Doelling et al. 2004; Roebeling et al. 2006a).

The algorithm to separate cloud-free from cloud-contaminated and cloud-filled pixels is based on the MODIS cloud detection algorithm (Platnick et al. 2003). This algorithm has been simplified and modified to make it applicable for SEVIRI (http://www-loa.univ-lille1.fr/~riedi/). The input to the SEVIRI cloud detection algorithm consists of normalized reflectances from the visible (0.6 $\mu$m and 0.8 $\mu$m) and near-infrared (1.6 $\mu$m) channels, whereas brightness temperatures are used from the thermal infrared channels (3.8, 8.7, 10.8 and 12.0 $\mu$m). In addition, the algorithm uses ancillary data on solar and viewing geometry and a land/sea map. There are spectral threshold and spatial coherence cloud detection tests that are different for land and ocean surfaces. The SEVIRI thresholds differ slightly from the MODIS thresholds because of differences in instrument calibration, channel characteristics and spatial resolution between the instruments.

Cloud phase was determined for individual pixels using the methods introduced in Section 3.2.1. For the ISCCP-like method, a temperature threshold of 260 K was used. $R_{sur}$ (see Equation 3.1) was calculated by applying the Planck function, weighted for the SEVIRI 10.8-$\mu$m spectral band, to European Center for Medium-Range Weather Forecasts (ECMWF) 10-meter temperatures. The 10-meter temperature was chosen because in cloudy situations the difference between 10-meter and surface skin temperature is small. Values for $Q_{10.8}$ and $Q_{0.6}$, used to convert $\tau_{0.6}$ into $\tau_{10.8}$, were obtained using a polynomial fit through values from Mie calculations for effective radii between 1 and 24 $\mu$m.

Subsequently, the cloud-top temperature was obtained using Equations 3.1 and 3.3. For the CM-SAF method, retrievals were limited to $\theta_\circ \leq 72^\circ$. Although not consistent with the recommendation of Loeb and Coakley (1998) to only use 1D simulated cloud reflectance for $\theta_\circ < \sim 60^\circ$, it was chosen to exceed this limit to also include winter observations in the dataset. Furthermore, cases in which the MODIS-like method retrieval was undefined were discarded for all methods.

### 3.3.2 Ground-based data analysis

Ground-based cloud-phase observations were recorded at a 15-second time resolution at Cabauw, The Netherlands. To account for the difference in observation techniques between satellite and ground-based instruments, the ground-based observations were collected over a 30-minute time window centered at the SEVIRI scanning time for Cabauw, being about 12 minutes past the SEVIRI slot time. Furthermore, to minimize broken cloud field effects or mismatch in cloud detection between satellite and ground-based instruments, only cases with cloud cover >90% within the 30-minute time window were included.

From the ground-based observations, cloud phase at both a high temporal resolution and for an entire cloud profile rather than only for the cloud top was derived. In addition, water clouds with a geometrical thickness of a few hundred meters are mostly optically thick, whereas ice clouds often have low optical thickness even when their geometrical thickness is large. Therefore criteria were developed to interpret each 30-minute time window into a single cloud phase value.

It was shown in section 3.2.2 that for each sampling period the six cloud phase categories as obtained from the algorithm of Illingworth et al. (2007) were binned into a water, ice, and mixed-phase category. For each of these three categories the thickness per sampling period (15 s) was calculated. Subsequently, the average thickness of the three categories within the 30-minute time window period was calculated. Finally, threshold values were set for the average ice, water, and mixed-phase cloud thickness to attribute the time window period to a unique cloud phase. Table 3.2 presents the criteria that are used to interpret 30-minute averaged water, ice, and mixed phase cloud thickness ($\Delta h_w$, $\Delta h_i$, and $\Delta h_m$, respectively) in terms of a single cloud phase for the considered period. Cloud systems with $\Delta h_i$ <600 m and ($\Delta h_w/\Delta h_m$)>4 were labeled as water cloud. Clouds with $\Delta h_i$ > 2500 m were labeled as ice, whereas for $\Delta h_i$ <2500 m and ($\Delta h_w/\Delta h_m$)<4 mixed phase was assigned.

**Table 3.2** *Criteria applied to 30-minute averages of ground-based observed water, ice, and mixed cloud layer thickness for calculation of monthly averaged cloud phase occurrence. $\Delta h_i$ refers to ice layer thickness, $\Delta h_w$ to water layer thickness, and $\Delta h_m$ to mixed layer thickness.*

| cloud phase | criterion |
|---|---|
| ice | $\Delta h_i > 2500$ m |
| water | $\Delta h_i < 600$ m & ($\Delta h_w$ / $\Delta h_m$) > 4 |
| mixed phase | 0 m < $\Delta h_i < 2500$ m & ($\Delta h_w$ / $\Delta h_m$) < 4 |

### 3.3.3 Comparison of satellite to ground-based cloud-phase observations

The comparison of the satellite retrievals to ground-observed cloud phase was divided into three parts: (i) instantaneous water and ice cloud retrievals, (ii) monthly averages of water and ice cloud occurrence frequency using a three-month moving window, and (iii) daytime diurnal cycle of cloud phase. The latter was performed for May-August 2004 only, because the daytime diurnal cycle of water and ice occurrence frequency can be distinguished best when convection prevails, which is mostly the case during the Western European summer months.

#### *Instantaneous water and ice cloud retrievals*

A first quality indication of the satellite cloud-phase determination methods was achieved by comparing instantaneous water and ice retrievals to collocated retrievals from the ground-based algorithm. Hereinafter, the word 'collocated' is used to indicate both the spatial collocation and the synchronization of two measurements. To quantify the detection accuracy of

satellite cloud-phase retrievals for different ground-observed cloud thicknesses, the ground ice cloud dataset was sorted into groups of cloud cases with the 30-minute averaged ice cloud thickness from >200 m to >5000 m. The water cloud cases were grouped into classes with ≤200 m to ≤2500 m of ice cloud overhead. For these instantaneous water and ice cases the bias in the satellite-retrieved cloud phase was determined.

Satellite data were obtained from the two pixels nearest to the Cabauw geolocation. Roebeling et al. (2006b) showed that the difference between simulated SEVIRI and ground-based LWP values has a minimum at a ground tracklength of ~4 km. Taking into account the westerly airflow, which dominates the Western European climate, and the SEVIRI pixel size of 4×7 km at the Cabauw geolocation, the validation area comprises the Cabauw pixel and the pixel west of Cabauw.

From the one-year dataset, collocated cases (both spatially and temporally) with a ground-based cloud cover >90% and labeled as either water or ice by both satellite and ground-based observations were selected. Subsequently, the collocated cases were compared. For both water and ice, the number of cases with satellite cloud-phase retrievals being different from the ground-observed value divided by the total number of collocated water (ice) cases indicates the bias for instantaneous water (ice) retrievals.

*Monthly liquid water and ice cloud occurrence frequency*

To examine the accuracy of the various methods with respect to climate monitoring purposes, the monthly averaged water and ice cloud occurrence frequency, $\overline{\varphi}^{w}_{m}$ and $\overline{\varphi}^{i}_{m}$, defined as the ratio of clouds labeled as water or ice to the total observed clouds, was calculated. The superscript $p$ is hereinafter used to generically denote water and ice. Using the criteria from Table 3.2, the daily water and ice cloud occurrence frequency were calculated first:

$$\varphi_d = \frac{n^p_d}{N_d}, \tag{3.4}$$

with $n^p_d$ and $N_d$ the number of observed water or ice clouds and total number of clouds at a day, respectively.

The monthly averaged occurrence frequency was calculated using a three-month moving window. Because the number of available collocated time slots changed significantly for each day, a weighting factor, $w_d$, was defined:

$$w_d = \frac{n_d}{\sum_{d=0}^{n} n_d}, \tag{3.5}$$

with $n_d$ the number of collocated time slots at day $d$ having a ground-based derived cloud cover >90% and at least one satellite validation pixel cloud flagged. For both the SEVIRI and ground-based data, the monthly averaged water and ice cloud occurrence frequency, $\overline{\varphi}^{p}_{m}$, was calculated as follows:

$$\overline{\varphi^p_m} = \frac{n^p_m}{N_m}, \tag{3.6}$$

with $n_m^p$ being the number of observed water or ice clouds and $N_m$ being the total observed clouds within the three-month moving window.

The main accuracy indicator is the monthly bias in water and ice cloud occurrence frequency, $B_m^p$:

$$B_m^p = \overline{\varphi_{m,sat}^p} - \overline{\varphi_{m,sur}^p}, \tag{3.7}$$

with suffixes $m,sat$ and $m,sur$ referring to the monthly satellite and surface derived water and ice cloud occurrence frequency, respectively.

The weighted unbiased root-mean-square error, $URMSE$, is used as a precision measure and indicates the spread in the differences between daily satellite and ground-observed water or ice cloud occurrence frequency after removing the monthly bias:

$$URMSE = \sqrt{\sum_{d=0}^{n} w_d \left[\varphi_{d,sat}^p - B_m^p - \varphi_{d,sur}^p\right]^2}. \tag{3.8}$$

A second precision indicator of the satellite-retrieved daily measurements is the linear correlation coefficient. To account for the different weights given to each day, the correlation coefficient was calculated using the product of $w_d$ and $\varphi_d^p$. The correlation coefficient for the water and ice cloud occurrence frequency is calculated as follows:

$$r = \frac{cov\left[(\varphi_d^p w_d)_{sat}, (\varphi_d^p w_d)_{sur}\right]}{\sigma_{sur}^p \sigma_{sat}^p} \tag{3.9}$$

A high correlation between the satellite and surface water or ice cloud occurrence frequency indicates a good skill of the satellite method.

### *Daytime diurnal cycle of cloud phase*

To assess the methods' ability for detecting the daytime diurnal cycle of cloud phase, a four-month period during the summer season (May-August 2004) was investigated. This period was chosen because in the western European coastal climate region, in which Cabauw is located, cloud formation during summer is mostly induced by convection and to a lesser degree by synoptic-scale systems. Therefore it is expected that as a result of enhanced convection during the afternoon, the ice cloud occurrence frequency increases accordingly.

All cases with ground-based observed cloud cover >90% were collected and binned into 15-minute observation time categories for the period 6:12-18:12 UTC (8:12-20:12 Central European Summer Time). For each bin the average water and ice cloud occurrence frequency was calculated. Subsequently, the correlation coefficient between satellite and surface methods was calculated. The error in the obtained correlation coefficient was calculated using a bootstrap technique. This technique uses the actual dataset to construct synthetic datasets by randomly drawing values from the original data (Efron and Tibshirani 1993).

## 3.4 Results

### 3.4.1 Instantaneous cloud-phase retrievals

The satellite-based cloud-phase retrieval is expected to perform better with increasing (optical) thickness of the observed cloud layer. In order to test this hypothesis, the accuracies of the satellite-based ice phase retrievals are determined for ground-based observed ice clouds with a geometrical thickness increasing from 200 m to 5000 m. It is likely that the bias for the satellite ice cloud retrievals will decrease with increasing ice cloud geometrical thickness over the ground-based sites. The SEVIRI cloud-phase retrievals are insensitive to geometrically thin (subvisual) ice clouds ($\tau_{0.6} \lesssim 1$), for which the SEVIRI cloud-phase retrievals are rather influenced by the water cloud or surface underneath. This may result in the incorrect retrieval of the water phase. Likewise, the accuracy of the satellite water phase retrievals is determined for ground-observed water clouds with an increasing ice cloud thickness overhead. For the validation of water clouds, an increasing ice thickness implies that more ice over water is allowed before the ground-based observed cloud phase is switched from water to the mixed phase category. It is therefore expected that with an increasing ice over water cloud thickness the number of satellite ice cloud retrievals will increase, hence increasing the bias with the ground-observed cloud phase.

Figure 3.4 presents results for the instantaneous satellite cloud phase retrievals for May 2004–April 2005. Results are obtained for ground-based ice clouds with an increasing geometrical thickness and for water clouds with an increasing ice geometrical thickness overhead. The results for water clouds are plotted in gray, while the results for ice clouds are plotted in black. Values on the x-axis indicate the maximum and minimum ice cloud thickness for ground-observed water and ice clouds, respectively. Please note that the datasets are not equal in size, as the water cloud dataset comprises ground observed water clouds with ice clouds aloft and the ice cloud dataset contains ground observed ice clouds, which do not necessarily have water clouds below.

From Figure 3.4 it can be seen that the satellite cloud phase-retrieval methods show small bias when almost pure water clouds (with ≤200 m ice overhead) are observed from the surface, with values of 4%, 7%, and 10% for the CM-SAF, MODIS-like, and ISCCP-like methods, respectively. The relatively high value for the ISCCP-like method is probably connected to the usage of 260 K as threshold, which fails to detect water clouds that exist at lower temperatures. Hogan et al. (2003) showed that the supercooled water occurrence frequency decreases from 27% towards 0% at temperatures between 268 K and 238 K, using ground-based lidar observations at Chilbolton (United Kingdom). As the ground-observed ice cloud thickness over water clouds increases, the bias increases for all methods. This increase indicates that the satellite methods tend to retrieve ice more often with increasing ground observed ice cloud thickness over water clouds. The MODIS- and ISCCP-like methods are slightly more sensitive to an increase in ice thickness than the CM-SAF method, which is seen from the larger increase in bias than CM-SAF between >500 m and >1500 m ice cloud thickness. Once the ground-observed ice cloud thickness exceeds 1500 m, all methods show a similar increase in bias.

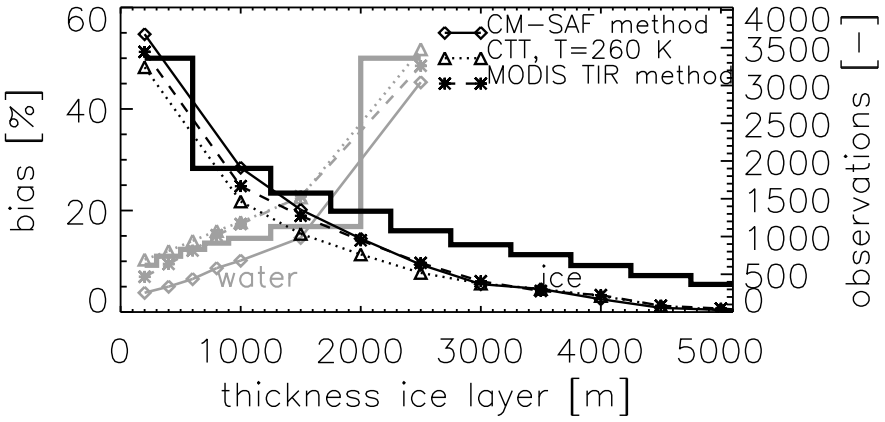


**Figure 3.4** *Bias between instantaneous satellite and ground-based cloud-phase retrievals for water (gray) and ice (black). The x-axis values indicate the maximum and minimum ice layer thickness for ground-based observed water and ice clouds, respectively. The CM-SAF method is plotted solid, the ISCCP-like method dotted, and the MODIS-like method dashed. The histograms indicate the number of collocated observations with scaling on the right-hand axis.*

The ice cloud retrieval results show an opposite behavior when ground-observed ice thickness increases. If ground-observed clouds with an average ice thickness >200 m are labeled as ice, the bias for the satellite methods is 50-55%, due to the SEVIRI spectral channels not being able to detect very thin ice clouds. However, at increasing minimum ice thickness the bias decreases sharply; for clouds with ice thickness >3500 m, the bias for the three methods diminishes to within 5%. Above results indicate that all methods have good skill for instantaneous retrievals if only thick, homogeneous water and ice clouds are considered.

### 3.4.2 Monthly liquid water and ice cloud occurrence frequency

The monthly averaged liquid water and ice cloud occurrence frequency is used to monitor the annual variations in cloud phase. Figure 3.5 shows the monthly averaged distribution between water, ice, and mixed phase clouds as derived from ground-based measurements using a three-month moving window. Water clouds overlaid by <600 m ice are still considered water; clouds with ice thickness >2500 m are labeled ice (see also Table 3.2). The remaining cases are labeled mixed phase.

The ice cloud occurrence frequency peaks during the late summer, which could be related to convective activity mostly taking place in the Western European climate in these months. The maximum water cloud occurrence frequency is observed in November 2004, which is probably connected to more synoptical weather systems moving over the Cabauw site. The mixed phase cloud occurrence frequency gradually increases towards the winter months from 30% to ~60%, which is likely due to more supercooled water clouds within the synoptic-scale systems. It was

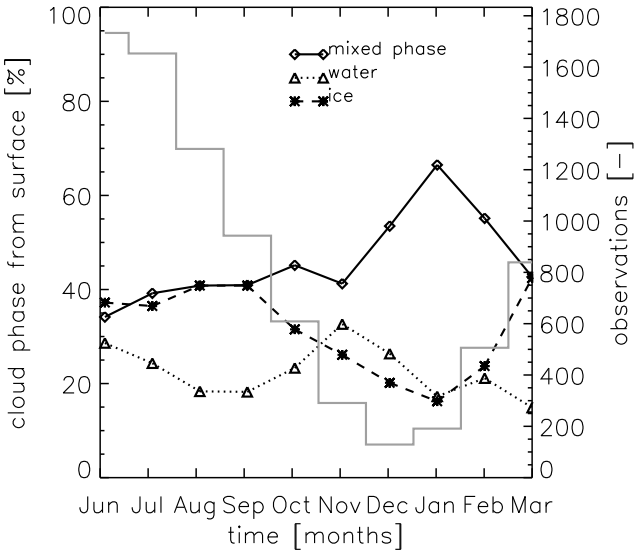


**Figure 3.5** *Monthly averages of ground-based derived liquid water (dotted), ice (dashed), and mixed phase (solid) clouds using a three-month moving window. Clouds are labeled as ice for 30-minute average thickness >2500 m, water clouds contain <600 m of ice overhead (see also Table 3.2). The gray histogram indicates the number of valid observations for each three-month period.*

shown by Rauber and Tokay (1991) that supercooled water layers are most likely to occur in non-convective clouds. Corresponding results were reported by Naud et al. (2006), who found that glaciation in mid-latitude storms occurs at lower temperatures for shallow clouds outside the frontal regions. Note that the number of observations, indicated by the gray histogram, is strongly skewed towards the summer months, which implies that occurrence frequencies obtained for the winter months are significantly less reliable.

The monthly water and ice cloud occurrence frequency for the satellite methods and the ground-based reference dataset are given in Figures 3.6a and 3.6d. The water and ice cloud occurrence frequency are shown in the left and right panel, respectively. Further, the monthly URMSE (see Equation 3.8) is presented in Figures 3.6b and 3.6e. It is mentioned that due to the limited visible channel information the number of observations is low for November 2004–January 2005 (see also Figure 3.5). The ground-observed water occurrence frequency decreases during the summer months, having a minimum in September 2004. The decline (increase) in water (ice) occurrence frequency is likely related to summer convection. Water occurrence frequency increases towards the (boreal) winter months, which may be connected to dominating synoptic-scale weather systems in the Western European climate region.

All methods show very small bias (<5%) throughout the summer months. Towards autumn and winter, both the ISCCP- and MODIS-like methods predict a lower water occurrence frequency than the ground-based observed value. For the ISCCP-like method, this underestimation could

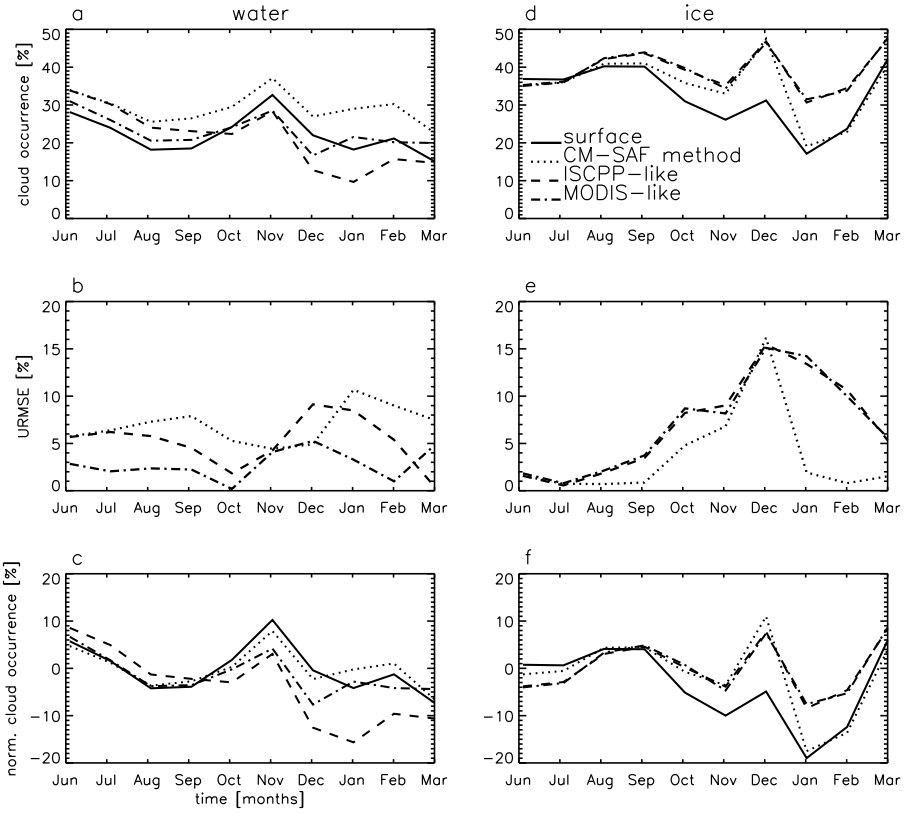


**Figure 3.6** *(a,d) Monthly averaged liquid water and ice cloud occurrence frequency for the SEVIRI methods and ground-based method; (b,e) unbiased root-mean-square error (URMSE) for the SEVIRI methods; (c,f) liquid water and ice cloud occurrence frequency for the SEVIRI methods and ground-based method normalized by the respective yearly average. Liquid water cloud and ice cloud results are shown in the left and right panels, respectively. Results were obtained using a three-month moving window.*

be related to differences in cloud dynamics between summer and winter (convectively versus synoptically induced clouds) and thus more water clouds existing at temperatures lower than the 260 K threshold (Hogan et al. 2003; Rauber and Tokay 1991). The CM-SAF method has a continuous positive bias of ~8% for almost the entire year. URMSE is small for all methods, with a slight increase towards the winter months. For the CM-SAF and ISCCP-like methods this could be related to unfavorable viewing geometries (large solar and viewing zenith angles), which affect the accuracy of simulated 0.6- and 1.6-$\mu$m reflectances and hence the precision of the cloud-phase retrieval. The MODIS-like method mostly has a smaller URMSE (higher precision) than the CM-SAF and ISCCP-like methods.

The derived ice cloud occurrence frequency shows a similar pattern for the summer months. Towards winter, all methods have a decrease in both accuracy and precision, as seen by the

increase in bias and URMSE. In December 2004, all methods overestimate the ground-based derived ice cloud occurrence frequency by ~15%, together with an increase in URMSE from ~2% in September to 16% in December 2004.

The increase in URMSE indicates a larger spread of the differences between daily satellite and ground-based derived ice cloud occurrence frequency, which is partly related to substantially less collocated observations compared to the summer months. The precision of the CM-SAF method significantly improves after December 2004, as the URMSE drops from 16% to ~3%. This indicates that the precision of cloud-phase determination using visible and near-infrared reflectance is largely influenced by the viewing geometry. For the ISCCP-like method, the overestimation of ice clouds during the winter coincides with an underestimation of water clouds, which suggests that 260 K is a too high temperature threshold to accurately estimate the monthly average of cloud phase during winter in a mid-latitude climate. Except for the large positive bias from October–December 2004, the CM-SAF method is best capable of detecting the ground-based observed ice cloud occurrence frequency.

To assess the methods' ability for reproducing the ground-based observed annual cycle in cloud phase, Figures 3.6c and 3.6f show the monthly averaged water and ice cloud occurrence frequency normalized by its yearly average in the left and right panel, respectively. For water clouds, the CM-SAF method almost perfectly detects the monthly variability in occurrence frequency as observed by the ground-based algorithm, probably linked to the usage of 0.6- and 1.6-$\mu$m reflectance which enables a more direct cloud-phase observation than temperature thresholding methods. During autumn and winter, the ISCCP-like method reproduces the annual cycle in water cloud occurrence frequency less clearly, which can be seen in Figure 3.6c from November 2004 onwards. For ice clouds, all methods reproduce the monthly variability well during summer. In the winter months, this ability decreases, although the CM-SAF method approaches the ground-observed ice cloud occurrence frequency again from January 2005 onwards.

Weighted correlation coefficients for the retrieved daily water and ice cloud occurrence frequencies are presented in Figure 3.7. All methods have a high correlation (>0.8) for the summer months and show a decrease during the winter months for both water and ice. Further, the correlation between satellite methods and ground-based observations is higher for ice cloud than for water cloud occurrence frequency, with almost similar correlation coefficients for all methods. Correlation coefficients are very high (>0.9) until December 2004, followed by a decrease to ~0.75 during the winter. For the water cloud occurrence frequency, the ISCCP-like method shows a sharper drop in correlation than the CM-SAF and MODIS-like methods. Note that from December 2004 to January 2005 the number of observations is very low, which makes the correlations more susceptible to outliers. Table 3.3 presents the weighted correlation coefficients for the entire dataset together with values obtained from a bootstrap technique (Efron and Tibshirani 1993), which gives information on the reliability of the obtained correlations.

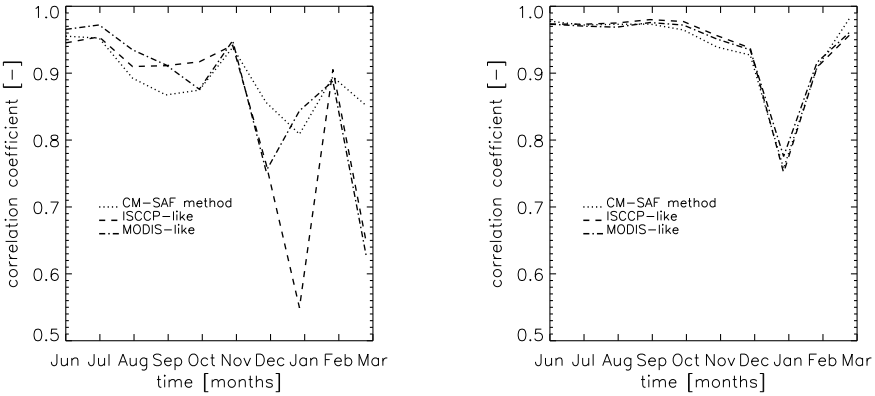


**Figure 3.7** *Monthly weighted correlation coefficients based on daily averaged water (left panel) and ice (right panel) occurrence frequency using a three-month moving window for CM-SAF (dotted), ISCCP-like (dashed), and MODIS-like (dashed-dotted) methods.*

**Table 3.3** *Weighted correlation coefficients ($r_0$) and median bootstrap correlation ($r_b$) with standard deviation between satellite and ground-based derived water and ice cloud occurrence frequency for May 2004–April 2005.*

| method | $r_{0,\text{water}}$ | $r_{\text{b,water}}$ | $r_{0,\text{ice}}$ | $r_{\text{b,ice}}$ |
|---|---|---|---|---|
| CM-SAF | 0.94 | 0.93±0.02 | 0.98 | 0.93±0.02 |
| ISCCP-like | 0.92 | 0.91±0.03 | 0.97 | 0.91±0.03 |
| MODIS-like | 0.92 | 0.91±0.03 | 0.97 | 0.91±0.03 |

### 3.4.3 Daytime diurnal cycle of cloud phase

Figure 3.8 shows the ground-based and satellite derived daytime diurnal cycle of water (left panel) and ice occurrence frequency (right panel) for May-August 2004. Results are shown for one-hour binned observations, while calculations of the correlation between satellite- and ground-observed water and ice cloud occurrence frequency were performed using 15-minute binned data. The gray histogram denotes the number of collected observations for each hour from 6:12-18:12 UTC (8:12-20:12 Central European Summer Time, CEST).

During the morning and early afternoon, the ground-based observed water occurrence frequency is approximately constant (~40%), while the ice cloud occurrence frequency shows a small increase. The water cloud occurrence frequency derived by the CM-SAF and ISCPP-like methods shows a strong peak from 11:12 to 12:12 UTC. This could be due to a backscatter geometry effect; azimuth difference angles in this period are 160°–180°. Because the LUT reflectances are less accurate for these unfavorable backscatter viewing geometries, for the CM-SAF method the increased 0.6- and 1.6-$\mu$m reflectance may lead to more water retrievals. For the ISCCP-like method, increased 0.6-$\mu$m reflectance leads to a smaller cloud emissivity correction (see Equations 3.2 and 3.3), which in turn leads to a higher cloud-top temperature. After local noon (varying from 13:37-13:47 CEST), water (ice) occurrence gradually decreases

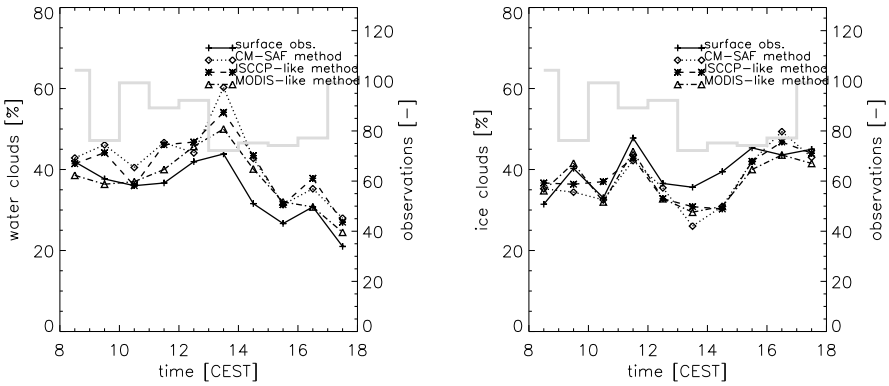


**Figure 3.8** *Daytime diurnal cycle of water (left panel) and ice (right panel) cloud occurrence frequency for SEVIRI methods versus ground-based observed values (solid line) for May-August 2004. Values are obtained from measurements binned over 1-hour periods from 6:12-18:12 UTC (8:12-20:12 CEST). The number of observations in each bin is denoted by the gray histogram, with scaling on the right-hand axis.*

(increases). This change in water and ice cloud occurrence frequency over the day is reproduced well by all methods, although some bias remains (~10%), mainly for the water cloud occurrence frequency. Further, the increase in ice cloud occurrence frequency after 13:12 CEST is reproduced with a small lag by the satellite methods, this could be due to the difference in spatial resolution between ground- and satellite-based measurements.

The correlation coefficients as obtained from the 15-minute binned observations are presented in Table 3.4. Correlation is significant for all methods for both the water and ice cloud occurrence frequency. As the original dataset was small (n=48), a bootstrap technique was used to assess the reliability of the obtained correlations. The standard deviation of the bootstrapped correlations is assumed to indicate the error of the original correlation $r_0$. For the 15-minute data, all $r_0$ values are within one standard deviation, which means that the correlation is reliable. For both the daytime diurnal cycle of water and ice cloud occurrence frequency, the MODIS-like method shows best performance with correlations of 0.89 and 0.86 for water and ice, respectively. The ISCCP-like and CM-SAF method have values between 0.67 and 0.76. The above values show significant skill for the number of data points used.

## 3.5 Conclusions

In this Chapter, three cloud-phase determination methods have been evaluated for their use in climate monitoring applications in mid-latitude coastal climate. The methods investigated are a MODIS-like thermal infrared method, an ISCCP-like method, and a method developed within the framework of the CM-SAF. Using one year of SEVIRI data (May 2004–April 2005), retrievals of the methods were compared to collocated ground-based cloud-phase retrievals from cloud radar and lidar data at Cabauw, The Netherlands. Three quality aspects of the satellite retrievals were evaluated:

**Table 3.4** *Correlation coefficients between the satellite and ground-based derived daytime diurnal cycle of water and ice cloud occurrence frequency for May–August 2004. $r_0$ represents the correlation using 15-minute binning of the original dataset (n=48), $r_b$ denotes the median bootstrap correlation with the standard deviation.*

| | $r_{0,\text{water}}$ | $r_{\text{b,water}}$ | $r_{0,\text{ice}}$ | $r_{\text{b,ice}}$ |
|---|---|---|---|---|
| CM-SAF | 0.73 | 0.74±0.06 | 0.67 | 0.67±0.09 |
| ISCCP-like | 0.76 | 0.76±0.07 | 0.70 | 0.70±0.07 |
| MODIS-like | 0.89 | 0.89±0.03 | 0.86 | 0.87±0.04 |

1) instantaneous cloud-phase retrievals, 2) monthly averaged water and ice cloud occurrence frequency, and 3) daytime diurnal cycle of cloud phase for May–August 2004.

The ground-based algorithm (Illingworth et al. 2007) used in this research retrieves cloud-phase information at a very high temporal resolution with a vertical range of ~12 km. This in contrast to satellite imagery, which mostly derives cloud-phase information from the uppermost part of a cloud. To account for these differences, ground-based cloud-phase retrievals were collected over 30-minute time windows. Furthermore, in order to obtain a straightforward comparison of satellite to ground-based derived cloud phase retrievals, the 30-minute averaged thickness of water, ice, and mixed phase layers was taken into account to label each time window period with a unique cloud phase.

Using the ground-based cloud phase dataset, it was shown that ice cloud occurrence frequency has a maximum during summer (~40%), probably due to convection, and a minimum during winter (~15%). The ground-based water cloud occurrence frequency peaks in November 2004 (~30%). The fraction of mixed-phase clouds gradually increases from 30% to ~60% towards the winter season, which could be related to synoptic-scale weather systems dominating the western European climate during winter. These systems contain substantial amounts of supercooled water clouds (Naud et al. 2006; Rauber and Tokay 1991).
All methods show small instantaneous bias for thick water and ice clouds with values within 5%. The ISCCP-like method has a larger bias for pure water clouds (~10%), which is likely due to the 260 K threshold leading to misdetection of water clouds existing at lower temperatures. Hogan et al. (2003) found that ~25% of ground-based lidar observed clouds at Chilbolton (United Kingdom) with temperatures lower than 258 K contain supercooled water layers.

For the dataset investigated, all methods show high precision in retrieving the water and ice cloud occurrence frequency during summer, with URMSE values mostly within 5%, and decreases during the winter months to 10-15%. The CM-SAF method is best capable of reproducing the annual cycle, mainly for the water cloud occurrence frequency, for which an almost constant positive bias of ~8% was found. This is largely coupled to the more direct observation of cloud phase due to the usage of visible and near-infrared reflectance. However, because this method can only be used during daytime, additional thermal infrared channel radiances are still required to obtain full-day coverage. The ISCCP- and MODIS-like methods reproduce the annual cycle accurately during the summer, but less clearly during the winter months.

For the ISCCP-like method this is probably connected to the indirect relation of cloud phase to cloud-top temperature. Especially during the winter months when clouds are more stratiform and are more likely to contain supercooled liquid water at temperatures <260 K, a considerable amount of water clouds may be misclassified. The usage of dynamical temperature thresholds depending on e.g. the cloud dynamics can improve the accuracy for detection of the monthly variability of cloud phase.

For May–August 2004, all methods are well capable of reproducing the daytime diurnal cycle of water and ice cloud occurrence. It was found that the MODIS-like method reproduces this cycle best, with correlations of 0.86 and 0.89 for the daytime diurnal water and ice cloud occurrence frequency, respectively. The CM-SAF and ISCCP-like methods have lower (~0.7), but still significant, correlation coefficients. The lower correlations compared to the MODIS-like method are likely linked to a lower signal-to-noise ratio and the usage of a temperature threshold for the CM-SAF and ISCCP-like method, respectively.

It is stressed that the very promising results were obtained over a mid-latitude coastal climate area using only one year of data. In order to obtain a high-quality global cloud-phase climatology and to evaluate the interannual variability of cloud phase, more research on cloud-phase determination using SEVIRI data over different climate regions and longer time periods is required. Furthermore, the accuracy of cloud-phase determination needs also to be assessed for nighttime scenes. Finally, the development and evaluation of mixed phase cloud categorization will be required as these clouds make up a significant part of all clouds.

# Chapter 4

## Broken and inhomogeneous cloud impact on satellite cloud property retrievals

The impact of sensor resolution on satellite-derived cloud particle effective radius ($r_e$) and cloud phase (CPH) for broken and overcast inhomogeneous clouds is investigated for the CPP retrieval algorithm used by the Climate Monitoring Satellite Application Facility (CM-SAF). First, synthetic datasets of high-resolution ($1\times1$ km$^2$) and low-resolution ($3\times3$ km$^2$) radiances are used to illustrate the effect on the $r_e$ and Cloud Top Temperature ($T_c$) retrieval, the cloud properties that are used for the CPH retrieval. It is shown that low-resolution $r_e$ can be overestimated by up to 12 $\mu$m and $T_c$ by up to 20 K for thick broken and inhomogeneous overcast water clouds over ocean and land surfaces. The overestimation of $r_e$ may cause erroneous assignments of 'ice' to 'water' clouds. Second, two months of CPP retrievals on Moderate-Resolution Imaging Spectroradiometer (MODIS) radiances are used to quantify the effect on $r_e$ and CPH over the Atlantic Ocean and Central Europe. Over both areas, the low-resolution $r_e$ is overestimated by up to 5 $\mu$m for broken and up to 2 $\mu$m for inhomogeneous overcast clouds. At low resolution, the fraction of water clouds is underestimated by 2.3% over the Atlantic Ocean and 0.6% over Central Europe. The increase of $T_c$ partly compensates for the increase in $r_e$ in the CPH retrievals at low resolution. If no $T_c$ information were used, the underestimation of the water cloud fraction would be 3.5% and 2.2% for the Atlantic Ocean and Central Europe, respectively. For inhomogeneous overcast clouds integrated over all inhomogeneity classes, the difference is -1.3% and -2.3% for Central Europe and Atlantic Ocean, respectively. Our results indicate that the retrieval of $r_e$ in the CPP algorithm is sensitive to satellite sensor resolution in case of broken clouds and inhomogeneous overcast clouds and that despite the large $r_e$ sensitivity the CPH retrieval is much less sensitive to sensor resolution.

Based on: Wolters, E.L.A., H.M. Deneke, B.J.J.M. van den Hurk, J.F. Meirink, and R.A. Roebeling, 2010: Broken and inhomogeneous cloud impact on satellite cloud particle effective radius and cloud-phase retrievals, *J. Geophys. Res.*, **115**, D10214, doi:10.1029/2009JD012205.

## 4.1 Introduction

Clouds strongly affect the Earth's surface energy budget by reflection and absorption of solar and thermal radiation. The way this budget is modulated depends among others on the particle size distribution, height, and thermodynamic phase of clouds. Water and ice clouds have different radiative properties. For water clouds, the dominant effect is the reflection of incoming shortwave radiation and hence a cooling of the atmosphere, whereas for ice clouds absorption and emission of outgoing terrestrial radiation is dominant, which causes a net warming (Arking 1991; Hansen et al. 1997). In spite of clouds' great importance, cloud representation in climate models is fairly simplified, owing to both lacking knowledge of the spatiotemporal variation of the various cloud properties and computational constraints.

One of the basic properties necessary for the development of accurate cloud parameterizations is the global distribution of cloud thermodynamic phase, i.e., whether a cloud is composed of either ice or water particles or a combination of both. As noted by Naud et al. (2006) in a large-scale assessment of cloud phase and its relationship to atmospheric circulation on climatological time scales, the meteorological conditions in which supercooled liquid water droplets change into ice particles vary widely. A better understanding of cloud phase in both stratiform and cumuliform clouds is necessary for understanding the cloud phase–temperature relationship in the context of diagnosed microphysical processes (Del Genio et al. 1996). Roebeling and van Meijgaard (2009) evaluated the parameterization of cloud amount, condensed water path (CWP), and cloud phase (CPH) in the Regional Atmospheric Climate Model version 2, [RACMO2, Lenderink et al. (2003)] with corresponding datasets obtained from the Spinning Enhanced Visible and Infrared Radiometer Instrument (SEVIRI) onboard the Meteosat-8 and -9 satellites. It was found that, in general, RACMO2 overestimates the amount of ice clouds by about 20%. Weidle and Wernli (2008) compared spatial and temporal cloud-phase patterns of the European Center for Midrange Weather Forecasts (ECMWF) 40-yr Reanalysis (ERA-40) data over Europe against cloud-phase observations from the POLarization and Directionality of the Earth's Reflectances 1 (POLDER-1) satellite instrument. It was concluded that agreement between the two datasets is good for water and ice clouds, however, the ERA-40 dataset contains too many ice clouds for clouds labeled 'mixed phase' by POLDER-1.

During the last decades, several cloud-phase retrieval methods from passive imagery data have been proposed using multispectral measurements at solar and infrared wavelengths. Some methods are based on the principle that at near-infrared wavelengths ice particles absorb solar radiation more effectively than water droplets (Key and Intrieri 2000; Knap et al. 2002; Pilewskie and Twomey 1987; Platnick et al. 2003), while other approaches employ thermal infrared-only wavelengths (Baum et al. 2003; 2000; Strabala et al. 1994; Turner et al. 2003). The global distribution of cloud thermodynamic phase can among others be obtained using data from the Moderate-Resolution Imaging Spectroradiometer (MODIS) onboard the National Aeronautics and Space Administration (NASA) Earth Observing System (EOS) Terra and Aqua satellites.

To discriminate water from ice clouds within the Climate Monitoring Satellite Application Facility [CM-SAF, Schulz et al. (2009a)] of the European Organization for the Exploitation of

Meteorological Satellites (EUMETSAT), a technique was developed using data from visible (0.6 $\mu$m), near-infrared (1.6 $\mu$m), and thermal infrared (10.8 $\mu$m) spectral channels (Roebeling et al. 2006a). The CM-SAF cloud-phase determination algorithm has been compared to a one-year dataset of cloud phase obtained from ground-based cloud radar and lidar observations at the Cabauw CloudNET station, The Netherlands [see Illingworth et al. (2007) for more information on CloudNET]. Resulting accuracy (bias) and precision (standard deviation) of the method were established to be <10% and <5%, respectively (Schulz et al. 2009b; Wolters et al. 2008).

Passive satellite cloud property retrieval techniques rely on the assumption that the observed radiance originates from plane-parallel clouds covering the entire pixel. As a result, when clouds only partly cover a pixel, the observed radiances are a weighted average of the cloudy and cloud-free parts. The contribution of the cloudy part to the total observed radiance depends among others on the fractional cloud coverage, cloud thickness, and albedo of the underlying surface. For broken clouds overlaying a dark surface, the observed radiance at visible and near-infrared wavelengths is reduced due to the clear-sky contribution. As a result, the obtained cloud optical thickness (from the visible) is underestimated and cloud particle effective radius ($r_e$, from the near-infrared) is overestimated [see e.g. Barker and Liu (1995),Oreopoulos and Davies (1998), and Coakley et al. (2005)].
In recent years, mainly the 3D effects of cloud property retrievals have been investigated [see for example Marshak et al. (2006) and Iwabuchi and Hayasaka (2002) for an evaluation of 3D radiative effects on $r_e$ and $\tau$ retrievals, respectively]. However, the effects of 3D radiative transfer are currently not accounted for in operational cloud property retrievals, both due to computational constraints and due to the fundamental under-determinedness of the inversion process (Stephens and Kummerow 2007).

At present, a considerable amount of cloud physical property climatologies are derived from geostationary satellite instruments, such as SEVIRI and the Geostationary Operational Environmental Satellite (GOES), as well as polar-orbiting satellite imagers such as the Advanced Very High Resolution Radiometer (AVHRR) and MODIS. These platforms differ in sensor resolution, with values of 3×3–5×5 km$^2$ and 1×1 km$^2$ for the former and latter, respectively. As about 20% of the clouds are broken clouds as observed at geostationary satellite resolution (Deneke et al. 2009), and because these clouds have small-scale variability resulting from e.g. convective updrafts, it can be questioned to what extent the obtained $r_e$ and cloud phase climatologies at geostationary resolution are influenced by broken cloud fields and inhomogeneous clouds compared to climatologies obtained at polar satellite resolution (with a typical nadir sampling resolution of 1×1 km$^2$). The quantification of the difference between low- and high-resolution cloud physical properties retrievals over various surfaces and for various cloud fractions could serve as a baseline for correcting the low-resolution cloud climatologies. In addition, the difference between low- and high-resolution cloud-phase retrievals can have significant impact on the calculation of the cloud radiative forcing (Oreopoulos et al. 2009).

In this Chapter the impact of broken clouds and overcast inhomogeneous clouds on the retrievals of cloud particle effective radius ($r_e$) and cloud phase from low-resolution satellite radiances is investigated. The impact of sensor resolution on low-resolution (3×3 km$^2$ at nadir, but typically 4×7 km$^2$ at ~50°N) satellite-derived cloud particle effective radius ($r_e$) and cloud

phase (CPH) for broken and overcast inhomogeneous clouds is investigated for the Cloud Physical Properties (CPP) retrieval algorithm used by the CM-SAF. The results presented are limited to a description of differences in retrieved cloud physical properties at two resolutions. The physical causes of these differences are outside the scope of this research and are subject to future investigations. Other retrieval algorithms exist that may reveal different sensitivities to resolution degradation, but the selected application illustrates the various relevant processes playing a role.

First, the impact of broken cloudiness and cloud inhomogeneity on the cloud particle $r_e$ retrieval is scrutinized using synthetic datasets. Both the cloud-phase and $r_e$ retrieval of the CPP algorithm rely on an estimate of the particle absorption, which is affected by unresolved variability. Second, for May and August 2007 low- and high-resolution retrievals are obtained from MODIS in two climate regions (subtropical ocean and mid-latitude land). These retrievals are interpreted in the context of the synthetic datasets and the effects on $r_e$ and cloud-phase retrievals are quantified.

The outline of the paper is as follows. Section 4.2 describes the various MODIS datasets, the CPP algorithm, and the experimental setup of the simulations and retrievals from MODIS radiances. In section 4.3, the synthetically obtained datasets as well as the comparison of MODIS high- and low-resolution retrievals against these synthetic datasets are shown. Finally, a discussion and conclusions are provided in section 4.4.

## 4.2 Data and methods

### 4.2.1 MODIS data

MODIS is an imager onboard the polar orbiting Terra (equatorial overpass at 10:30 local time) and Aqua (equatorial overpass at 13:30 local time) satellites. It has 36 onboard calibrated spectral channels with central wavelengths at 0.42–14.4 $\mu$m; spatial resolutions are 250×250 m$^2$ for bands 1 and 2 (0.65 $\mu$m and 0.86 $\mu$m), 500×500 m$^2$ for bands 3–7 (0.47–2.13 $\mu$m), and 1× km$^2$ for bands 8–36 (4.12–14.4 $\mu$m). The data used in this study are the 1 km Level-1B reflectance and radiance data (MOD021KM and MYD021KM for Terra and Aqua, respectively) from bands 1 (0.65 $\mu$m), 6 (1.64 $\mu$m), and 31 (11.0 $\mu$m).

Over land, surface albedo information was obtained from 16-day MODIS white-sky albedo maps (the bihemispherical reflectance under conditions of isotropic illumination, MCD43B3 Collection 5 data files). Although we realized that for certain broken cloud cases the usage of a white sky albedo might be less appropriate, these maps were used for both overcast and broken cloud cases.

Over ocean, an albedo of 0.05 was assumed for both the 0.65-$\mu$m and 1.64-$\mu$m channel, independent on solar zenith angle. It was shown from Scanning Imaging Absorption Spectrometer for Atmospheric Cartography (SCIAMACHY) spectra that ocean surfaces have a similar reflectance at both visible and near-infrared spectral channels [see Figure 2 in Roebeling et al.

(2006a)]. Collected data were limited to viewing and solar zenith angles ($\theta$ and $\theta_\circ$, respectively) within 60°, because the accuracy and precision of retrieved cloud physical properties decrease for very large $\theta$ and $\theta_\circ$ (Loeb and Coakley 1998; Roebeling et al. 2008; Wolters et al. 2008).

### 4.2.2 CPP retrieval algorithm

In this paper, the CPP algorithm of the CM-SAF is used to retrieve $r_e$ and cloud thermodynamic phase (Roebeling et al. 2006a) from visible, near-infrared, and infrared radiances. The algorithm is operationally applied to radiances observed from SEVIRI onboard Meteosat-8 and -9 and AVHRR onboard the National Oceanic and Atmospheric Administration (NOAA) satellites. Recent developments enable application of the CPP algorithm to the (nearly) corresponding visible, near-infrared, and infrared spectral channels of MODIS (Deneke et al. 2009).

#### *Cloud masking procedure*

In order to clearly focus on the effects of resolution degradation, we applied a simple, but equivalent cloud mask for both the high- and low- resolution retrievals. This cloud mask is based on the comparison between pixel and clear sky surface (MODIS white-sky albedo) reflectance. Pixels were flagged 'cloudy' if the observed 0.6- and 1.6-$\mu$m reflectance exceeded the clear-sky value by a predefined threshold value i.e., $R_{0.6} > (WS_{0.6} +$ threshold) and $R_{1.6} > (WS_{1.6} +$threshold), with $R$ and $WS$ referring to the observed reflectance and white-sky albedo, respectively.

#### *Retrieval of $\tau$ and $r_e$*

The CPP algorithm relies on the principle that reflectances in the non-absorbing visible spectral channels (0.6 $\mu$m or 0.8 $\mu$m) are largely determined by cloud optical thickness. In contrast, reflectances in the absorbing near-infrared spectral channels (e.g. 1.6 $\mu$m, 2.2 $\mu$m, and 3.8 $\mu$m) are also sensitive to the single scattering albedo of cloud particles, which in turn is a function of cloud particle size and the imaginary part of the refractive index of the cloud particles (Nakajima and King 1990; Platnick et al. 2003).

Cloud optical thickness and cloud particle effective radius are retrieved simultaneously through an iterative comparison of the observed 0.6-$\mu$m and 1.6-$\mu$m reflectances with Lookup Tables (LUTs) of simulated Radiative Transfer Model (RTM) reflectances for given cloud optical thickness, particle effective radius, and surface albedos for water and ice clouds (Roebeling et al. 2006a). To retrieve $\tau$ and $r_e$, the iteration scheme first searches the LUT for ice clouds, and if no convergence is found, the LUT for water clouds is searched. It is noted that some overlap between large water droplets and small ice crystals causes ambiguities in the phase assignment. In this case, the retrieved $\tau$ and $r_e$ values for ice clouds are chosen for pixels when the Cloud Top Temperature ($T_c$) is smaller than 265 K, while the $\tau$ and $r_e$ values for water clouds are chosen for the remaining pixels. In the default CPP algorithm, effective radius values for water (ice) clouds with $\tau < 8$ are relaxed to a climatological value of 8 $\mu$m (26 $\mu$m), because the $r_e$ retrieval can become ambiguous for such clouds when using a two-channel algorithm

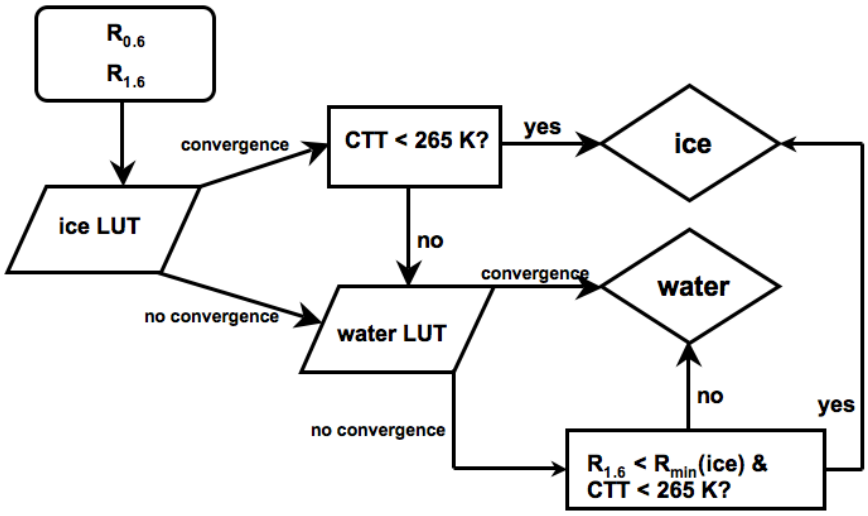


**Figure 4.1** *Flowchart of the cloud-phase retrieval algorithm.*

(Nakajima and King 1990). In this paper the relaxation of $r_e$ values to climatological values has been switched off to properly study the effect of broken clouds on the low-resolution $r_e$ retrieval, as otherwise for optically thin clouds $r_e$ values close to the relaxation value of 8 $\mu$m would be retrieved.

*Retrieval of cloud phase*

The retrieval of cloud phase is embedded in the $\tau$ and $r_e$ iteration scheme of the CPP algorithm. The logical flow of the cloud-phase retrieval algorithm is presented in Figure 4.1. The phases 'water' and 'ice' are assigned to pixels for which the measured 0.6-$\mu$m and 1.6-$\mu$m reflectances correspond to the respective simulated LUT reflectances. In other words, if the $\tau$ and $r_e$ retrieval converges for ice clouds, phase 'ice' is assigned, while phase 'water' is assigned to the remaining cloudy pixels. Further, a $T_c$ check is included. The assignment of phase 'ice' is only allowed for $T_c < 265$ K. In about 5% of the cases the $r_e$ retrievals do not converge for either water or ice clouds.

In these cases, phase 'ice' is assigned to a pixel with a 1.6-$\mu$m reflectance lower than the reflectance of an ice cloud with the largest ice crystals and a $T_c$ lower than 265 K, while phase 'water' is assigned to the remaining cloudy pixels. Note that the retrieved cloud phase is not representative for the entire vertical extent of a cloud, but mostly for the cloud top.

The $T_c$ is obtained by correcting the measured 10.8-$\mu$m (or 11.0-$\mu$m in case of MODIS data) brightness temperature for cloud emissivities ($\varepsilon_c$) less than unity, using the ratio of visible to thermal infrared cloud optical thickness and neglecting thermal infrared scattering (Minnis et al. 1998). The emissivity correction is not entirely independent of the cloud phase, as the retrieved cloud optical thickness depends on the cloud phase initially retrieved from the LUT search. Because ice crystals have a lower asymmetry parameter (less forward scattering of incident radiation) than water droplets, a larger optical thickness is retrieved for ice clouds than for water clouds having the same reflectance.

To quantify the differences in $T_c$ due to using emissivity corrections for water or ice clouds, we applied the correction twice for about 15,000 cloud-flagged pixels. First, all clouds were assumed 'water', the second time they were assumed 'ice'. For clouds having $\tau < 4$ (corresponding to $\varepsilon_c < 0.86$) the average and maximum difference between the two $T_c$ datasets was 0.3 K and 0.7 K, respectively. Thus, it can be concluded that only a marginal dependency of the $T_c$ calculation on the initially retrieved cloud phase exists. Further, in order to avoid too low cloud-top temperatures being retrieved at low emissivity values, a maximum temperature difference of 10 K between the measured brightness temperature and the obtained cloud-top temperature is imposed. Cloud-flagged pixels initially assigned to the phase 'ice' are labeled 'water' if the cloud-top temperature is warmer than 265 K. Again, we note that in the cloud-phase retrieval $r_e$ is not relaxed to the climatological value.

#### *Radiative Transfer Model (RTM) simulations*

The LUT reflectances are simulated with the Doubling Adding KNMI [DAK, De Haan et al. (1987); Stammes (2001)] RTM. This model calculates the monochromatic top-of-atmosphere reflectance in the ultra violet, visible, and near infrared, assuming plane-parallel homogeneous clouds over a Lambertian surface. The phase function of water droplets is calculated using Mie theory for spherical particles assuming a Gamma size distribution (Hansen and Travis 1974) with effective radii of 1–24 $\mu$m, while ray tracing is used to calculate the phase function for four types of imperfect hexagonal crystals (with volume equivalent effective radii of 6, 12, 26, and 51 $\mu$m) of the Cirrus Optical Properties ice crystal library (Hess et al. 1998). Subsequently, the monochromatic DAK reflectances are converted into spectral band reflectances using measured SCIAMACHY spectra (Roebeling et al. 2006a).

### *4.2.3 Synthetic datasets*

Synthetic cloud datasets at high (1×1 km$^2$ nominal, MODIS-like) and low (3×3 km$^2$ nominal, SEVIRI-like) resolution were constructed to simulate the effects of a) broken clouds and b) overcast clouds with an inhomogeneous optical thickness on the retrievals of $r_e$, $T_c$ and CPH. For clarity, 'broken clouds' are defined here as partly cloudy pixels with a constant $\tau$ and $r_e$, while the term 'inhomogeneous' is used for overcast clouds with varying $\tau$.

The CPP algorithm is used for the cloud property retrievals. Because this algorithm is based on the independent pixel approximation (IPA), 3-dimensional cloud radiative effects, such as

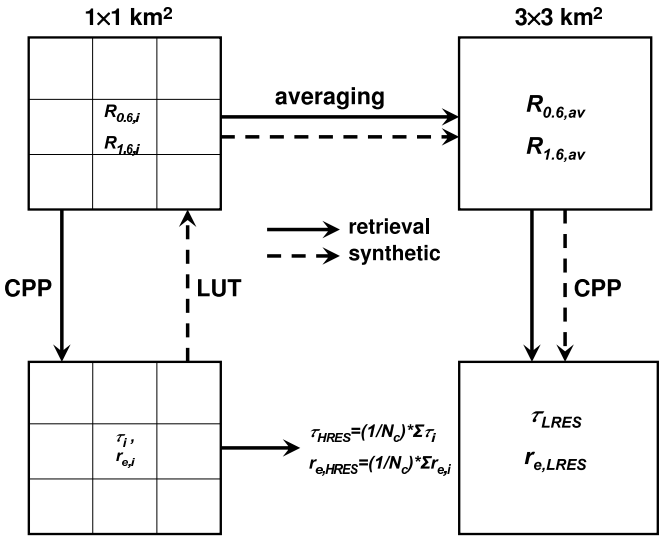


**Figure 4.2** *Schematic presentation of the (left) HRES and (right) LRES CPP simulation (indicated by the dashed lines) and retrieval (indicated by the solid lines) schemes. The CPP retrieval algorithm derives $\tau$, $r_e$, and CPH. The captions "1×1 km$^2$ " and "3×3 km$^2$ " refer to the MODIS and SEVIRI nadir spatial resolutions, respectively. $N_c$ denotes the number of cloudy pixels.*

horizontal photon transport, are not taken into account. The validity of IPA-based methods for these types of studies is discussed in more detail by e.g. Cahalan et al. (1994), Chambers et al. (1997b), and Chambers et al. (1997a). Hereafter, we refer to SEVIRI-like as low resolution and MODIS-like as high resolution, respectively. Further, we define the high-resolution cloud property retrievals averaged to low resolution as HRES and low-resolution retrievals based on radiances averaged to low resolution as LRES.

Figure 4.2 schematically presents the simulation and retrieval scheme for HRES and LRES, respectively. Solid lines denote the scheme for the retrievals from MODIS data, whereas the dashed lines indicate the flow for the synthetic simulations. For the broken and inhomogeneous cloud field simulations, the LUTs of the CPP algorithm were used to calculate the 0.6- and 1.6-$\mu$m reflectances (denoted $R_{0.6,i}$ and $R_{1.6,i}$ in Figure 4.2, respectively) for predefined high-resolution cloud optical thickness ($\tau_i$) and effective radius ($r_{e,i}$) values. $\tau_{\mathrm{HRES}}$ and $r_{\mathrm{e,HRES}}$ were computed by averaging $\tau_i$ and $r_{e,i}$ over a low-resolution (SEVIRI-like) pixel (see the lower middle box in Figure 4.2). $\tau_{\mathrm{LRES}}$ and $r_{\mathrm{e,LRES}}$ were retrieved from simulated SEVIRI-like reflectances (right arrow in Figure 4.2), which were calculated by averaging the 1×1-km MODIS reflectances to SEVIRI-like resolution (uppermost arrows in Figure 4.2).

*Broken cloud simulations*

Cloudy pixels were assigned $\tau_i$=8, $r_{e,i}$=12 $\mu$m to represent thin clouds and $\tau_i$=20, $r_{e,i}$=12 $\mu$m for thick clouds. These values were chosen based on observed frequency distributions of $\tau_{\mathrm{HRES}}$ and $r_{\mathrm{e,HRES}}$, shown later in Figure 4.5. Cloud-free pixels were assigned $\tau_i$=0. Because we assumed that broken clouds are homogeneous, $\tau_{\mathrm{HRES}}$=$\tau_i$ and $r_{\mathrm{e,HRES}}$=$r_{e,i}$.

Two surface types were considered, an ocean surface with surface albedo $\alpha_{0.6}$=$\alpha_{1.6}$=0.05 and a mid-latitude land surface with $\alpha_{0.6}$=0.10 and $\alpha_{1.6}$=0.20, with the latter values based on visual inspection of the MODIS white-sky albedo data. Once the low-resolution 0.6- and 1.6-$\mu$m reflectances were obtained, the CPP algorithm was used to retrieve $\tau_{\mathrm{LRES}}$ and $r_{\mathrm{e,LRES}}$. The simulations were performed for $\theta$=$\theta_\circ$=10° and azimuth difference angle $\varphi$-$\varphi_\circ$=100°. To assess the sensitivity of the simulations to surface albedo heterogeneity, the $\tau$ and $r_e$ simulations were repeated for a +/- 0.03 change in surface albedo at 0.6 $\mu$m and 1.6 $\mu$m, respectively. The $T_{c,LRES}$ was simulated assuming a $T_{c,i}$ of 270 K and surface temperatures of 280 K and 300 K over ocean and land surface, respectively. Cloudy and cloud-free brightness temperatures were averaged to simulate the brightness temperature at low resolution. Subsequently, $\tau_{\mathrm{LRES}}$ was used to calculate the cloud emissivity $\varepsilon_c$, after which the $T_{c,LRES}$ was computed.

*Inhomogeneous overcast cloud simulations*

The synthetic inhomogeneous cloud fields were prepared for completely overcast pixels. As for the synthetic broken cloud field data, the simulations were performed for an ensemble of thin and thick water cloud pixels. For thin clouds, $\tau_i$ was lognormally distributed around a median value ($\tau_{med}$) of 8 and $r_{e,i}$ was fixed at 12 $\mu$m, while for thick clouds $\tau_{med}$=15 and $r_{e,i}$=16 $\mu$m. The degree of inhomogeneity within a low-resolution pixel was varied by changing the spread around $\tau_{med}$, using the normalized interquartile range of $\tau_i$, hereafter referred to as $NIQR_\tau$:

$$NIQR_\tau = \frac{\tau_{75} - \tau_{25}}{\tau_{50}}, \tag{4.1}$$

with $\tau_{25}$, $\tau_{50}$, and $\tau_{75}$ denoting the 25-, 50- and 75-percentile value of the $\tau$ distribution, respectively. In case of homogeneous overcast clouds ($NIQR_\tau$=0), all $\tau_i$ and $r_{e,i}$ values were equal. For $NIQR_\tau > 0$, $\tau_i$ values were randomly drawn around the median values $\tau_{med}$=8 and $\tau_{med}$=15, respectively. The $\tau_i$ values to be drawn were constrained to match the desired $NIQR_\tau$ within a low-resolution pixel, spanning the range between 0.25 and 1.25. Because the $\tau_i$ values were randomly chosen, a large (500) number of pixels were generated. We chose to vary only $\tau_i$ (and not also $r_{e,i}$) because, as will be shown later in section 4.3.1, the observed variability in $\tau$ largely exceeds the observed variability in $r_e$.

To explain the impact of linearly averaging 0.6- and 1.6-$\mu$m reflectances on the LRES $r_e$ retrieval, Figure 4.3 shows the well-known Nakajima-King (Nakajima and King 1990) type plot for these spectral channel reflectances. The solid line denotes an arbitrary $r_e$ curve and the dotted line indicates a curve for a larger $r_e$. The diamond symbols represent two arbitrary 0.6- and 1.6-$\mu$m reflectance values for fixed $r_e$ and varying $\tau$. The linear averaging of the pixel reflectance values is indicated by the dashed line. Obviously, linear averaging of the 0.6- and 1.6-$\mu$m reflectances causes an overestimation of the cloud absorption at the low resolution, and thus

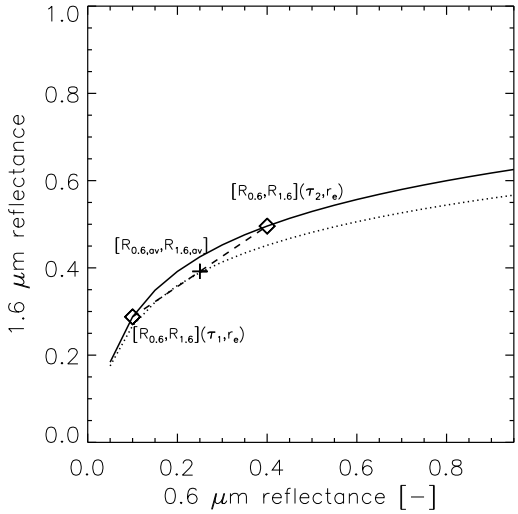


**Figure 4.3** *Conceptual plot of the effect of averaging reflectances on the low-resolution $r_e$ retrieval for varying $\tau$ and constant $r_e$. The solid line indicates an arbitrary $r_e$ curve. The diamonds denote the reflectance pairs $[R_{0.6},R_{1.6}]$ at $\tau_1$ and $\tau_2$. The cross shows the mean $[R_{0.6,av},R_{1.6,av}]$ value; the deviation from the solid line is obvious and leads to a larger low-resolution-retrieved $r_e$ (indicated by the dotted line).*

causes an overestimation of $r_e$. The deviation between low- and high-resolution-retrieved $r_e$ is among others dependent on the curvature of the $r_e$ curve.

### 4.2.4 Aggregation of MODIS observations

The cloud physical property datasets were retrieved for the areas shown in Figure 4.4 for May and August 2007 from MODIS Level-1 and -2 data with a version of the CPP algorithm that was adapted for using MODIS reflectances. $\tau_{\mathrm{HRES}}$, $\tau_{\mathrm{LRES}}$, $r_{\mathrm{e,HRES}}$, $r_{\mathrm{e,LRES}}$, $\mathrm{CPH}_{\mathrm{HRES}}$, and $\mathrm{CPH}_{\mathrm{LRES}}$ were obtained following the procedure described in Figure 4.2. As indicated in section 4.2.1, we applied a rather simple cloud masking technique based on the observed clear-sky reflectances at 0.6 $\mu$m and 1.6 $\mu$m. The HRES CPP retrievals were computed by averaging the 1×1-km$^2$ $\tau_i$ and $r_{e,i}$ over a SEVIRI pixel.

LRES retrievals were obtained from MODIS 1×1-km$^2$ radiances and surface albedos, which were averaged to the SEVIRI resolution. It is noted that the 1×1-km MODIS radiances were averaged to the real SEVIRI resolution, rather than to a fixed 3×3- or 5×5-pixel grid. By doing so, a SEVIRI image of the investigated area was reproduced. The number of 1×1-km pixels to be aggregated within a SEVIRI pixel was 5–35, dependent on the MODIS viewing angle and the SEVIRI pixel size at the geolocation of observation. Using the MODIS land/sea mask, only pixels over ocean and land were selected for the ATL and EUR area, respectively. Additional

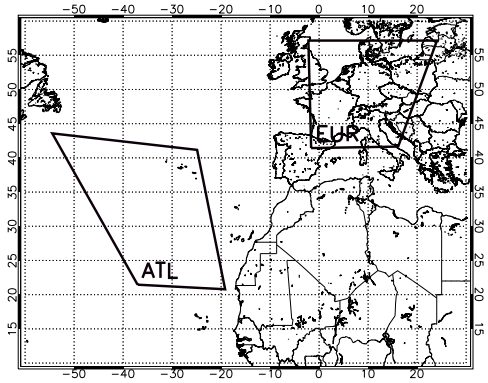


**Figure 4.4** *The two areas of investigation: Eastern Atlantic Ocean (ATL) and Central Europe (EUR).*

statistics on cloud fraction, the fraction of water and ice clouds, and variability in cloud optical thickness were also calculated for SEVIRI pixels having at least 10 MODIS pixels.

## 4.3 Results

### 4.3.1 Description of observed cloud-type occurrence over ATL and EUR

Table 4.1 shows the HRES and LRES distribution of water, ice, and mixed phase clouds for the classes cloud free, broken cloud, and overcast. The mixed-phase categorization represents HRES pixels with varying phases within the domain. All percentages are relative to the total number of observations for the ATL and EUR area, being about 269,000 and 154,000, respectively. About 20% of the clouds are broken clouds, which is consistent with the findings of Deneke et al. (2009). It follows from Table 4.1 that over the EUR area clouds contain considerably more ice than over the ATL area, especially for the fully overcast cases. This probably relates to deep convection, which dominates cloud formation over the European continent

**Table 4.1** *Water and ice cloud occurrence frequencies based on HRES and LRES retrievals for May and August 2007. Only clouds with $\tau_{HRES}>1.0$ were included in the dataset.*

| class | phase | ATL (%) | | EUR (%) | |
|---|---|---|---|---|---|
| | | HRES | LRES | HRES | LRES |
| cloud free | | 42.3 | 42.4 | 28.1 | 28.0 |
| broken clouds | water | 6.0 | 8.3 | 2.1 | 7.3 |
| | ice | 0.6 | 1.5 | 5.6 | 11.1 |
| | mixed | 3.2 | - | 10.7 | - |
| overcast | water | 29.1 | 29.5 | 14.0 | 16.6 |
| | ice | 15.2 | 18.3 | 33.0 | 37.0 |
| | mixed | 3.6 | - | 6.4 | - |

during the summer season.

Over the ATL area, cloud vertical extent is limited due to both less convection and subsidence within a quasi-persistent high-pressure area. Figure 4.5 shows contour plots of retrieved $\tau$ and $r_e$ for broken clouds over the EUR and ATL areas. Only pixels labeled as 'water' at HRES are included. The figure shows that for both the ATL and EUR area at LRES $\tau$ is lower than at HRES and that $r_e$ increases from HRES to LRES. The increase of $r_e$ with increasing $\tau$ is conform findings of Szczodrak et al. (2001).

Because the low-resolution $r_e$ retrieval could be influenced by variability in both the high-resolution $\tau$ and $r_e$, we have performed calculations on the variability in $\tau$ and $r_e$ within the LRES pixels over both the ATL and EUR area. These two quantities are shown in Figure 4.6. For consistency reasons, both the $\tau$ and $r_e$ variability have been calculated using the $NIQR$ as defined by Equation 4.1. From Figure 4.6 it is obvious that the variability in $\tau$ largely exceeds the variability of $r_e$. The median $NIQR$ values are 0.451 and 0.147 for $\tau$ and $r_e$, respectively.

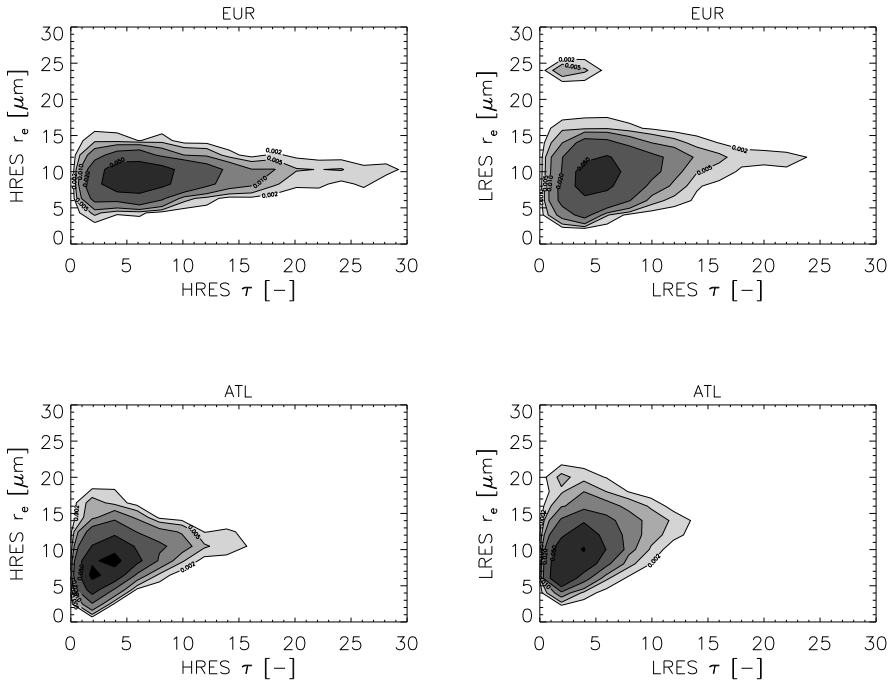


**Figure 4.5** *Contour plots of (left) HRES-retrieved and (right) LRES-retrieved $\tau$ vs $r_e$ for broken water clouds over the (top) EUR and (bottom) ATL areas for May and August 2007.*

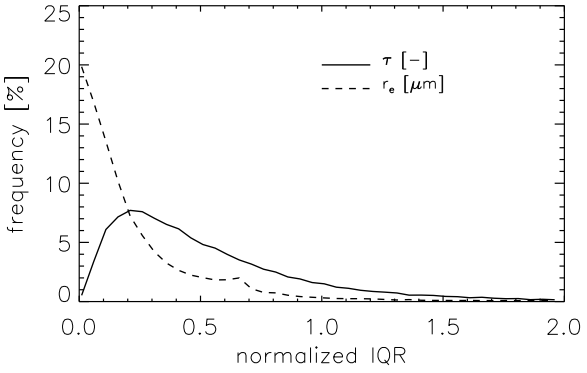


**Figure 4.6** *Frequency distribution of the variability in (solid line) $\tau$ and (dashed line) $r_e$, both expressed as normalized interquartile range (see Equation (4.1) for its definition). Data were selected over both areas for May and August 2007; within each LRES pixel the interquartile range and median $r_e$ and $\tau$ of the HRES retrievals were computed.*

### 4.3.2 Simulations with synthetic data

#### Broken clouds

Figure 4.7 shows the simulated $\tau_{\mathrm{LRES}}$, $r_{\mathrm{e,LRES}}$, and $T_{\mathrm{c,LRES}}$ for water clouds over an underlying dark and bright surface. The error bars in panels c) and d) denote the variability in retrieved $r_e$ resulting from a +/- 0.03 change in 1.6-$\mu$m surface albedo. $\tau_{\mathrm{LRES}}$ increases nearly linearly with cloud fraction for both the thin and thick clouds (Figures 4.7a and 4.7b), independent of the underlying surface. For thin clouds (Figure 4.7c), $r_{\mathrm{e,LRES}}$ is larger than $r_{\mathrm{e,HRES}}$ for all cloud fractions. Further, $r_{\mathrm{e,LRES}}$ is larger over a (dark) ocean than over a (brighter) land surface. Because effective radius increases with decreasing 1.6-$\mu$m reflectance, the resulting increase in $r_{\mathrm{e,LRES}}$ is larger over a dark than over a bright surface.

Figure 4.7d shows that also for thick clouds ($\tau_{\mathrm{HRES}}$=20, $r_{\mathrm{e,HRES}}$=12 $\mu$m), $r_{\mathrm{e,LRES}}$ is larger than $r_{\mathrm{e,HRES}}$, with the largest overestimation again occurring over the ocean surface. $r_{\mathrm{e,LRES}}$ approaches 24 $\mu$m, the maximum value for water clouds in the LUT, over the dark surface for cloud fraction $\leq$ 0.4. In this case, the inversion of 0.6-$\mu$m and 1.6-$\mu$m reflectances in the CPP algorithm results in the retrieval of an ice particle effective radius and in principle the assignment of cloud phase 'ice'. The cloud-top temperature as function of cloud fraction is shown in Figure 4.7e and 4.7f. It can be seen that $T_{\mathrm{c,LRES}}$ quickly converges to the real cloud-top temperature (270 K) as a result of the cloud emissivity correction.

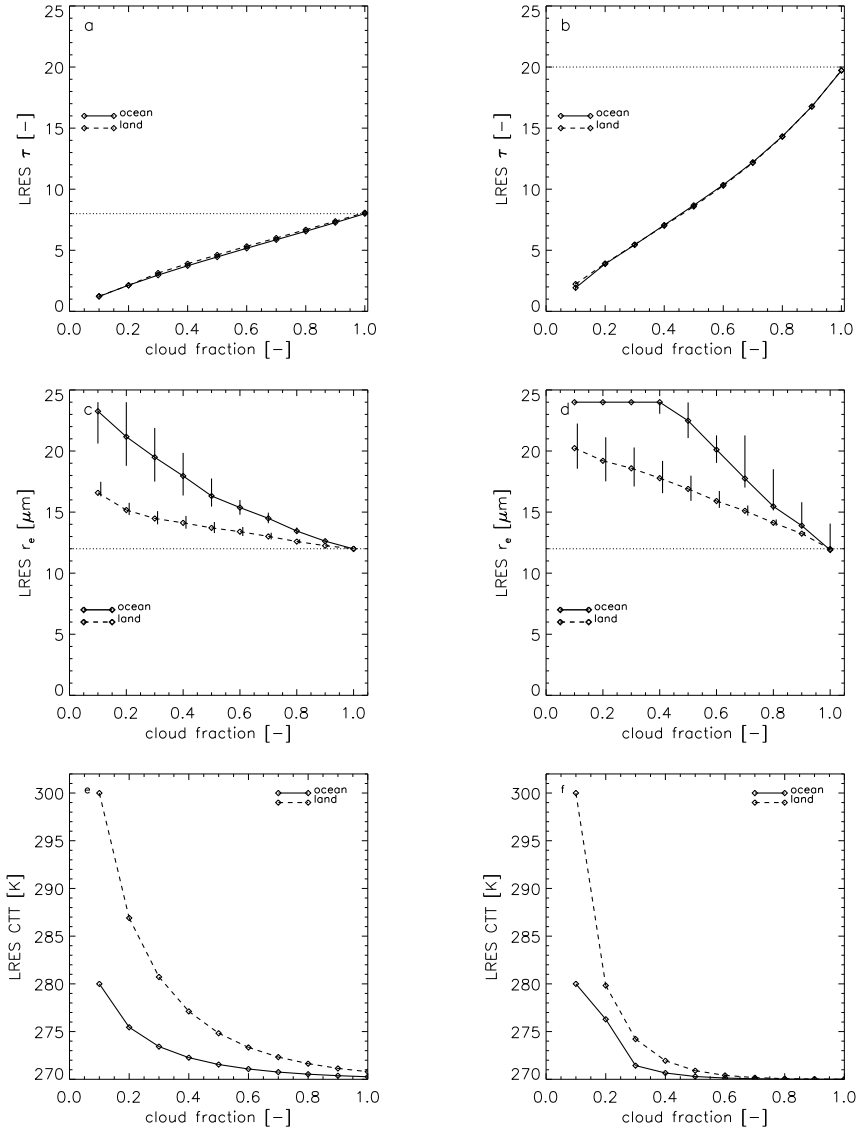


**Figure 4.7** *Simulation results for broken clouds: (a,b) Simulated $\tau_{LRES}$, (c,d) $r_{e,LRES}$, (e,f) and $T_{c,LRES}$ as function of cloud fraction for a thin water cloud with $\tau$=8, $r_e$=12 μm (a, c, e) and a thick water cloud with $\tau$=20, $r_e$=12 μm (b, d, f). Calculations were performed for a dark (ocean, $\alpha_{0.6}=\alpha_{1.6}$=0.05, solid line) and bright (mid-latitude land, $\alpha_{0.6}$=0.10, $\alpha_{1.6}$=0.20, dashed line) surface. Vertical bars denote the spread in retrieved $\tau$ and $r_e$ when assuming an error in the 0.6 μm (for $\tau$) or 1.6 μm (for $r_e$) surface albedo of +/- 0.03. The dotted lines indicate $\tau_{HRES}$ (a and b) and $r_{e,HRES}$ (c and d). Solar ($\theta_o$) and viewing ($\theta$) zenith angles are 10°, the azimuth difference angle ($\varphi$-$\varphi_o$) is 100°. $T_{c,LRES}$ was calculated assuming a real cloud-top temperature of 270 K and surface temperatures of 280 K and 300 K for the ocean and mid-latitude land surface, respectively.*

From Figure 4.7f it also follows that $\varepsilon_{\text{c,LRES}}$ approaches unity at lower cloud fractions in case of optically thick clouds at high resolution, hence the real cloud-top temperature is more rapidly converging. It is recalled that due to the underestimation of $\tau_{\text{LRES}}$, $\varepsilon_{\text{c,LRES}}$ is also underestimated, hence $T_{\text{c,LRES}}$ is overestimated. Because broken cloudiness mostly occurs for cumulus (water) clouds, the overestimation in $T_c$ due to an underestimation of $\varepsilon_c$ provides a partly compensating factor for the overestimation due to broken clouds in $r_e$.

*Inhomogeneous overcast clouds*

Figure 4.8 presents the simulated difference ($\Delta r_e$) between $r_{\text{e,HRES}}$ and $r_{\text{e,LRES}}$ for overcast inhomogeneous clouds with $\tau_{med}$=8 and $\tau_{med}$=15. Because $r_{\text{e,HRES}}$ was fixed at 12 $\mu$m and 16 $\mu$m in Figures 4.8a and 4.8b, respectively, the variation in $r_{\text{e,LRES}}$ is solely caused by a variation in $\tau_i$.
$r_{\text{e,LRES}}$ becomes larger than $r_{\text{e,HRES}}$ with increasing inhomogeneity for both cloud types, with the largest differences occurring over a dark surface, due to the larger contrast between cloud and surface compared to a bright surface. For larger $r_{\text{e,HRES}}$ (Figure 4.8b) the effect of inhomogeneous clouds on $r_{\text{e,LRES}}$ is larger, which is related to the steeper curvature of the $r_e$ vs $\tau$ function for larger cloud particles. As a result, linearly averaging of reflectances leads to a larger deviation from $r_{\text{e,HRES}}$ (see Figure 4.3).

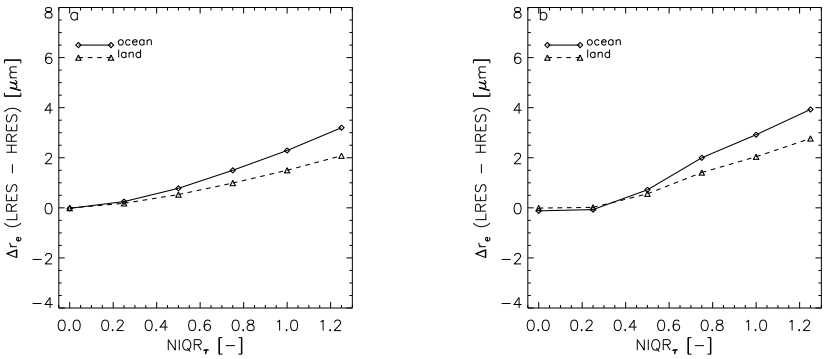


**Figure 4.8** *Difference between simulated $r_{e,LRES}$ and $r_{e,HRES}$ ($\Delta r_e$) for overcast water clouds as function of cloud inhomogeneity, expressed as Normalized Interquartile Range of $\tau$ ($NIQR_\tau$, see text for its definition). Results are shown for a (solid line) dark and (dashed line) bright surface at 1.6 $\mu$m for (a) thin clouds with HRES $\tau_{med}$=8, $r_e$ =12 $\mu$m and (b) thick clouds with $\tau_{med}$=15, $r_e$ =16 $\mu$m.*

Figure 4.9 shows $\Delta r_e$ as function of $\tau_{med}$ at $NIQR_\tau$=1.25 for overcast water clouds over an ocean surface having large ($r_e$=16 $\mu$m) and small ($r_e$=12 $\mu$m) droplets. The effect of the steeper curvature at $r_e$=16 $\mu$m can clearly be seen. At low $\tau_{med}$, the difference between thick and thin water clouds becomes larger. This is because of a larger sensitivity to a change in 1.6-$\mu$m reflectance for larger $r_e$ values. For example, at $\tau$=4 the sensitivity to a 1% change in 1.6-$\mu$m reflectance is about 1.5 $\mu$m larger within the range 16–24 $\mu$m than within the range

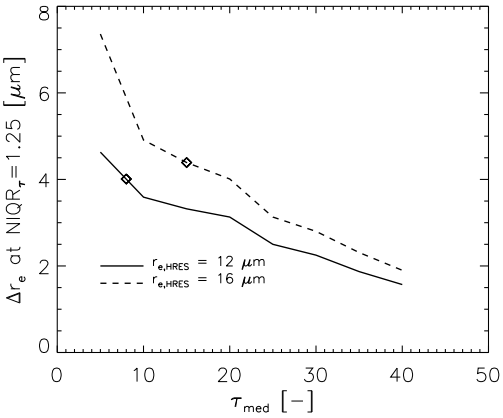


**Figure 4.9** *Simulated $\Delta r_e$ at $NIQR_\tau$=1.25 over a dark surface ($\alpha_{0.6}$=$\alpha_{1.6}$=0.05) as function of $\tau_{med}$ for overcast water clouds having small ($r_e$=12 µm, solid line) and large ($r_e$=16 µm, dashed line) droplets. The values at $NIQR_\tau$=1.25 over a dark surface shown in Figure 4.8a and 4.8b are denoted by the diamond symbols.*

12–16 $\mu$m. The simulations for inhomogeneous overcast clouds show that at larger degrees of inhomogeneity and for clouds with large droplet sizes (generally present in thicker clouds) the $r_{\text{e,LRES}}$ is considerably overestimated, which may lead to erroneous $\text{CPH}_{\text{LRES}}$ retrievals.

### 4.3.3 MODIS observations

The evaluation of simulated CPP retrievals in the previous section demonstrated that for broken clouds the largest effect on the low-resolution $r_e$ and CPH retrieval occurs for thick clouds, whereas for inhomogeneous overcast clouds the low-resolution $r_e$ and CPH retrievals are most affected for thin clouds having large particles. Both the broken and inhomogeneous cloud effects are most prominent over dark surfaces, although the $T_c$ check may have a compensating contribution. To quantify the effects of broken and inhomogeneous clouds in true observations, the CPP algorithm is used to compare HRES and LRES retrievals from MODIS radiances. First, the effect of broken and inhomogeneous clouds on the retrieval of $r_e$ is quantified for the ocean (ATL) and mid-latitude land (EUR) area. Second, the effect on the retrieval of cloud phase is assessed.

#### Broken clouds

It follows from Table 4.1 that about 20% of the clouds are broken. In order to exemplify where differences between HRES- and LRES-retrieved $r_e$ occur, Figure 4.10 shows the HRES- and LRES-obtained $r_e$ for an area southeast of the Azorean archipelago. This area is frequently covered with stratocumulus fields within a quasi-persistent high-pressure area. It is obvious

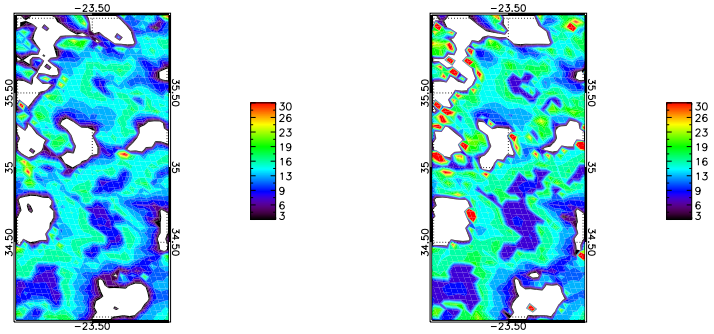


**Figure 4.10** *(left) HRES-retrieved and (right) LRES-retrieved $r_e$ ($\mu$m) over a $1^\circ \times 2^\circ$-area southeast of the Azores. Clouds with $r_e < 3\,\mu$m are not shown. Contouring is done for each 3-$\mu$m interval.*

from the figure that the largest overestimations at LRES occur at the stratocumulus edges.

Figure 4.11 presents the mean $r_{\mathrm{e,HRES}}$ and $r_{\mathrm{e,LRES}}$ versus cloud fraction for the EUR and ATL area for water clouds. Cloud-free pixels and pixels with $\tau_{\mathrm{HRES}}$<1 were discarded to ensure that only clouds were investigated, rather than also thick aerosol layers. Over the EUR area, the largest difference between $r_{\mathrm{e,LRES}}$ and $r_{\mathrm{e,HRES}}$ occur at the lowest cloud fractions (+4 $\mu$m at cloud fractions 0.02–0.2), which is conform the simulations shown in Figure 4.7. However, differences are smaller than in the synthetic data. The use of a fixed $r_e$ and viewing geometry in the simulations is probably responsible for this. The difference $r_{\mathrm{e,LRES}}-r_{\mathrm{e,HRES}}$ gradually decreases towards +0.5 $\mu$m at cloud fraction 1.0.

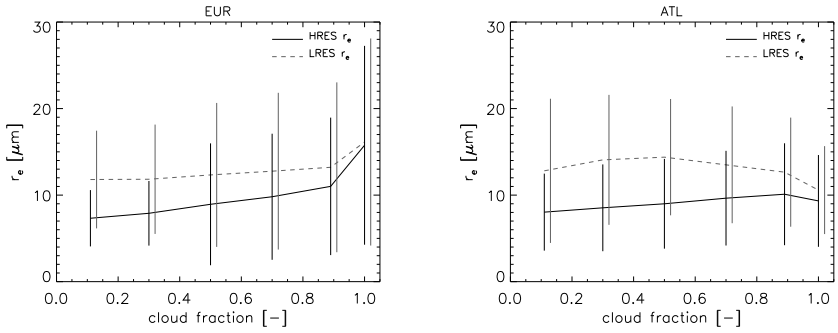


**Figure 4.11** *Mean retrieved $r_{e,HRES}$ (black line) and $r_{e,LRES}$ (dashed gray line) for water clouds (at both HRES and LRES) retrieved from MODIS radiances as function of cloud fraction for the EUR (left panel) and ATL (right panel) areas. The vertical bars indicate +/- one standard deviation within the respective cloud fraction bins (centered at 0.1, 0.3, 0.5, 0.7, 0.9, and for cloud fraction=1.0). For clarity of presentation, the vertical bars of $r_{e,LRES}$ are slightly shifted to the right. Only clouds with $\tau_{HRES}$>1 were included.*

Similar to the EUR area, over the ATL area the largest differences $r_{e,LRES}$-$r_{e,HRES}$ are found at low cloud fractions. The difference between $r_{e,LRES}$ and $r_{e,HRES}$ for broken clouds is of the same order (5 $\mu$m at the lowest cloud fraction bin) as found by Coakley et al. (2005), despite that in their study spectral channels less sensitive to the underlying surface, and hence a smaller penetration depth inside the cloud (Rosenfeld et al. 2004), were used for retrieving $r_e$.

The HRES- and LRES-retrieved water cloud occurrence frequency for clouds with $\tau_{HRES}$>1 (hereafter referenced as $CPH_{HRES}$ and $CPH_{LRES}$, respectively) versus cloud fraction is shown in Figure 4.12 for the EUR and ATL areas. Over the EUR area, $CPH_{LRES}$–$CPH_{HRES}$ is about +10% at low cloud fractions, but decreases and changes sign to -2% at cloud fraction > 0.9. Integrated over all cloud fractions the difference $CPH_{LRES}$–$CPH_{HRES}$ is -0.6%.

Without $T_c$ check the difference $CPH_{LRES}$–$CPH_{HRES}$ would be -2.2%, which demonstrates the added value of this check to the cloud-phase retrieval. Over the ATL area, the difference $CPH_{LRES}$–$CPH_{HRES}$ is small over all cloud fractions, ranging from +1% at cloud fraction 0.1 towards -3% for fully overcast clouds. Integrated over all cloud fractions, the difference $CPH_{LRES}$–$CPH_{HRES}$ is -2.3%. If no $T_c$ check would be included in the cloud-phase retrieval algorithm, the integrated difference would be -3.5%.

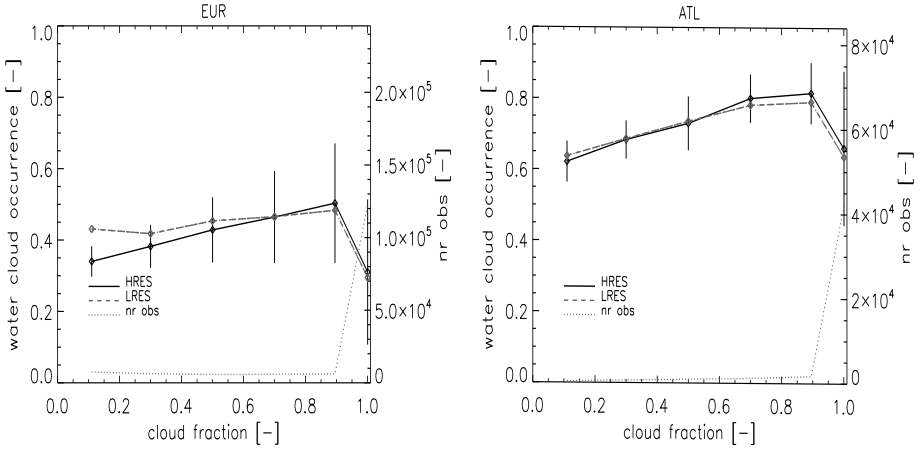


**Figure 4.12** *HRES-retrieved (solid line) and LRES-retrieved (dashed gray line) CPH expressed as water cloud occurrence frequency versus cloud fraction for clouds with $\tau_{HRES}$>1 over the (left) EUR and (right) ATL areas. Vertical bars denote the standard deviations of the HRES obtained water cloud occurrence frequency. The number of observations for each cloud fraction bin is indicated by the dotted gray line, with scaling on the right-hand axis. The CPH was retrieved using both the 0.6- and 1.6-$\mu$m reflectances and the $T_c$ correction (see section 4.2.2 for more details).*

*Inhomogeneous overcast clouds*

For the entire dataset of both areas, within each SEVIRI pixel the 25th, 50th, and 75th percentile of $\tau_i$ were calculated, from which the $NIQR_\tau$ within the respective LRES pixel was obtained. Subsequently, SEVIRI pixels were collected within $NIQR_\tau$ bins of 0.0–0.05 (representing virtually homogeneous clouds), 0.05–0.5, 0.5–1.0, and 1.0–1.5. For each bin the mean and standard deviation of $\Delta r_e$ were computed.

Figure 4.13 presents the observed mean difference between $r_{\mathrm{e,LRES}}$ and $r_{\mathrm{e,HRES}}$ ($\Delta r_e$) for HRES-retrieved water clouds with $\tau_{\mathrm{HRES}}$>1. For reference, also the differences found in the synthetic dataset with fixed values of $r_e$=12 $\mu$m and $\tau_{med}$=8 (Figure 4.8a) are shown. Figure 4.13 demonstrates that for both the EUR and ATL area the observed $\Delta r_e$ follows a similar trend with increasing cloud inhomogeneity as the $\Delta r_e$ from the synthetic data, although the retrieved values are substantially lower than the synthetic values. Differences between synthetic and observed $\Delta r_e$ can be attributed to differences between the $\tau$ distributions; in the synthetic datasets a lognormal distribution was used, whereas the $\tau$ distributions in the retrievals may deviate from this. Also, the assumed fixed value of $r_{e,i}$ and viewing geometry in the synthetic datasets contrasts with the MODIS observations.

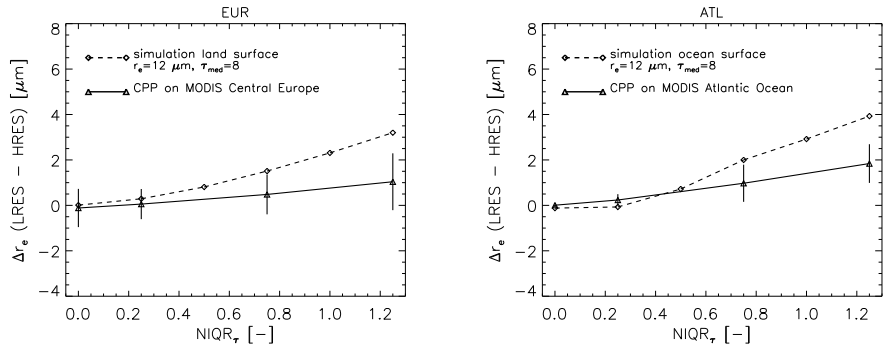


**Figure 4.13** *Comparison between MODIS-observed (solid line) and simulated (dashed line) $\Delta r_e$ for overcast inhomogeneous HRES-retrieved water clouds with $\tau_{HRES}$>1 as function of $NIQR_\tau$ for (left) EUR and (right) ATL. The triangle symbols for the observed values are plotted at the $NIQR_\tau$ bin center, vertical bars denote the observed standard deviation of $\Delta r_e$ within each bin.*

$\mathrm{CPH_{HRES}}$ and $\mathrm{CPH_{LRES}}$ are plotted versus cloud inhomogeneity for EUR and ATL in Figure 4.14. Over the EUR area, $\mathrm{CPH_{LRES}}$ and $\mathrm{CPH_{HRES}}$ gradually diverge with increasing inhomogeneity reaching a difference of 10% more 'ice' than 'water' retrieved at LRES than at HRES for $NIQR_\tau$=1.25. Integrated over all inhomogeneity bins, the difference $\mathrm{CPH_{LRES}}$–$\mathrm{CPH_{HRES}}$ is -1.3%. Over the ATL area, $\mathrm{CPH_{LRES}}$<$\mathrm{CPH_{HRES}}$ within the entire range of inhomogeneities, which is most likely linked to the increase in $r_{\mathrm{e,LRES}}$ with increasing cloud inhomogeneity, as seen from both the simulations and observations (see Figures 4.8 and 4.13). The difference

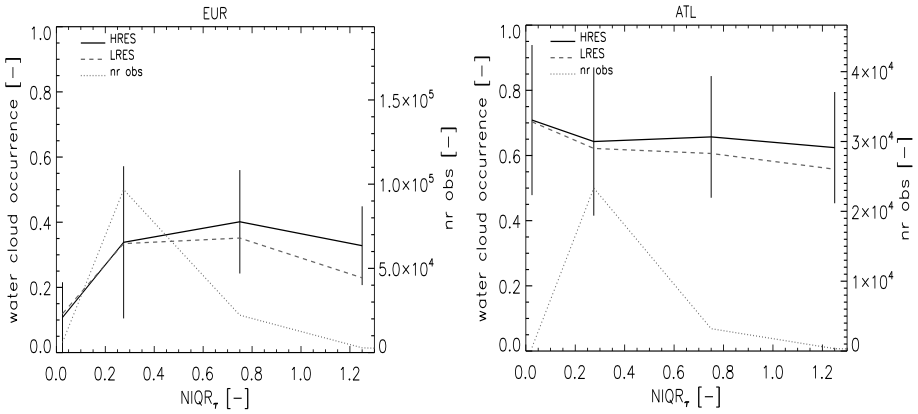


**Figure 4.14** *Water cloud occurrence frequency as function of cloud inhomogeneity ($NIQR_\tau$) obtained from HRES (solid line) and LRES (dashed line) retrievals for overcast clouds with $\tau_{HRES}$>1. The dotted gray line indicates the number of observations per $NIQR_\tau$ bin, with scaling on the right-hand axis. The CPH was retrieved using both the 0.6- and 1.6-$\mu$m reflectances and the $T_c$ correction (see section 4.2.2 for more details).*

$CPH_{LRES}$–$CPH_{HRES}$ reaches a value of -6% at $NIQR_\tau$=0.75 and $NIQR_\tau$=1.25, resulting in an integrated difference of -2.5%.

## 4.4 Discussion and conclusions

In this paper we investigated the influence of broken cloudiness and cloud inhomogeneity on satellite-retrieved $r_e$ and cloud phase of the CPP retrieval algorithm, and quantified the difference between low- (geostationary satellite) and high- (polar satellite) resolution derived values. We have identified an overestimate of cloud particle absorption caused by the non-linear relation of reflectances at absorbing and non-absorbing wavelengths as underlying physical mechanism. For the sake of simplicity, the inhomogeneity effect was only investigated for overcast cloud cases. Using synthetic datasets, it was shown that for thick broken clouds at high resolution (1×1 km$^2$ nominal) the low-resolution (3×3 km$^2$ nominal) CPH retrieval can become erroneous due to a too high retrieved $r_e$ (by up to 12 $\mu$m). This effect is strongest over dark surfaces (ocean), as the high-resolution cloud-free reflectances significantly contribute to the low-resolution 0.6- and 1.6-$\mu$m reflectance. For inhomogeneous overcast clouds, $r_{e,LRES}$ can be overestimated by 3–4 $\mu$m for both clouds with $r_{e,HRES}$=12 $\mu$m and clouds with $r_{e,HRES}$=16 $\mu$m, depending on the degree of inhomogeneity and underlying surface. The overestimation of $r_{e,LRES}$ is larger than the findings of Zinner and Mayer (2006), who found about 5% overestimation in low-resolution $r_e$ for inhomogeneous overcast clouds. However, their analysis included both inhomogeneity and 3D effects, while the latter was not accounted for in our 1D simulations.

Retrievals for broken cloud fields from MODIS radiances for May and August 2007 reveal that over both the ATL and EUR area $r_{e,LRES}$ is up to 5 $\mu$m larger than $r_{e,HRES}$. The overestimation

of $r_{e,LRES}$ is conform the simulations for broken cloud $r_{e,LRES}$, although the magnitude of the observed difference is smaller than the simulated difference, due to the use of a fixed $r_{e,HRES}$ and viewing geometry in the simulations. For cloud phase, at cloud fractions smaller than 0.5 the difference $CPH_{LRES}$–$CPH_{HRES}$ is up to +10% over the EUR area, while this difference becomes -2% at larger cloud fractions. Integrated over all cloud fractions, 0.6% less water clouds are retrieved at LRES than at HRES. If no $T_c$ check is applied, 2.2% less water clouds would be retrieved at LRES. Over the ATL area, $CPH_{LRES}$–$CPH_{HRES}$ gradually decreases from +1% to -3% with increasing cloud fraction. Due to the number of observations being strongly skewed towards overcast clouds, the overall difference is -2.3%. If no $T_c$ check is applied, this difference would be -3.5%.

For inhomogeneous overcast clouds, the difference $r_{e,LRES}$–$r_{e,HRES}$($\Delta r_e$) gradually increases with increasing inhomogeneity, but more pronounced in the synthetic data than from the MODIS retrievals. Maximum observed $\Delta r_e$ values are +1 $\mu$m and +2 $\mu$m over the EUR and ATL area, respectively. It is argued that the difference between synthetic data and retrievals is caused by differences in the $\tau$ distributions and the variability in $r_{e,i}$ and viewing geometries in the retrievals. The difference $CPH_{LRES}$–$CPH_{HRES}$ integrated over all inhomogeneity classes is -1.3% and -2.5% over the EUR and ATL area, respectively.

The broken cloudiness problem is not constrained to using visible/near-infrared data only; other $r_e$ and cloud-phase retrieval methods likely will have different values at low and high resolution. However, the sensitivity to surface albedo or surface emissivity (in case of a thermal infrared retrieval method) will depend on the spectral channels used. For example, use of the 2.2 $\mu$m or 3.9 $\mu$m channel for retrieving $r_e$ will be less sensitive to the underlying surface than the 1.6-$\mu$m channel used here, because cloud particles absorb radiation more efficiently at the former wavelengths and thus decrease the amount of radiation penetrating through a cloud. For example, the stronger absorption of the AVHRR 3.7-$\mu$m channel compared to the 1.6-$\mu$m channel enabled Platnick et al. (2001) to improve $r_e$ retrievals over snow-covered areas in the Arctic region.

The upcoming generation of geostationary satellite imagers will carry one or more high spatial resolution channels in addition to the suite of spectral channels that observe at the operational resolution. These high-resolution channels may allow for correcting the low-resolution $r_e$ and CPH climatologies (as well as other cloud physical properties) by using the fractional coverage and/or horizontal inhomogeneity of cloud fields obtained at high resolution. For the SEVIRI instrument, attempts are ongoing to retrieve high-resolution ($1\times1$ km$^2$ at nadir) $\tau$ from the High-Resolution Visible (HRV) channel, which spans the wavelength range of ~0.4–1.1 $\mu$m (Deneke and Roebeling 2010). Despite this channel having different spectral characteristics than the low-resolution 0.6-$\mu$m channel, an estimate of the high-resolution $\tau$ is made by using the correlation between HRV reflectance averaged over a low-resolution pixel and the corresponding low-resolution 0.6-$\mu$m reflectance. Further, an estimate of cloud fraction using a simple HRV reflectance threshold can be obtained to correct the low-resolution 0.6- and 1.6-$\mu$m reflectance for cloud fraction before the low-resolution CPP retrieval is performed. In order to develop a robust correction method, differences between the HRV reflectance and 0.6-$\mu$m reflectance need to be investigated over various areas and for various cloud types.

For cloud inhomogeneity, alternatives to the $NIQR$ diagnostic used to obtain cloud variability information exist in, for example, the variance in measured visible radiances or the variance in $T_c$. It is expected that different cloud inhomogeneity indicators likely give slightly different results than presented here. However, the general pattern seen for $r_{\mathrm{e,LRES}}$ and $\mathrm{CPH}_{\mathrm{LRES}}$ with increasing cloud inhomogeneity will dominate. The above results, including our ongoing research on the correlation between high- and low-resolution reflectance, will be an important improvement to the low-resolution derived cloud physical property climatologies. Future work will focus on the implementation of bias correction factors to the cloud property climatologies derived at geostationary resolution.

# Chapter 5

## SEVIRI precipitation retrieval evaluation over West Africa using TRMM-PR and CMORPH

This Chapter presents the evaluation of the CPP-PP algorithm over West Africa. The algorithm combines CWP, cloud phase, $r_e$, and $T_c$ retrievals from visible, near-infrared, and thermal infrared observations of SEVIRI to estimate precipitation occurrence frequency and precipitation intensity. It is investigated whether the CPP-PP algorithm is capable of retrieving these precipitation properties over West Africa with sufficient accuracy, using TRMM-PR observations as reference. Further, it is assessed whether CPP-PP is capable of monitoring the seasonal and daytime evolution of precipitation during the monsoon, using Climate Prediction Center Morphing Technique (CMORPH) precipitation observations. The SEVIRI-detected precipitation area agrees well with TRMM-PR, with the areal extent of precipitation by CPP-PP being ~10% larger than from TRMM-PR. The mean retrieved precipitation intensity from CPP-PP is about 8% higher than from TRMM-PR. Examination of the TRMM-PR and CPP-PP cumulative frequency distributions revealed that differences between CPP-PP and TRMM-PR are generally within +/-10%. Relative to rain gauge observations, CPP-PP shows very good agreement up to 5 mm $h^{-1}$. However, at higher precipitation intensities (5–16 mm $h^{-1}$) CPP-PP overestimates compared to the rain gauges. Further, it was shown that both the accumulated precipitation and the seasonal progression of precipitation throughout the monsoon is in good agreement with CMORPH, although CPP-PP retrieves higher amounts in the coastal region. Using latitudinal Hovmöller diagrams, a fair correspondence between CPP-PP and CMORPH was found, which is reflected by high correlation coefficients (≈0.7) for both precipitation intensity and precipitation occurrence frequency. The daytime diurnal cycle of precipitation from CPP-PP shows different patterns for three regions in West Africa throughout the monsoon, with a decrease in dynamical range of precipitation near the major monsoon rains. The dynamical range as retrieved from CPP-PP is larger than that from CMORPH. This might result from both the better spatio-temporal resolution of SEVIRI, as well as from thermal infrared radiances being partly used by CMORPH, which smooth the daytime precipitation signal. The promising results show that the CPP-PP algorithm, taking advantage of the high spatio-temporal resolution of SEVIRI, is of added value for monitoring daytime precipitation patterns in tropical areas.

Based on: Wolters, E.L.A., B.J.J.M. van den Hurk, and R.A. Roebeling, 2011: Evaluation of precipitation retrievals from SEVIRI reflectances over West Africa using TRMM-PR and CMORPH, *Hydrol. Earth Syst. Sci.*, **15**, 437–451, doi:10.5194/hess-15-437-2011.

## 5.1 Introduction

Precipitation can be considered the most crucial link between the atmosphere and the surface in weather and climate processes. Quantitative precipitation estimates at high spatial and temporal resolution are of increasing importance for water resource management, for improving the precipitation prediction scores in numerical weather prediction (NWP) models, and for monitoring seasonal to interannual climate variability. A dense and high-temporal resolution ground-based measurement network is required to achieve accurate precipitation observations. However, in several regions, especially over some tropical land areas and over the oceans, the coverage by rain gauges and/or ground-based radars is insufficient. For example, over certain regions in West Africa only a few rain gauges per 1000 $km^2$ are available (Ali et al. 2005). In addition, most operational rain gauges are recorded at daily time scales or larger. Satellite instruments, especially those onboard geostationary satellites, have the potential to provide additional insights in the spatio-temporal precipitation characteristics at sub-daily time scales. These insights are particularly useful for those regions where rain gauges are sparse.

Local economy, hydrology, and ecology in West Africa heavily depend on the availability of the monsoon rains. Especially in a region northward of ~15° N, less monsoon rain during subsequent years may intensify desertification, although no significant trend has been found throughout the 1980s and 90s (Nicholson et al. 1998). Less precipitation during the monsoon season also results in an increased surface albedo (because of decreased soil moisture content), increased dust generation, and less agricultural yield. Therefore continuous precipitation monitoring is of great importance.

The West-African monsoon (WAM) is the northward movement of the Inter Tropical Convergence Zone (ITCZ) during boreal summer and is manifested by the convergence of moist southwesterly air from the Atlantic Ocean with dry northeasterly air from the Sahara. The start of the monsoon season is often determined by a change in sign of the zonal wind component ($u$), i.e., a change from easterly to westerly winds. With the start of the monsoon season, first some sporadic convective activity due to the advection of moist oceanic air is triggered. This usually occurs from mid-April to mid-May and is followed by a relatively dry spell of about one month. Subsequently, the full onset of the WAM sets in around the end of June. Sultan and Janicot (2003) found that this onset date is 24 June ±8 days for the period 1968–1990. After this onset, a band with westward moving mesoscale convective systems (MCSs) traverses northward over the West African continent. These MCSs partly originate in the vicinity of African Easterly Wave (AEW) troughs. AEWs are dynamical disturbances within the African Easterly Jet (AEJ), which in turn exists due to the temperature gradient between the Gulf of Guinea and the Sahara (Cook 1999). Fink and Reiner (2003) found that about 40% of MCSs over West Africa are forced through AEWs, with the percentage increasing from east to west. Further, mature large convective systems influence the AEJ through generation of a rear-to-front flow in the lower part of the system and by accelerating the AEJ behind the system (Diongue et al. 2002).

The initiation of MCSs is not only dynamically driven, but is also dependent on e.g. soil wetness, with convection being suppressed over soils that are too wet (Taylor and Ellis 2006; Taylor et al. 2007).

Often a sudden shift from ~5° N to ~10° N of the most heavy rains is seen after the onset date. Several mechanisms explaining this monsoon jump have been proposed. For example, Sultan and Janicot (2003) suggested that due to persistent heating of the land surface near 15° N a thermal low develops, which is gradually strengthened by upper-air divergence caused by the Tropical Easterly Jet (TEJ). Hagos and Cook (2007) extended this view by showing through model simulations that a shallow southerly flow pattern from the Gulf of Guinea during the premonsoon phase is very important for the moisture supply into the continent. Ramel et al. (2006) debated the mechanism proposed by Sultan and Janicot (2003), as they posed that in the region near 15° N no sufficient low-level moisture is available to initiate large-scale wet convection. With the passage of the heavy monsoon rains, maximum convective activity occurs late in the afternoon, possibly as a result of gravity waves from morning convection over the West African ocean propagating northward (Sultan et al. 2007). However, Basu (2007) noted a shift of the main convective activity during the monsoon towards the late night/early morning, especially when dynamical factors and/or orography are involved.

The retrieval of precipitation intensity and precipitation amount from passive satellite imagery is closely related to the detection of convective cloud cells. Until now, many convection detection retrieval techniques have been developed (see e.g., Mecikalsi and Bedka 2006; Zinner et al. 2008). Most precipitation schemes from passive visible (VIS) and infrared (IR) imagery are based on the assumption that clouds start to precipitate if the thermal infrared brightness temperature (BT) becomes lower than a certain threshold value. The rationale behind this is that precipitation is more likely to occur if ice crystals are abundant in the cloud top (Pruppacher and Klett 1997) and is generally referred to as Cold Cloud Duration technique (CCD). However, the relation between BT and precipitation intensity is indirect, as e.g. thick cirrus clouds have low temperatures, but generally do not produce any (surface-observed) rain. The overestimation due to attributing precipitation intensities to non-precipitating cirrus is partly compensated for by an underestimation of precipitation intensities from shallow convection.

Despite these drawbacks, various precipitation retrieval techniques have been based on thermal infrared (TIR) temperatures only (mostly using the 10–12 $\mu$m atmospheric window spectrum), assuming that the amount of non-precipitating cirrus clouds is only minor (Adler and Negri 1988; Arkin and Meisner 1987; Ba and Gruber 2001; Negri and Adler 1993; Negri et al. 1984). An advantage of TIR data is the availability during both day and night. Although the performance of TIR-based precipitation retrieval algorithms is quite poor in estimating instantaneous precipitation intensities, a good correlation between cloud-top temperature and precipitation is found when accumulated over large areas and sufficiently long time periods (Kidd 2001), although Arkin and Xie (1994) pointed out that for stratiform rain TIR-based precipitation retrievals are less accurate. Most CCD techniques are calibrated locally or regionally with rain gauge and/or passive microwave (PMW) data to obtain an optimum accuracy. See for example Huffman et al. (2001) for a detailed description of the Global Precipitation Climatology Project One-Degree Daily (GPCP-1DD) product.

More direct ways to estimate precipitation intensity are performed by using passive microwave (PMW) data and infrared radiances. During the last decade, the development of precipitation retrieval algorithms has more focused on incorporating multiple sensors. For example, the TRMM Multi-Satellite Precipitation Algorithm [TMPA, Huffman et al. (2007)] combines data from PMW imaging, sounding instruments, and geostationary-observed IR radiances to obtain a single precipitation product. In the Climate Prediction Center Morphing Techinque [CMORPH, Joyce et al. (2004)], IR radiances are used to advect/morph cloud systems between two consecutive PMW instrument overpasses to obtain intermediate precipitation intensity estimates. A complete overview of the present-day status of the various precipitation retrieval algorithms can be found in Kidd and Levizzani (2011).

This Chapter presents an approach to estimate precipitation intensity using retrieved cloud-top properties from visible and near-infrared reflectances observed by the Spinning Enhanced Visible and Infrared Imager (SEVIRI) onboard the Meteosat Second Generation (MSG) satellites. The KNMI Cloud Physical Properties – Precipitation Properties algorithm (CPP-PP) differs from most state-of-the-art satellite precipitation retrieval algorithms in that it is independent of satellite data merging and calibration to rain gauge observations.

First, this research assesses whether CPP-PP is suitable to accurately estimate precipitation over West Africa in terms of mean precipitation area and median precipitation intensity. Earlier work already showed good performance of CPP-PP precipitation retrievals over the Netherlands in comparison with ground-based radar. The areal extent of precipitation as detected by CPP-PP from SEVIRI data correlates well (corr$\sim$0.9), with the retrieved precipitation intensities having an accuracy (defined as the difference in median precipitation intensity between SEVIRI and rain radar) of about 10% (Roebeling and Holleman 2009). In this paper, precipitation retrievals from the Tropical Rainfall Measurement Mission Precipitation Radar (TRMM-PR) and the CMORPH product are used as reference datasets. The CMORPH product is chosen because it is generally considered being of high quality [see e.g. Ebert et al. (2007)]. Although its quality is limited for convective precipitation over continental areas [Sapiano and Arkin (2009), Jobard et al. (2010), Tian et al. (2010)], the usage of almost entirely different satellite instrument data (PMW and TIR) than CPP-PP makes it a suitable alternative dataset for evaluating CPP-PP. Other factors that justify using CMORPH data are the 3-hourly temporal resolution and its independency on rain gauge calibration, which enables a consistent evaluation of CPP-PP over both ocean and land surfaces. Second, the capability of CPP-PP to monitor the progression of the monsoon rains into the West African continent and the evolution of the daytime precipitation cycle throughout the monsoon season (May–September) for three regions over the West African continent is investigated for 2005 and 2006 and compared to results obtained with CMORPH.

This Chapter is organized as follows. Section 5.2 presents the methodology and various datasets used. Section 5.3 contains the results and discussion, after which conclusions are drawn in Section 5.4.

## 5.2 Data and methods

### 5.2.1 CPP-PP precipitation retrieval technique

SEVIRI, onboard the geostationary Meteosat-8 and Meteosat-9 satellites of the European Organization for the Exploitation of Meteorological Satellites (EUMETSAT), is a passive imager with 11 operational narrowband channels in the spectral range 0.6–13.4 $\mu$m. Three spectral channels cover the visible and near infrared, the remaining eight cover the thermal infrared spectral region. The sampling resolution is $3\times3\,\mathrm{km}^2$ at nadir. SEVIRI scans the Earth every 15 min from southeast to northwest.

The precipitation retrieval algorithm used here was introduced by Roebeling and Holleman (2009). It has been adapted from a method originally developed for use on the Special Sensor Microwave/Imager (SSM/I) by Wentz and Spencer (1998) to make it suitable for use on SEVIRI data. The original algorithm is only applicable to water clouds, because microwave radiation is only to a minor extent scattered by ice crystals. Therefore Roebeling and Holleman (2009) have extended the applicability to ice clouds by considering the Condensed Water Path (CWP). In other words, the CPP-PP algorithm is capable of retrieving precipitation intensity for both stratiform and convective precipitation. It estimates precipitation intensity using condensed water path (CWP), cloud particle effective radius ($r_e$), cloud geometric height ($\Delta H$), and cloud thermodynamic phase (CPH) as retrieved using the Cloud Physical Properties retrieval algorithm (CPP, Roebeling et al. 2006a). The algorithm is operationally applied to reflectances and radiances observed by SEVIRI.

The CPP algorithm retrieves cloud optical thickness ($\tau$), $r_e$, and CPH in an iterative way by comparing observed SEVIRI reflectances to pre-calculated lookup table (LUT) reflectances obtained from the Doubling Adding KNMI (DAK, De Haan et al. 1987; Stammes 2001) radiative transfer model (RTM). CWP is proportional to the product of the retrieved $\tau$ and $r_e$ values. The thermodynamic phase 'water' or 'ice' is assigned to those cloud-flagged pixels for which the observed 0.6- and 1.6-$\mu$m reflectances match the corresponding water or ice cloud LUT reflectances. If phase 'ice' is assigned, an additional $T_c$ check (obtained from the 10.8-$\mu$m brightness temperature) is applied to ascertain the cloud-phase assignment. For $T_c > 265$ K, phase 'ice' is changed into 'water' (Wolters et al. 2008). It is noted that at low cloud fraction, $\tau$ and $r_e$ can be significantly under- and overestimated, respectively (Wolters et al. 2010b). To minimize retrieval artifacts resulting from low solar elevations, CPP retrievals were only performed from 7:30–16:30 UTC and limited to solar zenith angles ($\theta_\circ$) < 50°.

The separation of precipitating from non-precipitating clouds is the first step in the retrieval of precipitation intensities. Precipitating clouds are detected from CWP, $r_e$, and CPH information. Water cloud pixels with CWP values larger than $150\,\mathrm{g\,m^{-2}}$ and $r_e$ values larger than 16 $\mu$m are flagged 'precipitating', while for ice clouds all pixels with CWP larger than $150\,\mathrm{g\,m^{-2}}$ are flagged 'precipitating'. For the pixels that are flagged 'precipitating', the precipitation intensity ($P$, in $\mathrm{mm\,h^{-1}}$) is calculated using the following equation (Roebeling and Holleman 2009):

$$P = \frac{c}{\Delta H}\left[\frac{\mathrm{CWP_a} - \mathrm{CWP_o}}{\mathrm{CWP_o}}\right]^{1.6} \tag{5.1}$$

with $\mathrm{CWP_a}$ the actual condensed water path. $\mathrm{CWP_o}$ is an offset CWP value that is set at $125\,\mathrm{g\,m^{-2}}$, the constant factor $c$ has a value of 1 and is of unity $\mathrm{mm\,h^{-1}\,km}$, and $\Delta H$ is the thickness of the rain column (in km), which is defined as:

$$\Delta H = \frac{T_{c,m} - T_{c,a}}{\gamma} + dH, \tag{5.2}$$

in which $T_{c,a}$ and $\mathrm{T}_{c,m}$ denote the $T_c$ of the actual pixel and the maximum $T_c$ in a $100 \times 100$ pixel area around the actual pixel, respectively. The pixel with maximum $T_c$ is assumed to represent a low, thin cloud and thus gives an estimate of the cloud base.

The denominator $\gamma$ represents the mean adiabatic lapse rate of $6.0\,\mathrm{K\,km^{-1}}$ and $dH$ represents the minimum rain column thickness in km, which is currently set at 600 m. At the nominal SEVIRI resolution, the minimum precipitation intensity to be retrieved is dependent on $\Delta H$, but is generally in the order of $0.05\ \mathrm{mm\ h^{-1}}$. The maximum precipitation intensity is currently set at $40\ \mathrm{mm\ h^{-1}}$.

### 5.2.2 Precipitation retrieval from TRMM-PR

TRMM is a Low-Earth Orbiting (LEO) satellite that flies at an altitude of about 400 km and covers the latitudinal range between ~37° S and ~37° N. The onboard Precipitation Radar (PR) is the first dedicated active precipitation measuring instrument launched into space. The PR obtains information on precipitation at a vertical and horizontal (nadir) resolution of 250 m and 4.3 km, respectively. More details on the TRMM satellite and its instrument configuration can be found in Kummerow et al. (1998).

Because the PR suffers from considerable attenuation by large rain droplets, a correction algorithm has been developed and applied to the measured radar echo intensities ($Z$). Subsequently, the corrected radar echo intensities are converted into precipitation rates using separate droplet size distributions for stratiform and convective precipitation, which are composed of $Z$–$P$ relations measured during aircraft campaigns at various locations around the world (Iguchi et al. 2000). In this research, the near-surface observed precipitation from the TRMM PR 2A25 (version 6) product is used. The 2A25 product has been validated over West Africa using rain gauge measurements for the 1998 monsoon season (Nicholson et al. 2003) and over Florida using ground-based rain radar (Liao and Meneghini 2009). In the former study, it was found that the seasonally averaged bias of TRMM-PR is $+0.3\ \mathrm{mm\,d^{-1}}$ (+7% relative), with an RMSE of $1.9\ \mathrm{mm\,d^{-1}}$. In the latter study, a TRMM-PR overestimate for stratiform rain by 9% was revealed, whereas convective precipitation is underestimated by 19%.

### 5.2.3 CMORPH precipitation retrieval technique

CMORPH is one of the recently developed precipitation retrieval techniques that synergize LEO-observed PMW data with geostationary-observed TIR data. At present, the PMW precipi-

tation intensities are obtained from the Advanced Microwave Sounder Unit-B (AMSU-B), SSM/I, and the TRMM Microwave Imager (TMI). For the three PMW sensors, separate precipitation retrieval algorithms are used. However, to account for the different channel characteristics of AMSU-B its precipitation retrievals are normalized to those of SSM/I and TMI using a histogram matching technique. See Joyce et al. (2004) and references therein for more details on the PMW channel characteristics and normalization procedure.

Thermal infrared radiances from five geostationary satellites [the two Geostationary Operational Environmental Satellites (GOES), Meteosat-9, Meteosat-7, and the Geostationary Meteorological Satellite 5 (GMS-5)] are parallax-corrected and mapped to a 4-km grid at a temporal resolution of 30 minutes. Subsequently, these TIR data are used to calculate cloud motion vectors. For the observational gaps between two PMW instrument overpasses, the observed raining systems are propagated both forward and backward in time using the motion vectors. Finally, the forward and backward propagated precipitation is inversely weighted with the respective temporal distance from the initial and subsequent PMW instrument observations to obtain a change in intensity and shape of the precipitation systems. In this study, the 3-hourly $0.25^\circ \times 0.25^\circ$ product is used.

### 5.2.4 Evaluation of SEVIRI precipitation intensities

#### Comparison with TRMM-PR and CMORPH

As mentioned earlier, this paper first presents an evaluation of the CPP-PP precipitation observations over West Africa through a comparison with TRMM-PR using the observed areal precipitation and instantaneous precipitation intensities of SEVIRI and TRMM-PR, and the SEVIRI- and TRMM-PR-observed frequency distributions of precipitation intensity. Both comparisons have been performed for the region 0°–20° N, 10° W–10° E for May–September 2005 and 2006.

For the instantaneous comparison, initially 150 TRMM-PR overpasses were selected and collocated with the SEVIRI precipitation retrievals. Both SEVIRI and TRMM-PR retrievals were reprojected to a $0.1^\circ \times 0.1^\circ$ grid. In accordance with the TRMM-PR detection threshold of 0.5 mm $h^{-1}$ (Liao and Meneghini 2009), SEVIRI precipitation intensity retrievals below this threshold were considered as non-precipitating. For each TRMM-PR overpass, the SEVIRI image closest in time was selected, which gives a maximum time difference of ~7 min. An example of a collocated TRMM-PR overpass with SEVIRI is shown in Figure 5.1. In order to avoid possible spatial collocation mismatches, we refrained from comparing pixel-by-pixel values. Instead, the mean precipitation area and median precipitation intensity were calculated. The TRMM-PR and CPP-PP areal precipitation has been calculated by dividing the number of grid boxes for which the TRMM-PR-observed rain rate exceeded the 0.5 mm $h^{-1}$ detection threshold to the total number of grid boxes in a TRMM-PR overpass. In 23 overpasses, no rain was detected, so 127 TRMM-PR overpasses were included in the comparison dataset.

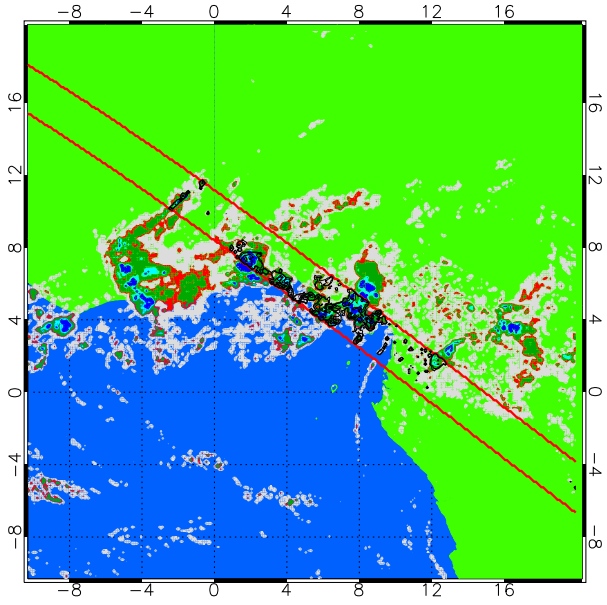


**Figure 5.1** *Example of a collocated SEVIRI image with a TRMM-PR overpass over the West African coastal area at 16 May 2006, 11:15 UTC. SEVIRI precipitation intensities are in color-filled contours, while TRMM-PR precipitation intensities are indicated by open black contours. Contour intervals are drawn at 0.1, 0.5, 1, 5, and 10 mm $h^{-1}$. The red lines indicate the edges of the TRMM-PR swath.*

Additional to the comparison of SEVIRI- and TRMM-PR-derived precipitation intensities per overpass, the relative and cumulative frequency distributions were computed for daytime TRMM-PR and SEVIRI rain retrievals at 0.1° × 0.1° with precipitation intensity exceeding 0.5 mm $h^{-1}$. Subsequently, a bootstrapping technique was applied to obtain an indication on the uncertainty of the obtained cumulative distribution functions. Using this bootstrapping technique, from the original single cumulative frequency distribution consisting of about 14,000 retrievals 10,000 new cumulative frequency distributions were computed by randomly drawing values from the original observations.

*Comparison with rain gauge observations*

Rain gauge observations from 110 stations operated within the framework of the African Monsoon Multidisciplinary Analysis project (AMMA, Redelsperger et al. 2006) were used as a third evaluation dataset. As satellite and ground-based precipitation observations are difficult to compare in terms of time series or on a pixel-by-pixel basis (areal averages observed from satellite versus point measurements from rain gauges), the rain gauge observations were only included in the comparison of the relative and cumulative frequency distributions. The stations were selected from the Gourma, Kori de Dantiandou, Niamey, and Ouémé mesoscale sites. Figure 5.2 shows the locations of the rain gauges. The majority of the rain gauge stations were operated during the monsoon seasons of 2005 and 2006.

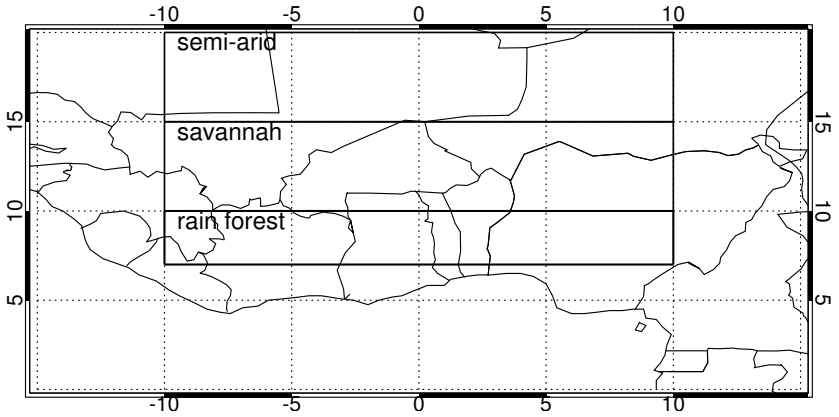


**Figure 5.2** *Locations of the 110 selected AMMA rain gauges, which were used for the validation of the CPP-PP rain retrievals, and the three regions (designated 'rain forest', 'savannah', and 'semi-arid') used for calculating the CPP-PP and CMORPH daytime diurnal cycle.*

Precipitation at these stations is recorded at a 5-min resolution. Note that different parts of clouds are sampled by rain gauges and satellites. Satellite instruments observe an area-averaged precipitation intensity of an instantaneous observation, while rain gauges sample precipitation intensity over a period of time at one location. It is assumed that rain gauge observations taken over a period of time represent a transect through a cloud system. To minimize the sampling and collocation uncertainties one needs to apply a correction procedure. Here we assumed that a cloud system remains constant over the time period between two consecutive SEVIRI images and that the averaging period of the surface observations to match the satellite pixel size is mostly a function of wind speed and wind direction. Correction procedures and their underlying assumptions to allow a proper comparison between satellite retrievals and ground-based observations are described by Greuell and Roebeling (2009) and Schutgens and Roebeling (2009) for Liquid Water Path (LWP).

However, it is noted that precipitation is of a more intermittent nature than LWP, hence the above described correction procedure would necessitate various corrections. Therefore it was chosen to simply aggregate over 15 minutes centered at the SEVIRI observation times to approximate the $0.1^\circ \times 0.1^\circ$ satellite grid boxes that were used to construct the frequency distributions. In order to preserve as closely as possible the same precipitation characteristics as observed by the satellite precipitation retrieval techniques, only daytime rain gauge measurements were included (07:30–16:30 UTC). The relative and cumulative frequency distributions were constructed by collecting all 15-minute observations having precipitation intensities $>0.5$ mm $h^{-1}$ into 0.01 mm $h^{-1}$ wide bins.

### 5.2.5 Evaluation of the monsoon progression over West Africa

In addition to the verification of the CPP-PP precipitation intensity accuracy, the detection of the WAM precipitation progression on seasonal and sub-daily scales is of interest.

To investigate the ability of CPP-PP to monitor the seasonal monsoon scale, latitudinal Hovmöller diagrams were constructed for rain occurrence frequency and precipitation intensity for the monsoon seasons of 2005 and 2006. In these periods, three data gaps in our SEVIRI data archive occurred (1–8 August 2005, 1–7 August 2006, and 24–30 September 2006), but still about 90% of the total number of daytime observations were available. The latitudinal Hovmöller diagrams were constructed from the $0.25^\circ \times 0.25^\circ$ SEVIRI and CMORPH observations.

First, all SEVIRI images were aggregated to a $0.25^\circ \times 0.25^\circ$ grid. Subsequently, for each SEVIRI image and each $0.25^\circ$ latitude grid box all retrievals with solar zenith angles less than $50^\circ$ and precipitation intensity larger than 0.05 mm $h^{-1}$ were averaged over 10°W–10°E, thus yielding at maximum 80 values per image for 0°–20° N. Subsequently, all values per latitude grid box were averaged with the number of images per day. The same was done using CMORPH data collected at 09:00, 12:00, and 15:00 UTC.

The daytime diurnal cycle of precipitation was investigated for three areas. The latitudinal bands were chosen analogously to Mohr (2004), and are primarily based on vegetation type: 7°–10° N (rain forest), 10°–15° N (savannah), and 15°–20° N (semi-desert). For clarity, these areas are indicated in Figure 5.2. Within these areas, for May–September of 2005 and 2006 all 15-min regridded CPP-PP retrievals having $P > 0.05$ mm $h^{-1}$ were collected into hourly bins (centered at 08:00, 09:00, ..., 15:00, 16:00 UTC). The solar zenith angle limit was set at $50^\circ$ to minimize retrieval artefacts contaminating the daytime precipitation signal. Subsequently, for each hour the 25th, 50th, and 75th percentiles of precipitation intensity were calculated.

## 5.3 Results

### 5.3.1 Validation of SEVIRI precipitation retrievals with TRMM-PR

Figure 5.3 presents the obtained precipitation area and median precipitation intensity per TRMM-PR overpass from SEVIRI and TRMM-PR data. The left panel in Figure 5.3 shows that the TRMM-PR and CPP-PP precipitation area agree well (corr=0.86). However, the precipitation area retrieved by CPP-PP is about 10% larger than the area observed by TRMM-PR. This difference might be a result from differences in the precipitation observation techniques of TRMM-PR and SEVIRI, or the threshold settings used to separate precipitating from non-precipitating pixels.

The scatter plot of median precipitation intensity per TRMM-PR overpass (Figure 5.3, right panel) reveals that the correlation between TRMM-PR and SEVIRI is weaker than for precipitation area. Also, the dynamic range of 0–3 mm $h^{-1}$ for TRMM-PR is smaller than for SEVIRI (0–5 mm $h^{-1}$). As noted earlier, Liao and Meneghini (2009) found that TRMM-PR retrieves lower precipitation intensities from convective systems as compared to ground-based radar observations. Part of the differences between both datasets are caused by errors due to differences in the spatial and temporal sampling.

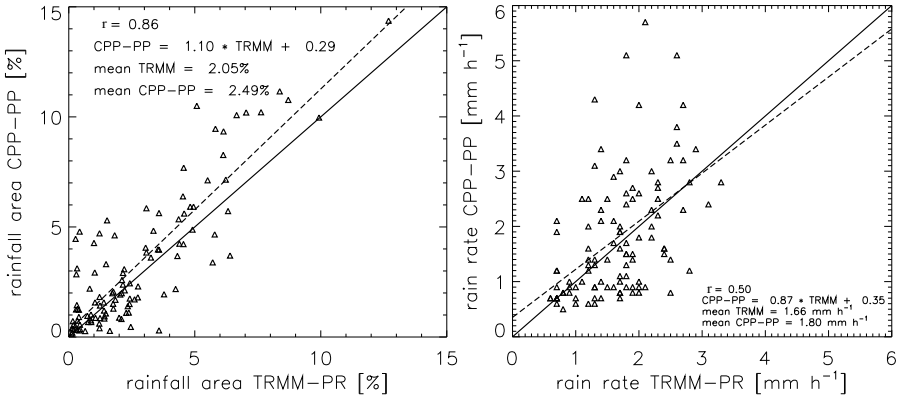


**Figure 5.3** *(Left) detected precipitation area (in % per TRMM-PR overpass) for retrievals with $P>0.5\,mm\,h^{-1}$ and (right) the corresponding median precipitation intensities per overpass as observed by TRMM-PR and SEVIRI. Solid lines indicate the 1:1 relation, dashed lines denote linear regressions.*

Roca et al. (2010) presented a method that corrects for such types of errors, and found that the correlation coefficient generally increases when these errors are accounted for in both datasets.

The cumulative and relative frequency distributions are presented in Figure 5.4. The dotted lines indicate the respective standard deviations of the cumulative frequency per precipitation intensity bin, which were calculated using the bootstrapping technique.

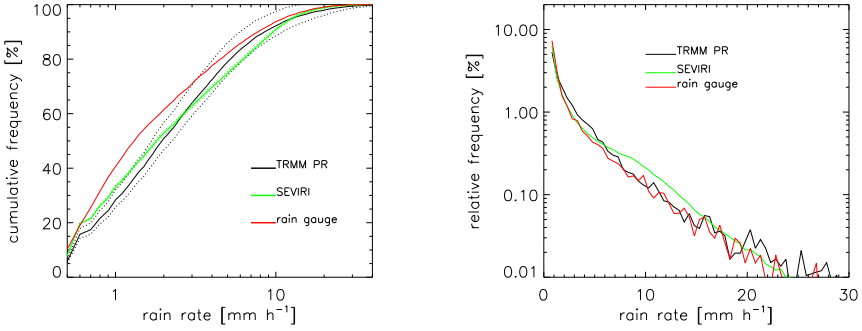


**Figure 5.4** *(Left) Cumulative frequency distribution of precipitation intensity derived from (black) TRMM-PR, (green) SEVIRI using CPP-PP, and (red) daytime (07:30–16:30 UTC) rain gauge observations from the selected stations shown in Figure 5.2. Note the logarithmic scaling on the x-axis. The accompanying dotted lines for TRMM-PR and SEVIRI denote the standard deviation at each precipitation intensity bin, which was obtained from a bootstrapping technique using 10,000 draws. (Right) corresponding relative frequency distribution for TRMM-PR, SEVIRI, and rain gauge with logarithmic scaling on the y-axis. Results were obtained for 10° W–10° E, 0°–20° N.*

From Figure 5.4, left panel, it follows that the precipitation intensities from TRMM-PR are higher than from CPP-PP up to the 60th percentile, with relative differences being below 10%. Between the 60th and 90th percentile, CPP-PP has higher precipitation intensities than TRMM-PR by 0.5–1.0 mm $h^{-1}$ (5–15% relative difference), although this overestimation diminishes beyond the 75th percentile. With respect to the AMMA rain gauge observations, both TRMM-PR and CPP-PP tend to overestimate precipitation intensities.

The relative frequency distributions (Figure 5.4, right panel) show that CPP-PP and TRMM-PR have a lower occurrence frequency than the rain gauges for $P < 1$ mm $h^{-1}$. Further, CPP-PP is higher than both TRMM-PR and the rain gauges for precipitation intensities between 5 and ~16 mm $h^{-1}$, but retrieves lower occurrence frequencies again for $P >$20 mm $h^{-1}$. The latter could be the result of an underestimation of $r_e$. In large convective systems, strong updrafts transport smaller and lighter ice crystals to the cloud top. Because for thick convective clouds the retrieved $r_e$ is only representative of the first optical thickness units (i.e., only the first few hundreds of meters) and no information on the ice crystal size at lower altitudes can be obtained, the column integrated condensed water path and hence precipitation intensity could be underestimated for these types of cloud.

### 5.3.2 Monitoring of the monsoon progression

Both the 2005 and 2006 monsoon seasons were characterized by a near-normal precipitation amount relative to the 1951–2000 mean [based on Global Precipitation Climatology Center (GPCC) data, Rudolf (1993)], although their development was different in terms of convection. First, the location of the ITCZ in 2005 was about 2° in latitude north of its climatological mean throughout almost the entire monsoon season. In addition, the 2005 monsoon onset date was earlier than the average onset date, while the 2006 monsoon contrasted with an onset due by about 10 days. Finally, colder Sea Surface Temperature (SST) in 2005 compared to 2006 occurred in the Gulf of Guinea, which for the latter year resulted in a slower monsoon development due to a smaller temperature gradient between ocean and continent (Janicot and Coauthors 2008).

To demonstrate the ability of CPP-PP to monitor the precipitation dynamics, Figure 5.5 shows the mean daytime precipitation amount for May–September 2005 for 0°–20°N, 10°W–10°E. Because CMORPH data is only available at a 3-hr resolution and due to CPP-PP retrievals being limited to daytime data, for both datasets only observations at 09:00, 12:00, and 15:00 UTC were included. For each month, precipitation retrievals were accumulated and converted to a mean daily precipitation, assuming a uniform distribution of precipitation throughout the day.

Figure 5.5 reveals that both CPP-PP and CMORPH capture the monthly shift of the monsoon rain patterns over the West African continent. In May 2005, the major rain bands are along the coastline (~5°N), with also some sporadic convection in a band near 10°N.

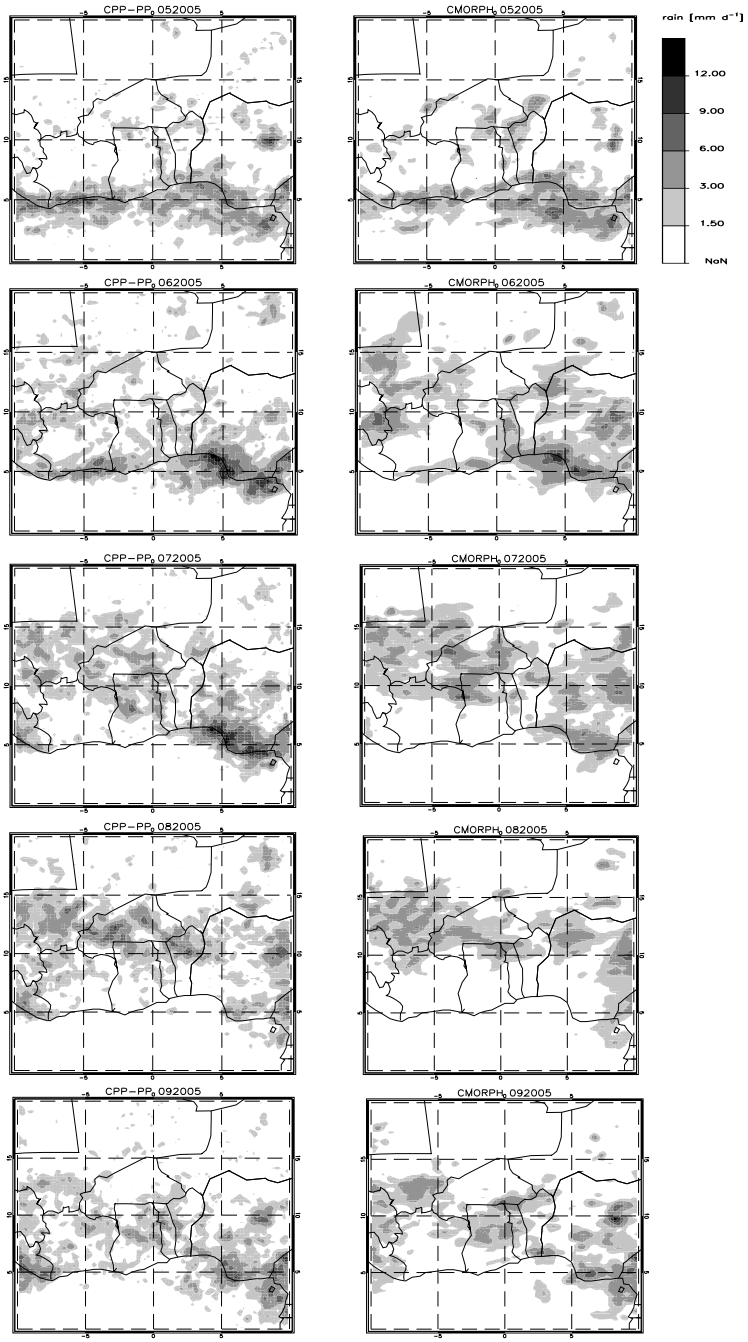


**Figure 5.5** *Mean accumulated daily precipitation (expressed in mm d$^{-1}$) for May–September 2005 from (left) CPP-PP and (right) CMORPH. For both datasets observations at 09:00, 12:00, and 15:00 UTC were included. See text for further details.*

The eastward part of this band as well as some parts of the coastal rain band are observed somewhat more prominently by CPP-PP than by CMORPH.

In June 2005, CPP-PP retrieves higher precipitation intensities along the West African coast than CMORPH. This is particularly evident in the western part, where CMORPH partly has a mean daytime precipitation of <3 mm $d^{-1}$, while CPP-PP retrieves values of 3–6 mm $d^{-1}$. Furthermore, the precipitation over the continent west of 0° is observed as smaller scale convection by CPP-PP. This is likely the result of the coarser resolution of CMORPH. Despite the usage of geostationary IR radiances at 4×4 km, the CMORPH data resolution is limited by the relatively large PMW instrument sampling resolution [~10-15 km, Joyce et al. (2004)]. The rapid movement of the major rain systems between June and July 2005 is seen by both CPP-PP and CMORPH, with both the location and intensity largely in agreement. As for May and June, CPP-PP observes more intense rains along the eastern West African coast than CMORPH, which seems to be more in agreement with the GPCC observations (not shown).

In August, the monsoon rains have reached their northernmost position and daytime rain totals are less than 3 mm $d^{-1}$ along the coast. Most rain is observed in the western part of West Africa (with several areas having 6-9 mm $d^{-1}$), which may be due to initiation and/or (re)activation of MCSs/squall lines over the Aïr mountains (Mohr 2004). In September, the monsoon rains have retreated southward and in general their intensity has decreased.

Figure 5.6 shows latitudinal Hovmöller plots from CPP-PP and CMORPH daytime precipitation retrievals for May–September 2005 and 2006. As for Figure 5.5, the general features and seasonal march of the monsoon of CMORPH and CPP-PP agree fairly well, with the correlation coefficient of non-zero precipitation intensities being 0.64 and 0.76 for 2005 and 2006, respectively. For both datasets and both years, the southward retreat of the monsoon rains is more pronounced than the northward movement during May–July. It is suggested that the northward displacement of the monsoon rains occurs at different speeds along the longitudes investigated (10°W–10°E). Some evidence of this can be seen in Figure 5.5 for June and July 2005; the monsoon rains west of 0°E have reached as far as ~13–15°N, while east of 0°E the monsoon rains are located roughly 3° more southward. The slower movement east of 0°E is possibly due to blocking and forced convection on the windward side of the Cameroon Highlands (near 7°N, 9°E).

For 2005 (Figures 5.6a and 5.6c), CPP-PP retrieves higher precipitation intensities (up to 1.3 mm $h^{-1}$, but mostly 0.2–0.4 mm $h^{-1}$, not shown) than CMORPH along the coastline during June and July, a feature which is also visible in Figure 5.5. The higher precipitation intensities than CMORPH are compensated for by several lower precipitation intensities (mainly over the continent, e.g. 10°–15°N during the first part of June), which is reflected by a mean difference between CPP-PP–CMORPH of 0.0±0.16 mm $h^{-1}$. In both datasets the monsoon rains reach their northernmost position at ~15° N during late July and early August. Finally, from late August onwards the monsoon rains retreat southward, which is well visible in both CPP-PP and CMORPH.

The seasonal signature of the 2006 WAM (Figures 5.6b and 5.6d) is different than that of 2005. In both CMORPH and CPP-PP a larger latitudinal extent of the oceanic/coastal rains (~2-6°N) during the early monsoon (May and June) is seen. In addition, during late June and early July a decrease in the latitudinal extent of these rain bands is observed, a feature also recognizable when precipitation is averaged over multiple years (Hagos and Cook 2007). As for 2005, CPP-PP retrieves higher precipitation intensities in the coastal area (up to 7°N) than CMORPH, but the difference is larger than for 2005, with differences occasionally > 0.5 mm $h^{-1}$. The mean difference is +0.05±0.21 mm $h^{-1}$. CPP-PP retrieves higher precipitation intensities than CMORPH until around mid-July, after which the maximum precipitation shifts towards ~12°N. In CMORPH, the monsoon jump is observed around the same date and at approximately the same location.

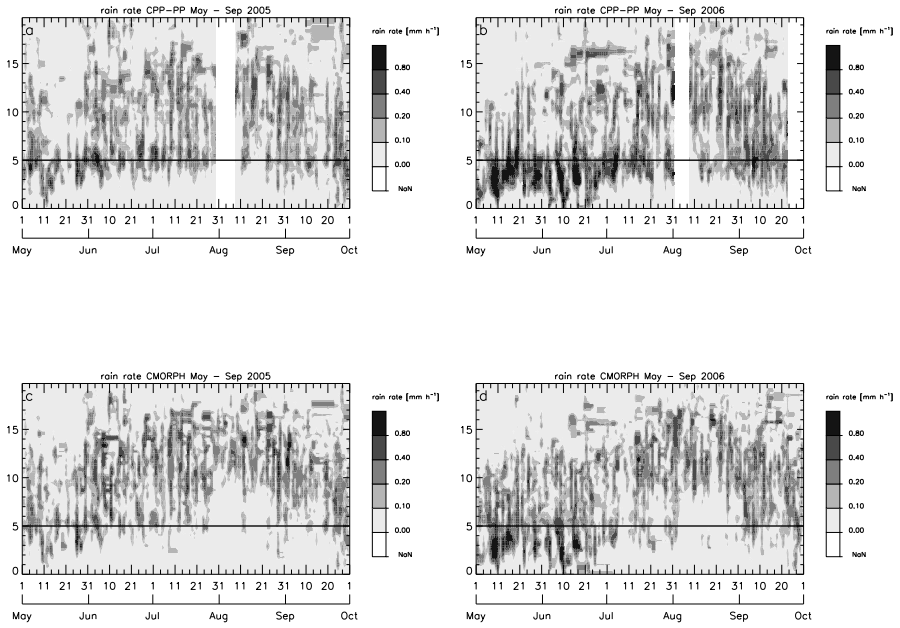


**Figure 5.6** *Hovmöller plots of (left) 2005 and (right) 2006 daytime conditional precipitation intensity ($P>0.05\,mm\,h^{-1}$) for 0°–20° N; (top) CPP-PP and (bottom) CMORPH. Both datasets are at 0.25°×0.25° resolution. Values have been averaged over 10° W–10° E. The thick horizontal line denotes the approximate location of the coastline. The white bands in the CPP-PP plots indicate data archive gaps.*

The fair agreement between the CPP-PP and CMORPH Hovmöller plots is emphasized in Figure 5.7, which shows latitudinal cross sections of the monthly mean precipitation intensity from CPP-PP and CMORPH for May–September 2005 and 2006.

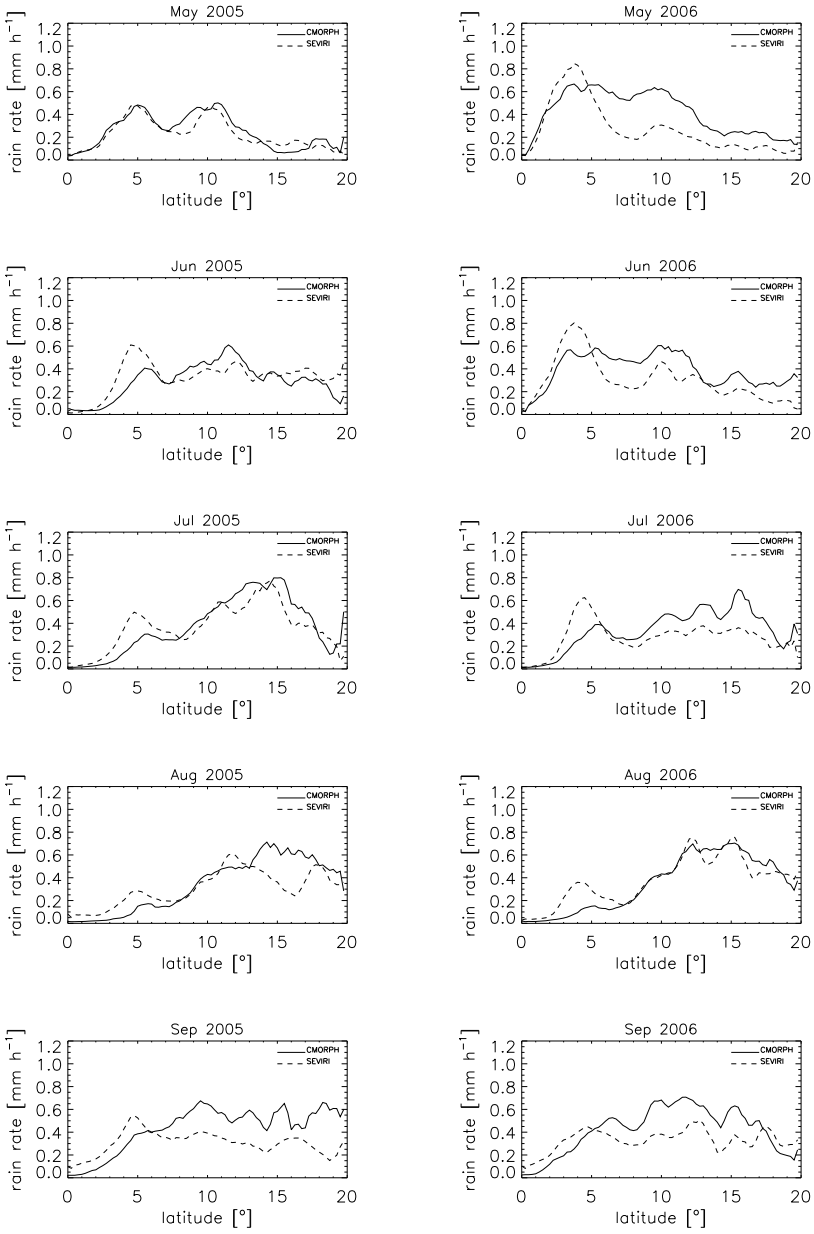


**Figure 5.7** *Latitudinal cross section of monthly mean daytime conditional precipitation intensity ($P > 0.05\,mm\,h^{-1}$) from CMORPH (solid line) and CPP-PP (dashed line) for (left) May–September 2005 and (right) May–September 2006. Both datasets are at $0.25° \times 0.25°$ resolution.*

Over the continent (>~5°N), the differences between CPP-PP and CMORPH are generally small, although CMORPH has larger values than CPP-PP in 2006. In both years, CPP-PP has larger precipitation intensities than CMORPH over the coastal areas. It was noted by Sapiano and Arkin (2009) that CMORPH likely overestimated convective precipitation over land. Further, we again refer to CPP-PP having a better agreement in the coastal areas with GPCC-observed precipitation amounts than CMORPH.

Figure 5.8 presents the 2005 and 2006 Hovmöller plots of CPP-PP- and CMORPH-retrieved precipitation occurrence frequency. Similar to the precipitation intensity plots, correlation between the two datasets is high (0.70 and 0.76 for 2005 and 2006, respectively). In addition, as for precipitation intensity, CPP-PP retrieves a higher precipitation occurrence frequency in the coastal area, with overestimations up to 28%. The mean difference CPP-PP–CMORPH is -0.1±6.6% and +4.2±9.8% for 2005 and 2006, respectively.

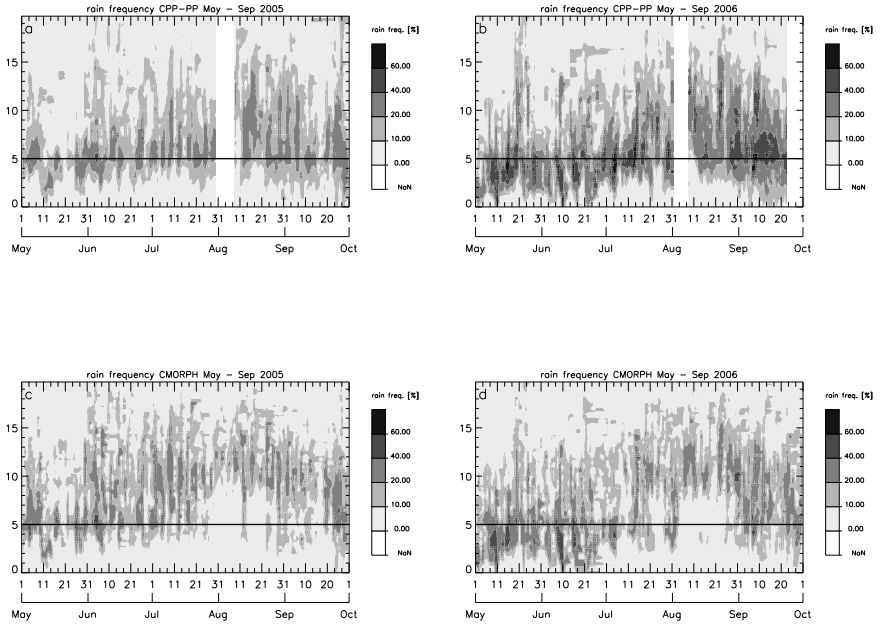


**Figure 5.8** *As in Figure 5.6, but for precipitation ocurrence frequency.*

### 5.3.3 Daytime diurnal cycle of precipitation

Figure 5.9 shows the daytime diurnal cycle of precipitation intensity and precipitation occurrence frequency for CMORPH and CPP-PP over three regions (see also Figure 5.2), averaged over May–September 2005 and 2006: 7°–10° N, 10°–15° N, and 15°–20° N, with all areas having longitudinal extents 10° W–10° E. Note that both datasets are at 0.25° × 0.25° grid. For convenience, the regions are designated as 'rain forest', 'savannah', and 'semi-desert', respectively, consistent with the analysis of Mohr (2004). To reduce noise in the results, only precipitation intensities larger than 0.05 mm $h^{-1}$ were included.

Over the rain forest region (7°–10° N), the median precipitation intensity shows a small decline during morning and early afternoon and slowly increases during the afternoon in May. The region is close to the monsoon rains, which probably causes the reduced dynamical range (see also the 75th percentile), as more dynamically driven convection occurs. The agreement with CMORPH is good, with a small underestimation of ≈0.1 mm $h^{-1}$ by CPP-PP for all three percentiles shown. Note that the CPP-PP plots are at an hourly resolution averaged from the 15-minute observations, whereas those for CMORPH are given per 3 hours.

During June and July, the dynamics in daytime precipitation cycle as retrieved from CPP-PP increase as the ITCZ has passed the region; the median (75th percentile) precipitation intensity decreases from 0.35 (1.6) mm $h^{-1}$ at 08:00 UTC to 0.2 (0.6) mm $h^{-1}$ around noon, after which the precipitation intensities increase towards the end of the CPP-PP observation period (the bin centered at 16:00 UTC). Compared to CPP-PP, CMORPH has a much smaller daytime precipitation cycle. This may be due to several factors, among others the use of TIR data to interpolate and morph precipitation intensities between PMW instrument overpasses, which smooths the daytime precipitation signal. In August and September, the dynamical range in daytime precipitation as retrieved by CPP-PP decreases again slightly, as the ITCZ retreats southward and the daytime cycle of precipitation is less dominated by differential heating. This is possibly due to the occurrence of MCSs, which can be maintained throughout the night due to dynamical forcing and cloud-top radiative cooling (Dai 2001; Yang and Smith 2006).

Similar to the rain forest region, over the savannah and semi-desert region the dynamical range of precipitation during daytime decreases when the monsoon rain bands pass (see for example the difference between May and July for the savannah region, Figure 5.9, middle column). In addition, as for the rain forest region, for almost all months CPP-PP has lower absolute precipitation intensity values compared to CMORPH. In addition, the dynamical range of the daytime precipitation cycle is larger from CPP-PP than from CMORPH. Finally, the higher percentiles of CPP-PP have a larger amplitude than those from CMORPH. With respect to the lower precipitation intensity values of CPP-PP relative to CMORPH over the continent, it is mentioned that CMORPH tends to overestimate the precipitation over these areas (Sapiano and Arkin 2009). Furthermore, Tian et al. (2010) found this overestimation particularly occurring during the summer season, i.e., when convective processes dominate precipitation formation.

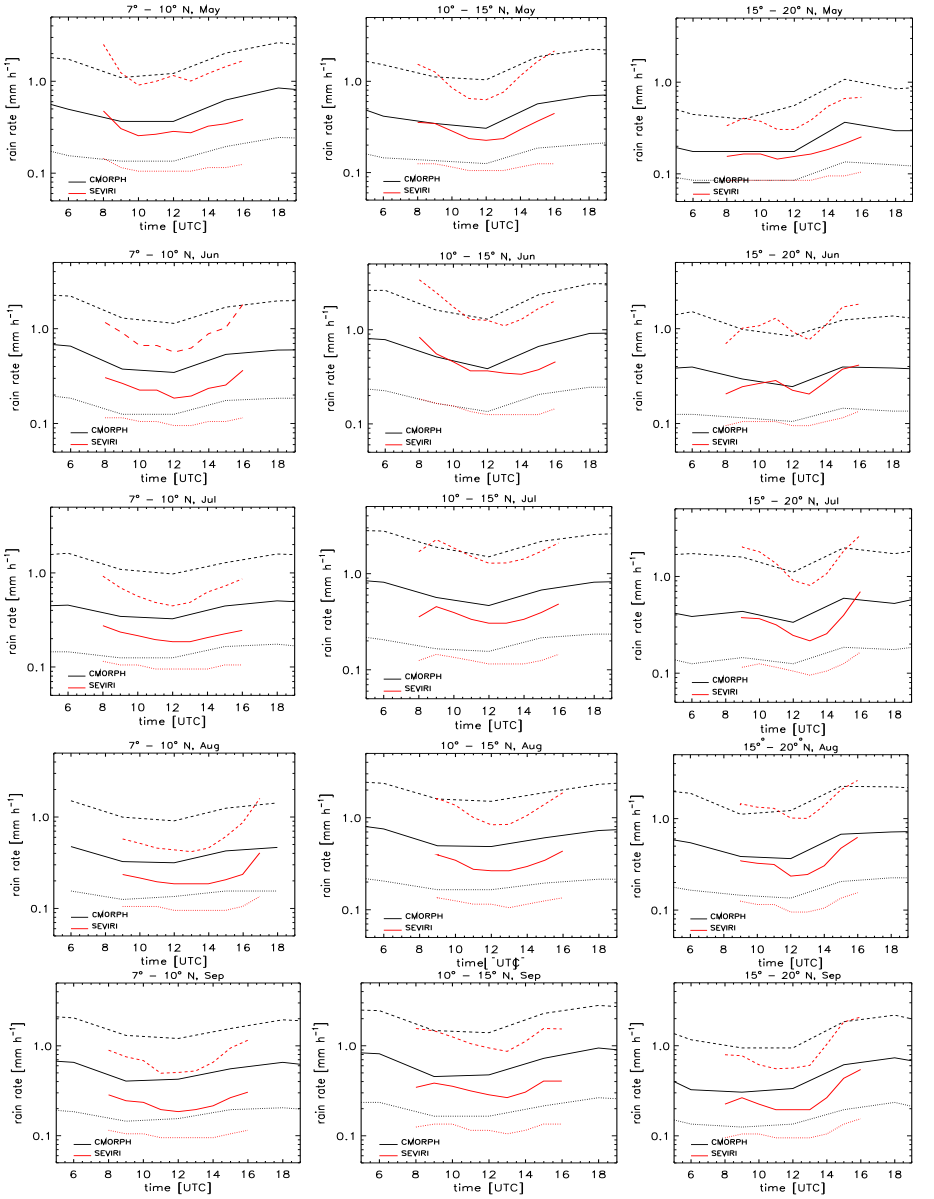


**Figure 5.9** *(Black) CMORPH and (red) CPP-PP daytime diurnal cycle of precipitation intensity (for values with $P > 0.05$ mm $h^{-1}$) from May–September (averaged over 2005 and 2006) for (left column) 7°–10° N, (middle column) 10°–15° N, and (right column) 15°–20° N. Values were averaged over 10° W–10° E, CPP-PP precipitation retrievals were collected in hourly bins. The 25th (dotted), 50th (solid), and 75th (dashed) percentiles are shown.*

## 5.4 Summary and conclusions

This Chapter presented the evaluation of the CPP-PP precipitation retrieval algorithm on SEVIRI visible and near-infrared reflectances over West Africa for May through September of 2005 and 2006. The algorithm combines retrieved cloud particle effective radius, cloud phase, and cloud-top temperature information to estimate precipitation intensity. Instantaneous precipitation retrievals were compared against TRMM-PR and rain gauge observations. CPP-PP is well able to capture the precipitation characteristics observed by TRMM-PR; the areal precipitation retrieved by CPP-PP of 2.5% is higher than the corresponding value from TRMM-PR of 2.0%, which is a satisfactory agreement given the different measurement techniques. Further, it was shown that the mean retrieved precipitation intensity from CPP-PP is ≈8% higher than from TRMM-PR. Examination of the TRMM-PR and CPP-PP cumulative frequency distributions revealed that differences between CPP-PP and TRMM-PR are generally within +/-10%. Relative to the AMMA rain gauge observations, CPP-PP shows very good agreement up to 5 mm $h^{-1}$, however, at higher precipitation intensities (5–16 mm $h^{-1}$) CPP-PP overestimates compared to the rain gauges.

A second goal of this paper was to demonstrate to which extent the CPP-PP precipitation retrievals can be used to monitor the seasonal progression of the WAM and the precipitation characteristics at sub-daily time scale. It was shown that both the accumulated precipitation and the seasonal progression of precipitation throughout the WAM have good agreement with CMORPH, although CPP-PP retrieves higher precipitation amounts over the coastal region of West Africa. Using latitudinal Hovmöller diagrams, again a fair correspondence between CPP-PP and CMORPH was found, which is reflected by high correlation coefficients (≈0.7) for both precipitation intensity and precipitation occurrence frequency.

The daytime diurnal cycle of precipitation from CPP-PP shows distinctly different patterns for three different regions throughout the WAM, with a decrease in dynamical range in the vicinity of the ITCZ, a feature which is attributed to the occurrence of dynamically driven convective systems being dominant over convection forced through differential heating of the land surface. The dynamical range of the daytime precipitation cycle as retrieved from CPP-PP is larger than that from CMORPH.

We speculate this to be both resulting from the better spatio-temporal resolution of the SEVIRI instrument, as well as from thermal infrared radiances being partly used in CMORPH, which likely smooth the daytime precipitation signal, especially when cold anvils from convective systems are present. Another feature emerging from the comparison of the CPP-PP and CMORPH daytime cycles is that although CPP-PP has a larger dynamical range of daytime precipitation than CMORPH, the absolute value of the separate percentiles is lower. On the other hand, it was pointed out that the absolute value of CMORPH daytime precipitation dynamical range is likely too high, due to the tendency of CMORPH to overestimate precipitation of convective systems over continental areas.

The unprecedented 15-min temporal resolution in combination with the 3×3 $km^2$ spatial sampling of SEVIRI makes it a well-suited instrument to monitor precipitation features, both

at sub-daily and at seasonal scale. Over West Africa, about 40 precipitation retrievals per day can be performed for a single location, which makes SEVIRI a suitable instrument to monitor year-to-year changes in daytime precipitation patterns. In contrast, the TRMM satellite captures a full diurnal cycle once every 47 days, which necessitates at least several years of data to obtain substantial statistics.

Without neglecting the differences between CPP-PP–TRMM-PR and CPP-PP–CMORPH, the overall results show that the CPP-PP algorithm has a promising accuracy in retrieving precipitation intensity and precipitation occurrence over tropical areas. As already pointed out by Ebert et al. (2007) and Sapiano and Arkin (2009), it is difficult to assess a "best" precipitation retrieval algorithm, as each algorithm has its strengths and weaknesses, which are for the largest part imposed by instrumental constraints. For example, PMW precipitation observations relying on the emission of hydrometeors have problems over land surfaces, as both the intensity and heterogeneity of the surface background emission reduces the signal-to-noise ratio.

For the CPP-PP algorithm, its strengths exist in the use of retrieved cloud-top properties from SEVIRI to estimate precipitation intensity, which is more physically based than e.g. the widely used Cold Cloud Duration techniques developed in the 1970s and 1980s. In addition, the retrieved cloud-top properties are observed by the same instrument, which excludes the usage of merging and normalization procedures, such as in CMORPH. On the other hand, the availability of CPP-PP precipitation retrievals is currently limited to daytime only, due to its dependency on VIS/NIR reflectances. During nighttime, SEVIRI only provides observations from the water vapor (6.2 $\mu$m and 7.3 $\mu$m) and thermal infrared (8.7 $\mu$m–13.4 $\mu$m) spectral channels. These channels might be useful to continue our present daytime precipitation retrievals during the night. For example, Behrangi et al. (2009) showed that using all channels from 6.2 $\mu$m–13.4 $\mu$m improves the precipitation retrieval evaluation statistics compared to those for the 10.8 $\mu$m channel only.

Second, because precipitation occurs generally in thick clouds and the usage of passively observed reflectances implies that precipitation intensity is estimated from cloud-top properties, no information from lower atmospheric layers is available. Especially in the tropics, a too high precipitation intensity may be retrieved, due to a considerable amount of the precipitation at cloud base being evaporated before reaching the surface. This below-cloud evaporation fraction may add up to 40%, depending on cloud base height, precipitation intensity at cloud base, and the below-cloud relative humidity (Rosenfeld and Mintz 1988). Implementation of a correction for below-cloud evaporation [e.g. Petty (2001)] is planned to be incorporated in future versions of CPP-PP.

Being operational since 2004, SEVIRI enables obtaining a substantial statistical dataset to study the interaction between cloud-top properties, precipitation and for example the large-scale dynamics or land surface characteristics (soil moisture, vegetation, etc.). These process studies are useful to evaluate among others the cloud, precipitation, and land surface–atmosphere interaction predictions of regional climate models [see e.g. the work of Greuell et al. (2011) and Roebeling and van Meijgaard (2009)].

# Chapter 6

## A soil moisture–precipitation feedback study over West Africa

This Chapter describes a study on the relation between soil moisture and convective precipitation over West Africa, using soil moisture retrievals from Advanced Microwave Scanning Radiometer EOS (AMSR-E) brightness temperatures and daytime (7:30–16:15 UTC) precipitation retrievals obtained from Scanning Enhanced Visible and Infrared Imager (SEVIRI) visible and near-infrared reflectances. For the 2005 and 2006 monsoon seasons, soil moisture anomalies from the AMSR-E dataset were calculated in 2°×2° blocks. Using the lowest and highest 10% of the soil moisture anomalies distribution to represent dry and wet land surfaces, respectively, the SEVIRI-based precipitation occurrence frequency and intensity over these surfaces at the following day were calculated. The increase in precipitation occurrence frequency after 13:00 UTC was observed over the entire domain, but was especially strong over dry surfaces. No significant difference in precipitation intensity was observed between wet and dry surfaces. This research has demonstrated the potential of satellite-based soil moisture and precipitation datasets for improving the understanding of the soil moisture–precipitation interactions.

Wolters, E.L.A., B.J.J.M. van den Hurk, and R.A. Roebeling, 2011: A soil moisture–precipitation feedback study over West Africa using SEVIRI and AMSR-E observations, *in revision for J. Hydrometeorol.*

### 6.1 Introduction

Land–atmosphere interactions occur at various spatial and temporal scales. One of these land–atmosphere surface processes taking place is the interplay between soil moisture and precipitation in certain areas of the world. In models, anomalies in soil moisture are found to have an impact on precipitation (Koster et al. 2004). While the effect of precipitation on soil moisture is a trivial positive feedback mechanism, i.e., that precipitation increases soil moisture, the effect of soil moisture on the initiation of convection and hence precipitation is less straightforward and has therefore been subject of a considerable amount of research efforts [see for example Dirmeyer et al. (2006) and Ferguson and Wood (2011)].

In this interaction mechanism, a trade-off exists between increased moist static energy and net radiation on one hand and suppressed sensible heat leading to boundary layer growth on

the other hand. Model experiments performed by Alonge et al. (2007) demonstrated that both the net radiation (due to a lower surface albedo) and moist static energy are larger over wet surfaces than over dry surfaces. Findell and Eltahir (1997) showed from soil moisture and rain gauge precipitation observations for the state of Illinois that especially during summer wet surfaces are positively correlated with subsequent precipitation, which is caused by a larger evaporation and hence atmospheric water vapor supply over these surfaces (Findell et al. 2011). In a more detailed case study over West Africa, which is also the area of interest here, Taylor et al. (2010) demonstrated that although mesoscale convective systems hardly initiate over wet surfaces, precipitation initiated upstream is strengthened over these surfaces. It was suggested that among others the downdraft on the leading edge of the convective system could force moist convection over wet surfaces. They also noted that the gradients in soil moisture are of higher importance to convective initiation than the absolute soil moisture values. This latter suggestion was confirmed by Taylor et al. (2011), who found that the probability of convective initation doubles over strong soil moisture gradients at distances of 10–40 km compared to over surfaces which have a more homogeneous horizontal soil moisture distribution. Taylor and Ellis (2006) demonstrated from satellite observations that precipitation during the afternoon is inhibited if surfaces are too wet. Soil wetness was also found to affect both the horizontal movement and intensity of large tropical convective systems (Wolters et al. 2010a).

Over dry surfaces, water from the surface that can be converted into clouds is limited, while the surface sensible heat flux can trigger deep convection if atmospheric stability and water vapor content permit (Findell and Eltahir 2003a;b; Hohenegger et al. 2009). Favorable conditions for convection for example occur when moist air is advected over dry surfaces. In addition, model simulations by Garcia-Carreras et al. (2011) showed that convection may be favored over dry surfaces close to dry-wet transitions. As a result of the differential heating between the wet and dry soil patches, a surface-induced shallow airflow develops, which can cause convergence and hence forces the air to ascent when opposing the large-scale wind. The existence of such dry soil–precipitation interaction was confirmed through satellite observations by Taylor et al. (2011).

One of the regions identified in the model study by Koster et al. (2004) to have a potential strong dependency of precipitation on soil moisture anomalies is the West African Monsoon (WAM) region. Taylor et al. (2002) pointed out that anthropogenically induced land use changes in this region could cause a delayed wet season onset due to a decreased vegetational coverage and hence a limited efficiency of the surface to recycle water. Further, van den Hurk and van Meijgaard (2010) found that the interaction between soil moisture and subsequent precipitation in the Sahel zone is strongly constrained by atmospheric quantities such as available convective energy and atmospheric moisture.

Most of the research efforts on the soil moisture–precipitation coupling have been performed through the use of (regional) climate or numerical weather prediction models and to a lesser degree from direct observations. One of the reasons for the small amount of observational investigations is that in situ soil moisture observations are rather sparse and are not always taken on a routine basis. In addition, soil moisture has a large spatial variability, which necessitates a large amount of in situ observations to obtain a representative picture of soil moisture at the

mesoscale (de Rosnay et al. 2009). However, using satellite-observed microwave brightness temperatures enables soil moisture observations over large areas and at a sufficient spatial resolution to study land–atmosphere interactions at the mesoscale (~50–100 km). For example, the studies of Taylor and Ellis (2006) and Taylor et al. (2010) use soil moisture obtained from Tropical Rainfall Measurement Mission Microwave Imager (TRMM-TMI) and AMSR-E brightness temperatures, respectively.

Soil moisture retrievals from space have been available since 1978 from passive microwave brightness temperature observations. More recently, also soil moisture retrievals using scatterometer data have become available. For example, Wagner et al. (1999) and Bartalis et al. (2007) use measured radar backscattering coefficients observed by the scatterometer onboard the European Remote Sensing Satellite-2 (ERS-2) and the Advanced Scatterometer (ASCAT) onboard the Meteorological Operational Satellite (MetOp) for retrieving soil moisture with a spatial resolution of ~50 km.

In this study, a soil moisture dataset derived from microwave brightness temperatures observed by the Advanced Microwave Scanning Radiometer onboard the Earth Observing System (EOS) Aqua satellite (AMSR-E) is used. We investigate the relation with subsequent precipitation as retrieved using the Cloud Physical Properties–Precipitation Properties (CPP-PP) from Spinning Enhanced Visible and Infrared Imager (SEVIRI) reflectances onboard Meteosat-8 and -9. This research provides a first-order estimate of the interaction between soil moisture anomalies and convective precipitation by solely using satellite retrievals. In addition, the possibilities of using satellite-retrieved soil moisture and precipitation datasets in hydrological applications are demonstrated.

Mesoscale convective systems contribute considerably to the total precipitation in West Africa (Laing et al. 1999; Mathon et al. 2002), and although most of these systems are dynamically forced, they can be influenced by the underlying land surface characteristics. Therefore the research question we address in this study is whether the precipitation occurrence and intensity of these convective systems that are initiated during daytime is significantly different over wet surfaces than over dry surfaces.

The research is outlined as follows. The principles to retrieve precipitation information from SEVIRI reflectances and soil moisture information from AMSR-E microwave brightness temperatures, as well as data analysis methods are explained in Section 6.2. Results of the soil moisture–precipitation interaction study are presented in Section 6.3, after which these are discussed and conclusions are drawn in Section 6.4.

## 6.2 Soil moisture and precipitation datasets

### 6.2.1 CPP-PP retrieval algorithm

The Cloud Physical Properties - Precipitation Properties [CPP-PP, Roebeling and Holleman (2009)] retrieval algorithm derives precipitation occurrence and intensity using cloud-top

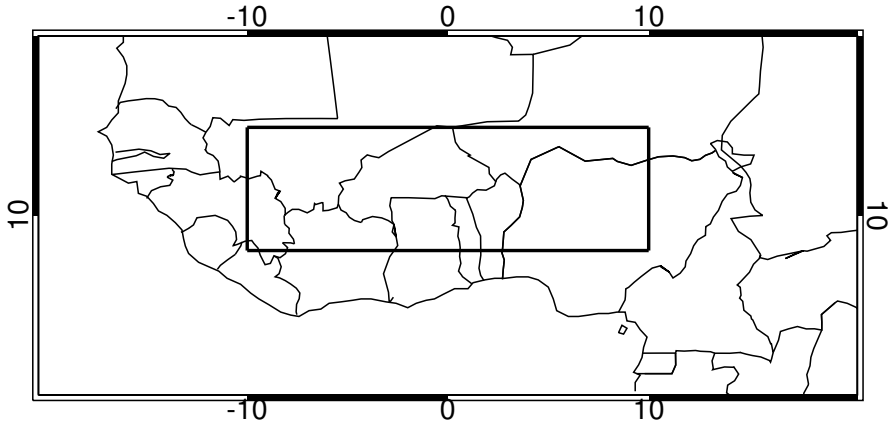


**Figure 6.1** *Depiction of the study area. The soil moisture–precipitation relation is studied within the solid-lined area.*

properties that are retrieved from visible and near-infrared reflectances observed by SEVIRI, which observes at a nominal resolution of 3×3 km$^2$ over the area of interest. This implies that only daytime values can be retrieved (07:30–16:15 UTC). The discrimination between precipitating and non-precipitating clouds is done using thresholds for cloud particle effective radius ($r_e$) and condensed water path (CWP). For water clouds, clouds are labeled as 'precipitating' if $r_e$ is larger than 16 $\mu$m and CWP exceeds 150 g m$^{-2}$, whereas for ice clouds only the latter criterion needs to be fulfilled, because the precipitation formation process is more efficient when ice crystals are present in the cloud top. Precipitation intensity is calculated from a scaling of CWP with the precipitation column thickness, which in turn is estimated from the difference between the thermal infrared-based cloud-top temperature and the warmest pixel (lowest cloud) found in a 100×100 pixel region, which corresponds to ~300×300 km$^2$ over West Africa. See for more details on the CPP-PP algorithm Roebeling and Holleman (2009) and Wolters et al. (2011).

### 6.2.2 AMSR-E soil moisture retrieval algorithm

The AMSR-E instrument flies onboard the polar orbiting EOS Aqua satellite, which has a local overpass time of 1:30 and 13:30 for the descending and ascending nodes, respectively, and has been operating from 2002 until October 2011. AMSR-E measured brightness temperatures at frequencies ranging from 6.9–89 GHz at horizontal and vertical polarizations. The spatial resolution ranged from 56×56 km$^2$ to 5×5 km$^2$ between 6.9 and 89 GHz, respectively.

The physical principle to derive soil moisture information from passive microwave observations is a relation between soil moisture and the surface emissivity. While the microwave surface emissivity over bare dry surfaces is about 0.95, over bare wet surfaces it decreases to about 0.6. As a consequence, the microwave brightness temperature measured over wet

surfaces is lower than over dry surfaces. The retrieved soil moisture, which is obtained from the AMSR-E 6.9 and 10.65 GHz channels, represents the soil water content in the upper 1-1.5 cm of the soil (Owe et al. 2008). The soil moisture retrieval is hampered over dense vegetation (Njoku et al. 2005), where the emitted microwave radiance is dominated by plant leaves and hence insufficient information on soil moisture can be retrieved. The soil moisture retrievals from AMSR-E used in this study were obtained from an algorithm that was developed in a joint effort by the National Aeronautics and Space Administration (NASA) and the Free University of Amsterdam and is part of a historical soil moisture climatology that was constructed from various microwave instruments dating back to 1978 (Owe et al. 2008). It uses a Land Parameter Retrieval Model (LPRM) that incorporates the 6.9-GHz and 10.65 GHz vertical and horizontal polarized brightness temperatures to obtain information on the relative permittivity of the canopy and soil to microwave radiation. AMSR-E soil moisture retrievals have been evaluated using various in situ soil moisture measurements over midlatitude and tropical areas [see for example the studies of Gruhier et al. (2010; 2008) and McCabe et al. (2005)]. Generally, the AMSR-E soil moisture retrievals have a reasonable to good performance; Gruhier et al. (2010) found an annual bias of 5.9% between the AMSR-E soil moisture retrievals and in situ observations over four ground sites in Mali.

### 6.2.3 Data analysis

Figure 6.1 indicates the studied region (10°W–10°E, 8°–15°N). The southern edge of this region contains rain forest, while to the north the vegetation changes into savannah and even desert-like. Some elevated terrain is located to the east of the region, which could affect convective initiation in the dominant easterly flow of the African Easterly Jet (Dinku et al. 2007).

AMSR-E soil moisture retrievals were made available through the Atmospheric Data Access for the Geospatial User Community (ADAGUC) web portal of the Free University of Amsterdam. Here we use the $0.25° \times 0.25°$ daily soil moisture data for May–September of 2005 and 2006. Because West Africa is sampled only twice per day (around 1:30 and 13:30 LT), it is possible that wet soil moisture anomalies are sampled that are resulting from precipitation a few hours before. As we are only interested in the influence of soil moisture on the initiation and occurrence of subsequent precipitation and not vice versa, the precipitation retrievals were matched to soil moisture retrievals from the preceeding AMSR-E overpass of 1:30. This is motivated by the fact that the Planetary Boundary Layer generally develops at a daily scale (Betts 2004).

CPP-PP precipitation retrievals were obtained from 7:30–16:15 UTC. This implies a time difference of 6–15 hours between the nighttime soil moisture observations and the first daytime precipitation retrievals. It is implicitly assumed that the observed soil moisture anomaly patterns remain constant throughout this period. In order to support this assumption, we filtered out influences from convective systems that persist throughout the night. The filtering was applied by discarding grid points for which at 7:30 UTC rainfall was detected within a radius of ~250 km.

Spatial soil moisture anomalies were obtained using 8×8 AMSR-E pixel areas (~220×220 km$^2$) from which the soil moisture difference (in m$^3$ m$^{-3}$) between the center 2×2 and the surrounding pixels, $\Delta\theta$, was computed:

$$\Delta\theta = \theta_c - \theta_s, \tag{6.1}$$

with suffixes $c$ and $s$ referring to the center and surrounding AMSR-E pixels within the 8×8 pixel areas. The above equation defines $\Delta\theta > 0$ and $\Delta\theta < 0$ as wet and dry (spatial) anomalies, respectively.

Subsequently, for each month all $\Delta\theta$ values were aggregated into a cumulative frequency distribution and the lowest and highest 10% were selected to be further investigated as dry and wet anomaly datasets, respectively. It is noted that only the 2× 2 AMSR-E center pixels and not the surrounding pixels were included as either dry or wet anomaly patches.

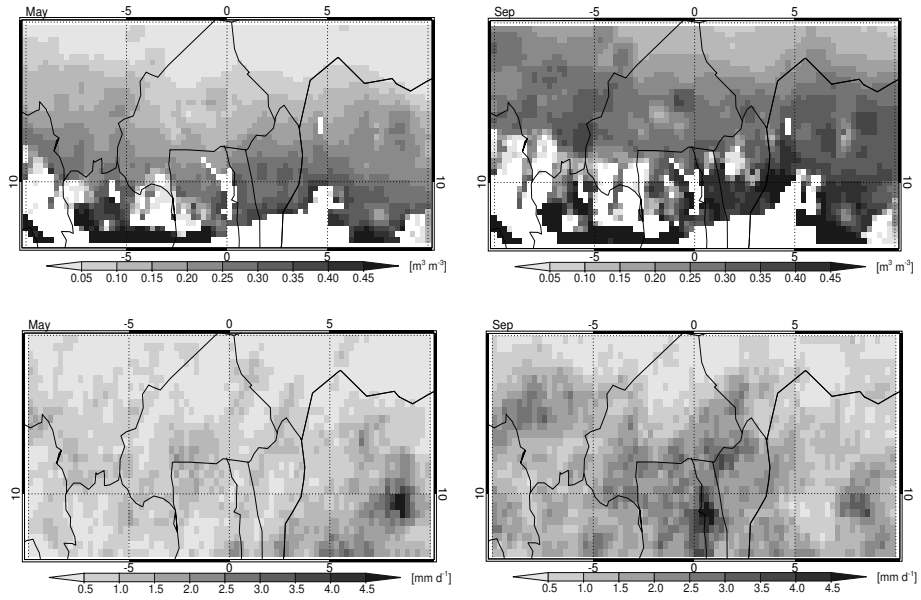


**Figure 6.2** *(Top panels) AMSR-E soil moisture as observed from the 1:30 LT overpasses for (left panel) May and (right panel) September averaged over the years 2005–2006. White areas indicate the absence of soil moisture retrievals as a result of dense vegetation. (Bottom panels) Averaged daytime precipitation (7:30–16:15 UTC) for (left panel) May and (right panel) September 2005–2006 as retrieved by CPP-PP. For convenience, CPP-PP retrievals were regridded to the AMSR-E 0.25° × 0.25° resolution.*

For the 2×2 AMSR-E center pixels that were flagged as dry or wet, the occurrence frequency from the daytime-observed SEVIRI reflectances at the subsequent day were computed by dividing the number of precipitation-flagged SEVIRI pixels by the total number of SEVIRI pixels within the 2×2 AMSR-E pixel area (~300 at nominal resolution). Precipitation intensities of

the 10 investigated months (May–September of 2005 and 2006) were collected in a cumulative histogram, from which the 17th, 50th, and 84th percentile were calculated. Q67 is defined as the difference between the 84th and 17th percentile.

## 6.3 Results

Figure 6.2 shows the development of AMSR-E soil moisture (upper panels) and CPP-PP daytime precipitation, both averaged over 2005 and 2006 at the beginning (May) and end (September) of the WAM. During both months, soil moisture decreases from south to north. However, the soil moisture gradient becomes less pronounced as a result of increased precipitation over the dry areas throughout the monsoon, as can be seen from the smoother patterns for September than for May. In May, the median and Q67 soil moisture values within the study area are 0.15 and 0.26 $m^3\ m^{-3}$, respectively, while for September these values are 0.27 and 0.23 $m^3\ m^{-3}$.

The averaged daytime precipitation (7:30–16:15 UTC) shows the northward excursion of the convective systems between the beginning and end of the monsoon. In May, the average precipitation is < 1.5 mm $d^{-1}$ over the entire study area, except for the enhanced precipitation near the Jos Plateau (~9°N, 8°E). In September, especially west of 5°E daytime precipitation amounts have increased to 2–3 mm $d^{-1}$ relative to May.

The daytime diurnal cycle of precipitation occurrence and intensity sampled during May–September 2005 and 2006 are shown in Figure 6.3 for dry, wet, and all surfaces. Over all surfaces, the occurrence frequency is lower than 2% during the morning hours (07:30–12:00 UTC), after which the occurrence frequency increases from about 12:00 UTC onwards. The increase over dry surfaces is significantly different from a statistical perspective than over wet and all surfaces from 13:00 UTC onwards. At 16:00 UTC the precipitation occurrence frequency over dry surfaces is about 3% higher than over wet surfaces.

The median precipitation intensity over wet surfaces shows a similar pattern as over all surfaces, with values of 0.13 mm $h^{-1}$ until 11:00 UTC, followed by a steady increase to about 0.4 mm $h^{-1}$ at 16:00 UTC. Over dry surfaces, precipitation intensity is slightly lower than over wet surfaces during the morning hours (0.08–0.10 mm $h^{-1}$), but increases more rapidly (from 0.1 at 11:00 UTC to 0.52 mm $h^{-1}$ at 16:00 UTC) during the afternoon. However, the difference between dry and wet surface median precipitation intensity is not significant at the 0.05 significance level using a Kolmogorov-Smirnov test.

Figure 6.4 shows the cumulative distribution function (CDF) of the soil moisture anomalies and the afternoon (at 16:00 UTC) precipitation occurrence frequency and intensity as function of this CDF. More than half (60%) of the anomalies have values within +/-0.03 $m^3\ m^{-3}$. As already shown in Figure 6.3, convection is more frequent over dry than over wet surfaces. In addition, precipitation occurrence frequency over surfaces with less sharp soil moisture gradients (represented by the intermediate CDF deciles) in the 2°×2° boxes is lower, a feature that can also be deduced from Figure 6.3. However, the higher occurrence frequency does not imply a larger precipitation intensity, as follows from the right panel of Figure 6.4; the median

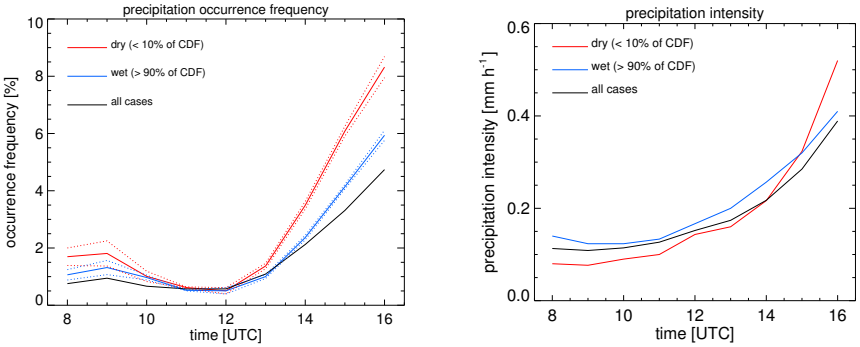


**Figure 6.3** *(Left panel) Daytime diurnal cycle of precipitation occurrence frequency for May–September 2005 and 2006 over dry (red line), wet (blue line), and all surfaces (black line). The dotted lines for dry and wet surfaces denote the occurrence frequencies obtained using a soil moisture anomaly deviating +/- 5% from the standard 10% (for dry surfaces) and 90% (for wet surfaces). (Right panel) Median daytime precipitation intensity over dry, wet, and all surfaces.*

precipitation intensity decreases from 0.52 mm $h^{-1}$ in the first decile to 0.35 mm $h^{-1}$ in the sixth decile, followed by a gradual increase to 0.41 mm $h^{-1}$ in the last decile.

## 6.4 Discussion and conclusions

This Chapter aimed at answering the question if the precipitation occurrence frequency and intensity over dry surfaces differ significantly from over wet surfaces. We have addressed this question by investigating the relation between CPP-PP-retrieved precipitation occurrence and intensity and preceeding (6–15 hours earlier) AMSR-E-observed soil moisture anomalies over West Africa. Over both dry and wet surfaces, a distinct increase in occurrence frequency to-

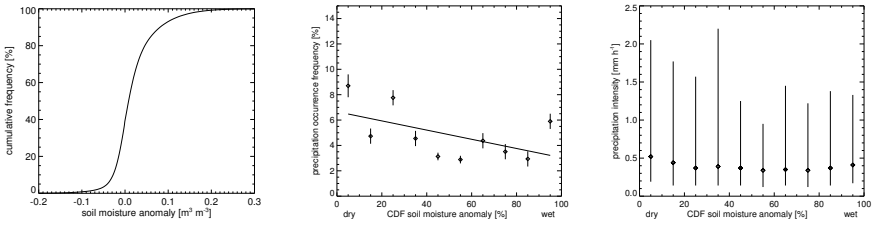


**Figure 6.4** *(Left panel) Cumulative distribution function of AMSR-E soil moisture anomalies for May–Sep 2005–2006. See text for details on the anomaly calculations. (Center panel) Afternoon (16:00 UTC) precipitation occurrence frequency as function of the soil moisture anomaly cumulative distribution function with error bars denoting the standard deviation within each decile. The thin solid line indicates a linear regression. (Right panel) Afternoon precipitation intensity as function of the soil moisture anomaly CDF, with error bars indicating the Q67 within each decile.*

wards the afternoon is seen. The occurrence frequency over dry surfaces becomes significantly different from its wet surface counterpart after about 13:00 UTC. For precipitation intensity, no significant difference between dry and wet surfaces has been found.

The results presented in this research are in line with those of Taylor and Ellis (2006) and Taylor et al. (2011), who showed that the probability of convective initiation over the driest anomalies is about one third larger than over the wettest anomalies. However, our results contrast with those of Findell and Eltahir (1997) and Findell et al. (2011), which suggest that wet surfaces are more favorable for the onset of convection. Part of these differences might originate from the fact that the studies of Findell and Eltahir (1997) and Findell et al. (2011) were performed in more humid climate zones (Southeastern and Midwest US), while this study was carried out over a semi-arid climate region. In the latter study, it was pointed out that afternoon convective triggering increases sharply when the evaporative fraction (the ratio between latent and total heat flux) exceeds 0.7. However, this may only partly apply to the investigated Western African area, because high evaporative fractions are generally only found over the densely vegetated areas. The insignificant difference between dry and wet soil moisture anomalies and subsequent precipitation intensity was also shown in a study conducted in a midlatitude climate region by Alfieri et al. (2008). They demonstrated that both convective and stratiform precipitation intensity is virtually uncorrelated with the preceeding soil moisture.

Because our dataset comprises both beginning and mature convection, it is suggested that the precipitation intensity of maturing convective cells becomes to a lesser extent influenced by soil moisture and becomes more dependent on atmospheric constraints, such as stability, vertical wind shear, and low-level moisture convergence. In addition, the soil moisture influence on moving convective cells might be horizontally decoupled, so that precipitation intensity is affected at a downwind location. However, this horizontal displacement might not be larger than a few kilometres (Clark et al. 2003). Finally, it has been demonstrated that AMSR-E soil moisture and SEVIRI precipitation observations are well-suited to extend the research on the soil moisture–precipitation interaction on the mesoscale, which will contribute to a better understanding of the complex interplay between land surface characteristics and convective precipitation in the tropics.

The study presented does not provide the entire view on the influence of soil moisture on the occurrence and intensity of precipitation. First, no indication on the soil moisture–precipitation relation during the evening and night can be given, because the CPP-PP retrievals are restricted to daytime only. The studies of Taylor et al. (2011) and Taylor and Ellis (2006) provide additional overviews on the convective behavior related to soil moisture during the evening hours. In addition, no distinction between convection that *initiated* over wet and dry surfaces and *mature* convection initiated at upwind directions that moved over dry or wet surfaces has been made. To do so, a sophisticated convective cell tracking algorithm would be required in order to trace individual thunderstorms back to their point of origin [see for example the studies of Mathon et al. (2002), Roca et al. (2010), and Taylor et al. (2011)]. Finally, care should be taken in using the AMSR-E soil moisture retrievals. Although AMSR-E soil moisture retrievals compare well against in situ observations and their horizontal sampling resolution is appropriate for

investigating the soil moisture–precipitation relation at the mesoscale, the temporal sampling is rather limited and necessitates the assumption of stationary soil moisture between consecutive overpasses. As a result, the calculated soil moisture differences might not only be affected through precipitation in between overpasses, which was largely filtered out, but also through the drying of wet surfaces. Recently, Pellarin et al. (2009) showed the possibility of interpolating AMSR-E soil moisture retrievals to 30 minutes using a satellite-based precipitation product and a microwave emission model.

A final note on the AMSR-E soil moisture retrievals is that their quality may decrease during the course of the West African Monsoon. This may especially occur over the semi-arid region in West Africa, because vegetation growth and hence the increase in vegetation optical depth during the monsoon is large in this region (Zribi et al. 2009). Space-based observations of soil moisture are continued by the dedicated Soil Moisture and Ocean Salinity [SMOS, Barre et al. (2008); Kerr et al. (2001)] and the future Soil Moisture Active and Passive [SMAP, Entekhabi et al. (2008)] missions.

# Chapter 7

## Perspectives

This thesis has highlighted the retrieval, evaluation, and application of cloud physical property datasets obtained from SEVIRI-observed visible and near-infrared reflectances. In this Chapter, first the main findings of this thesis are summarized in short, followed by a survey of possible and intended improvements to the CPP algorithm. Finally, some current and future applications of the cloud physical properties and precipitation datasets are highlighted.

The research questions that were addressed in this thesis were as follows:

1) Is the CPP cloud-phase retrieval of sufficient accuracy and precision to construct reliable long-term cloud-phase climatologies for midlatitude coastal climates (Chapter 3)?

2) What is the impact of different horizontal resolutions to the retrieval of cloud particle effective radius and cloud phase using CPP (Chapter 4)?

3) Is the accuracy of precipitation occurrence frequency and precipitation intensity as retrieved from CPP sufficient to monitor the seasonal monsoon progression and the rainfall dynamics at sub-daily scale over West Africa (Chapter 5)?

4) Is there a significant difference in the precipitation occurrence frequency and intensity over wet and dry surfaces during the West African Monsoon (Chapter 6)?

Chapter 3 presented the evaluation of one year of cloud-phase retrievals with ground-based cloud radar and lidar observations at Cabauw, The Netherlands. It was shown that the CPP cloud-phase retrieval algorithm has sufficient accuracy (<5%) and precision (<10%) for climate monitoring purposes. During winter, the usage of 0.6-$\mu$m and 1.6-$\mu$m reflectances has added value over cloud-phase determination using temperature thresholding, which tend to misclassify supercooled water in stratiform clouds. During summer, the increase and decrease in the amount of ice clouds resulting from convection between morning and late afternoon can be well followed.

In Chapter 4, the question to what extent varying horizontal resolutions affect the cloud particle effective radius and cloud-phase retrievals in case of broken clouds and inhomogeneous overcast clouds was addressed. It was shown from CPP retrievals on MODIS reflectances that at the lowest cloud fractions the low-resolution $r_e$ over ocean surfaces is overestimated by up to 5 $\mu$m compared to at high resolution, due to the relatively large contribution of the underlying surface to the observed 1.6-$\mu$m reflectances. In about 4% of the cases, this leads to a misclassification of 'water' clouds into 'ice'. However, the additional cloud-top temperature check in the cloud-phase retrieval algorithm reduces these misclassifications to 2%.

CPP-PP precipitation retrievals were evaluated over West Africa with TRMM-PR and CMORPH observations in Chapter 5. The precipitation occurrence frequency from CPP-PP agrees well with TRMM-PR-observed values, with a correlation coefficient of 0.86. CPP-PP-obtained instantaneous precipitation intensities agree to a lesser extent (corr=0.50), but given the different observation techniques (passive satellite imagery versus active radar observations) the agreement is satisfactory. Investigation of the rainfall frequency distributions from CPP-PP revealed good agreement with TRMM-PR and rain gauge observations, although in the range 5–16 mm $h^{-1}$ CPP-PP overestimates relative to the rain gauges. Further, it was demonstrated that CPP-PP is suitable to monitor both the seasonal and diurnal cycle during daytime of precipitation throughout the West African Monsoon. Owing mainly to its high spatial and temporal resolution, CPP-PP detects a larger dynamical range in the diurnal cycle during daytime of precipitation intensity than CMORPH.

Chapter 6 presented a study on the relation between soil moisture and the precipitation occurrence frequency and intensity during the West African Monsoon seasons of 2005 and 2006. Based on spatial soil moisture anomalies calculated from AMSR-E retrievals, dry soils were discriminated from wet soils. It followed that the precipitation occurrence frequency over dry soils becomes significantly higher than over wet soils during the afternoon, but that precipitation intensity over dry soils is not significantly different. It was suggested that for well-developed convective cells the soil moisture forcings become less important compared to other (atmospheric) forcings. The study demonstrated that the combination of satellite-based soil moisture and precipitation observations can be helpful in improving the understanding of the land surface–precipitation interaction over tropical areas.

## 7.1 Algorithm improvements

This thesis showed that accurate cloud physical and precipitation properties can be retrieved using the CPP algorithm. However, it was also indicated that under certain circumstances the accuracy of the retrievals decreases. Therefore a number of improvements and extensions for the retrieval of cloud phase, cloud particles effective radius, and precipitation properties are proposed below.

### *Cloud phase*

The cloud-phase retrieval algorithm currently uses the SEVIRI 0.6- and 1.6-$\mu$m channel reflectances. As a consequence, the algorithm can only be applied during daytime.

As was shown in Chapter 3, the cloud phase retrieved using CPP can be properly used to study the daytime growth of convection. However, study on the entire diurnal cycle of cloud phase requires usage of the thermal infrared channel brightness temperatures. One such cloud-phase retrieval algorithm, which was adapted for use on SEVIRI data is the MODIS infrared cloud-phase retrieval algorithm (Baum et al. 2000; Strabala et al. 1994). It applies a similar physical principle (different absorption characteristics between water droplets and ice crystals) as CPP to derive cloud phase and may be suitable to complement the CPP daytime cloud-phase retrievals. In order to enable a smooth transition from the daytime visible/near-infrared CPP to the nighttime MODIS infrared cloud-phase retrievals the differences between retrievals from the two algorithms obtained during daytime will be investigated.

*Cloud particle effective radius*

The $r_e$ retrieval may be improved by using spectral channels that are further located in the near-infrared spectral region, where solar radiation is more efficiently absorbed by cloud particles. As a result, the influence of the underlying surface to the measured reflectance in case of semi-transparent clouds diminishes. Therefore retrievals for these cloud cases might be carried out using the SEVIRI 3.9 $\mu$m spectral channel. However, for retrieving ice cloud $r_e$ the 3.9 $\mu$m spectral channel is less suitable, due to among others a limited sensitivity of $r_e$ to the 3.9-$\mu$m reflectance for large ice crystals. The Flexible Combined Imager (FCI) onboard the Meteosat Third Generation (MTG) satellites (to be launched from 2017 onwards) will carry a 2.2 $\mu$m spectral channel, which will enable $r_e$ retrievals that are more representative for the cloud top (Platnick et al. 2001). In addition, using the three near-infrared channels (1.6 $\mu$m, 2.2 $\mu$m, and 3.9 $\mu$m) research on the vertical $r_e$ profile for optically thin clouds could be performed (Chang 2003; Chang and Li 2002).

Another potential for improvement of the $r_e$ retrieval will be the correction of 1.6-$\mu$m reflectances with the observed High-Resolution Visible (HRV) channel reflectance in case of broken or inhomogeneous clouds. Although the HRV spectral channel range is rather broad (0.4-1.1 $\mu$m), Deneke and Roebeling (2010) demonstrated for the 0.6-$\mu$m and 0.8-$\mu$m channels that the observed reflectance at the operational resolution ($3\times3$ km$^2$ at nadir) can be downscaled to the HRV resolution using the HRV-observed reflectance. This downscaling could also be applied to other SEVIRI shortwave channels.

A final improvement of the $r_e$ retrievals may be achieved by using optimal estimation techniques. In optimal estimation, the basic principle is to maximize the probability of the retrieved cloud properties conditional on the value of the measurement and any a priori information on the observed clouds. It might be particularly useful to improve the $r_e$ retrievals for optically thin clouds, because the existing ambiguities in the retrieval will be solved for. Optimal estimation on SEVIRI data has been proven useful for surface reflectance and aerosol retrievals (Govaerts et al. 2010), sea surface temperature (Merchant et al. 2009), and combined aerosol and cloud retrievals (Thomas et al. 2007). A constraint of optimal estimation is the large calculation time that is required, which makes it less suitable to be implemented in a near-realtime processing environment.

### Precipitation properties

As the precipitation properties are derived from cloud-phase and implicit $r_e$ information (through the CWP), the retrieved precipitation properties will benefit from the future improvements of the cloud-phase and $r_e$ retrievals. Further, it is intended to add a below-cloud evaporation correction to the current algorithm. To do so, information on the relative humidity in the lowest 2 km of the atmosphere is required, because the cloud base is mostly located below this level, as is the majority of the total atmospheric water vapor burden. Because the below-cloud relative humidity can change rapidly in both time and space (for example due to air mass changes within synoptical weather systems), the water vapor information needs to be as actual as possible.

A water vapor dataset that could potentially be used has been developed within the Water Cycle Multi Mission Observation Strategy project [WACMOS, Su et al. (2010)]. Water vapor datasets for three layers (200–500 hPa, 500–850 hPa, and 850 hPa–surface) are produced from a combination of water vapor observations from SEVIRI and the Infrared Atmospheric Sounding Interferometer (IASI) onboard MetOp. The information is provided at a spatial and temporal resolution of $0.25° \times 0.25°$ and 3 h, respectively. As an alternative to satellite water vapor datasets, Numerical Weather Prediction (NWP) model analyses on temperature and humidity might be incorporated. Although these data are available only 4 times per day, it provides detailed information on the vertical profiles of temperature and humidity, which results in a more accurate cloud base and below-cloud evaporation estimate.

The dependency of the precipitation properties retrievals to cloud physical properties retrievals implies the restriction to daytime SEVIRI data only. Continuous precipitation information enables profound research on the full diurnal cycle of precipitation mechanisms, but this can only be achieved when using the thermal infrared and water vapor absorption channels. For example, Thies et al. (2008) developed a rainfall retrieval algorithm that uses CWP and cloud-phase information from the SEVIRI visible and near-infrared channels during daytime, while cloud phase and CWP are retrieved from various brightness temperature differences during nighttime.

## 7.2 Applications

The high temporal and spatial resolution of the SEVIRI-based cloud physical and precipitation properties datasets opens various possibilities for their application in atmospheric research. One possible application was already highlighted in Chapter 6. Additional to this land surface–precipitation study, other potential applications of the cloud physical and precipitation properties datasets are:

• **Climate monitoring**
Monitoring the atmosphere from space with respect to climate change has been recognized by the Global Climate Observation System (GCOS) of the World Meteorological Organization (WMO). In order to guarantee continuous and accurate observations, a list of Essential Climate

Variables (ECVs), comprising among others atmospheric upper-air temperature, cloud cover, cloud-top temperature, and precipitation was established. Prior to the generation of sustained long-term and reprocessed Thematic Climate Data Records (TCDRs), the radiances measured by the various satellite instruments need to be intercalibrated to the highest possible accuracy to avoid artificial trends resulting from orbital drifts or degrading calibration performance. This calibration effort is coordinated by the Global Space-based Inter-Calibration System [GSICS, Goldberg et al. (2011)]. Recently, within the Climate Monitoring Satellite Application Facility (CM-SAF) the first reprocessed cloud physical property datasets based on recalibrated AVHRR data from 1981 onwards have been completed and a similar reprocessing effort will be carried out for the Meteosat First and Second Generation satellites (1981–present).

**• Weather forecasting**

The potential of SEVIRI is to track and follow developing convective cells using its very high spatial and temporal resolution (Carbajal Henken et al. 2011; Zinner et al. 2008). Precipitation retrievals can be a useful tool for meteorologists to get an indication on the intensity of approaching precipitation as an augment to rain radar information. In addition, SEVIRI precipitation datasets in combination with satellite soil moisture datasets might serve as input for a surface runoff system, although satellite precipitation retrieval algorithms tend to overestimate precipitation intensities compared to ground-based observations and hence would overestimate the surface runoff (Tian et al. 2007). These potential nowcasting applications can be further exploited with the launch of the FCI onboard the MTG satellites, which will enable monitoring of convective cells every 10 minutes (for Europe and Africa) and even every 2.5 minutes when in Rapid Scan Service (Europe only).

In addition to nowcasting applications, measured SEVIRI thermal infrared radiances are increasingly assimilated as additional observations into global or regional NWP models [see for example Andersson et al. (2005), Szyndel et al. (2005), Stengel et al. (2009), and Bauer et al. (2011)] using four-dimensional variational analysis (4D-Var) schemes. Also the derived and validated cloud physical property and precipitation datasets from SEVIRI might be of added value for improving the NWP predictions, taking advantage of SEVIRI's high spatial and temporal sampling resolution.

**• Feedback studies**

Beside the study on the soil moisture–precipitation relation presented in Chapter 6, cloud property and precipitation datasets may be applied for other process studies, such as water cycle closure. From the retrieved cloud optical thickness and auxilary water vapor and aerosol datasets the transmission and hence the surface solar irradiance is calculated with an accuracy of about 3 W $m^{-2}$ (Deneke et al. 2008). The surface solar irradiance can in turn be used as input for surface energy balance models [such as the Surface Energy Balance System (SEBS), Su (2002)]. The synergistic use of observations from different satellite platforms to obtain an accurate estimate of the various water cycle components is investigated in the WACMOS project. In order to obtain reliable estimates of water cycle closure, it is required that internal consistency between the separate water cycle components is conserved. For example, soil moisture observations should show an increase after a precipitation event, which in turn should lead into an increase in model-predicted evaporation.

**• Climate model evaluation**

As a result of the rather large intermodel spread in climate model predictions of the temperature increase, which is partly caused by uncertainties in cloud feedback [Randall et al. in Solomon et al. (2007)], satellite-derived cloud property datasets are a useful tool for the evaluation of cloud parameterizations of these models. The cloud physical properties derived from SEVIRI-observed reflectances are especially beneficial for evaluating the physical processes that occur at sub-daily scales, such as the growth and decline of convection. Evaluations of the Regional Atmospheric Climate Model (RACMO) cloud scheme using CPP-derived cloud properties (CWP, precipitation, cloud phase, and cloud height) have been performed for West Africa (Greuell et al. 2011) and Europe (Roebeling and van Meijgaard 2009) and provided valuable information for the climate model community. Other climate model cloud scheme evaluations have been carried out using CALIPSO (Chepfer et al. 2008) and ISCCP cloud datasets (Lin and Zhang 2004). It is expected that the increment of the SEVIRI cloud datasets combined with the intended CPP algorithm improvements will extend the possibilities for the climate model community to evaluate their models. It is noted that special attention should be paid to adequately match the horizontal resolutions of the climate model and the cloud physical and precipitation properties datasets, as well as to correct for the different vertical representation of clouds between the model and the satellite observation datasets.

## Summary

Clouds play an important role in the Earth's radiation and hydrological balance. In the shortwave spectrum, incident sunlight is primarily reflected by clouds, thereby resulting in a cooling effect, while in the longwave spectrum outgoing radiation from the Earth's surface is absorbed and re-emitted, which results in a warming effect. Further, clouds redistribute water and latent heat at both the horizontal and vertical scale. In order to accurately assess whether the properties of clouds and precipitation change in a changing climate, accurate measurements at high resolutions in space and time are required. However, large parts of the world remain undersampled with respect to ground-based observations of these properties. The current generation of geostationary weather satellites is well-suited to monitor clouds and precipitation, and retrieve their properties accurately. Further, accurate cloud and precipitation datasets can be used for evaluating cloud and precipitation parameterizations in weather and climate models, to investigate land–atmosphere interactions, and to detect changes in the diurnal cycle of clouds and precipitation.

This thesis describes research performed to retrieve and validate cloud thermodynamic phase, cloud particle effective radius, and precipitation occurrence and precipitation intensity. Further, an application of these retrievals to evaluate the feedback mechanism between precipitation and soil moisture is presented. The properties of clouds and precipitation are retrieved by the Cloud Physical Properties (CPP) algorithm that uses visible (0.6 $\mu$m) and near-infrared (1.6 $\mu$m) reflectances observed by the Spinning Enhanced Visible and Infrared Imager (SEVIRI) on the Meteosat Second Generation (MSG) satellites. These reflectances are measured at a temporal resolution of 15 minutes and a spatial resolution that varies between $3\times3$ km$^2$ over Central Africa and $4\times7$ km$^2$ over Western Europe. Such a high temporal and spatial resolution enables e.g. research on diurnal developments of cloud and precipitation properties.

In Chapter 1, a general introduction on climate change and the influence clouds have on the climate is given. Several feedback mechanisms in the climate system, such as the impact of a temperature increase on clouds and atmospheric water vapor are explained. Further, the importance of clouds to the hydrological cycle is highlighted. Finally, the research questions that are answered in this thesis are addressed.

In Chapter 2, the theoretical basis for the research performed in thesis, as well as the methodologies that are used, are presented. First, the theory of radiative transfer, applied to the the Earth's atmosphere and clouds, is explained, followed by a short survey on some radiative transfer models. Further, the various satellite instruments from which data are used in this thesis are highlighted, after which the Chapter concludes with a detailed explanation of the CPP algorithm, that is used to obtain the cloud and precipitation properties from the measured reflectances observed by SEVIRI.

In Chapter 3, three cloud phase retrieval algorithms are evaluated to assess their applicability for climate monitoring purposes in mid-latitude coastal climate zones i.e., the CM-SAF method, the MODIS-like method and the ISCCP-like method. Using one year of data from SEVIRI on Meteosat-8, retrievals of the methods are compared to collocated and synchronized ground-based cloud-phase retrievals obtained from cloud radar and lidar observations at Cabauw, the Netherlands. Three aspects of the satellite retrievals are evaluated: 1) Instantaneous cloud-phase retrievals, 2) monthly averaged water and ice cloud occurrence frequency, and 3) daytime diurnal cycle of cloud phase. The results reveal for the instantaneous cases, that all methods show a very small bias for thick water and ice cloud retrievals (~5%). The ISCCP-like method has a larger bias for pure water clouds (~10%), which is likely due to the 260 K threshold leading to misdetection of water clouds existing at lower temperatures. For the monthly averaged water and ice cloud occurrence, the CM-SAF method is best capable of reproducing the annual cycle, mainly for the water cloud occurrence frequency, for which an almost constant positive bias of ~8% was found. The ISCCP- and MODIS-like methods are less capable to detect the annual cycle, especially due to retrieval inaccuracies during the winter months. The difference in annual cycle detection between the three methods is most probably related to the use of visible/near-infrared reflectances, which enable a more physically based observation of cloud phase than the MODIS-like and ISCCP-like methods that use infrared radiances. The daytime diurnal cycle of cloud phase is well reproduced by all methods. The MODIS-like method reproduces the daytime diurnal cycle best, with correlations of 0.89 and 0.86 for water and ice cloud occurrence frequency, respectively.

In Chapter 4, the impact of satellite sensor resolution on the retrievals of cloud particle effective radius ($r_e$) and cloud phase is investigated for broken and overcast inhomogeneous clouds, using the CPP retrieval algorithm. First, synthetic datasets of high-resolution (1×1 km$^2$) and low-resolution (3×3 km$^2$) radiances are used to evaluate the effect of these clouds on the retrieval of $r_e$ and Cloud-Top Temperature ($T_c$), the cloud properties that are used for cloud-phase retrievals. It is shown that for thick broken and inhomogeneous overcast water clouds over ocean and land surfaces low-resolution $r_e$ retrievals can be up to 12 $\mu$m higher and $T_c$ retrievals up to 20 K higher than the corresponding high-resolution retrievals. The overestimation of $r_e$ may cause erroneous assignments of 'ice' to water clouds. Second, CPP retrievals on Moderate-Resolution Imaging Spectroradiometer (MODIS) reflectances are used to quantify the effect of broken and overcast inhomogeneous clouds on $r_e$ and CPH retrievals over the Atlantic Ocean and Central Europe. Over both areas, the low-resolution $r_e$ is overestimated by up to 5 $\mu$m for broken and up to 2 $\mu$m for inhomogeneous overcast clouds. At low resolution, the fraction of water clouds is underestimated by 2.3% over the Atlantic Ocean and 0.6% over Central Europe. The increase of $T_c$ partly compensates for the increase in $r_e$, in the CPH

retrievals at low resolution. If no $T_c$ information were used, the underestimation of the water cloud fraction would be 3.5% and 2.2% for the Atlantic Ocean and Central Europe, respectively. For inhomogeneous overcast clouds integrated over all inhomogeneity classes, this difference is -1.3% and -2.3% for Central Europe and Atlantic Ocean, respectively. The results indicate that the retrieval of $r_e$ in the CPP algorithm is sensitive to satellite sensor resolution in case of broken clouds and inhomogeneous overcast clouds, but that despite the large $r_e$ sensitivity the CPH retrieval is much less sensitive to sensor resolution.

Chapter 5 presents the evaluation of the CPP-PP algorithm over West Africa. This algorithm combines CWP, CPH, $r_e$, and $T_c$ retrievals from visible, near-infrared and thermal infrared observations of SEVIRI to retrieve precipitation occurrence frequency and precipitation intensity. It is investigated whether the CPP-PP algorithm is capable to retrieve these precipitation properties with sufficient accuracy over West Africa, using TRMM-PR observations as reference. Further, it is assessed whether CPP-PP is capable of monitoring the seasonal evolution and variations in the daytime cycle of precipitation during the monsoon, using the Climate Prediction Center Morphing Technique (CMORPH) precipitation observations. The results show that the SEVIRI-detected precipitation area agrees well with TRMM-PR, with the area detected by CPP-PP being ~10% larger than observed by TRMM-PR. The mean retrieved precipitation intensity from CPP-PP is about 8% higher than from TRMM-PR. Examination of the TRMM-PR and CPP-PP cumulative frequency distributions reveal that differences between CPP-PP and TRMM-PR are generally within +/-10%. Relative to rain gauge observations, CPP-PP shows very good agreement up to rain intensities of ~5 mm $h^{-1}$. However, at moderate precipitation intensities (5–16 mm $h^{-1}$) CPP-PP overestimates compared to the rain gauges. Further, it was shown that both the accumulated precipitation and the seasonal progression of precipitation throughout the monsoon is in good agreement with CMORPH, although CPP-PP retrieves higher amounts in the coastal region. Using latitudinal Hovmöller diagrams, a fair correspondence between CPP-PP and CMORPH was found, which is reflected by high correlation coefficients (≈0.7) for both precipitation intensity and precipitation occurrence frequency. The daytime cycle of precipitation from CPP-PP shows different patterns for three regions in West Africa throughout the monsoon, with a decrease in dynamical range of precipitation near the major monsoon rains. The dynamical range as retrieved from CPP-PP is larger than that from CMORPH. This might result from both the better spatio-temporal resolution of SEVIRI, as well as from thermal infrared radiances being partly used by CMORPH, which smooth the daytime precipitation signal.

Chapter 6 describes a study on the relation between soil moisture and convective precipitation over West Africa, using soil moisture retrievals from Advanced Microwave Scanning Radiometer EOS (AMSR-E) brightness temperatures and daytime (7:30–16:15 UTC) precipitation retrievals obtained from SEVIRI-observed visible and near-infrared reflectances. For the 2005 and 2006 monsoon seasons, soil moisture anomalies from the AMSR-E dataset were calculated in 2°×2° blocks. Using the lowest and highest 10% of the soil moisture anomalies distribution to represent dry and wet soils, respectively, the SEVIRI-based precipitation occurrence frequency and precipitation intensity over these soils at the following day were calculated. It was found that over both dry and wet soils the precipitation occurrence frequency increases during the afternoon, with a stronger increase over dry soils than over wet soils after 13:00

UTC. For precipitation intensity no significant difference between the dry and wet soils could be discerned, as the difference between wet-soil and dry-soil precipitation intensity is mostly $< 0.1$ mm $h^{-1}$. This research has demonstrated the potential of satellite-based soil moisture and precipitation datasets for improving the understanding of the soil moisture–precipitation interactions.

Finally, in Chapter 7 some potential improvements to the CPP algorithm as well as future research applications of the retrieved satellite cloud and precipitation datasets are discussed. The suggested improvements for the CPP algorithm comprise a nighttime algorithm for the cloud-phase and precipitation properties, which would enable research on the entire diurnal cycle of these quantities. Further, more research on correcting retrieved cloud physical properties for partly cloud-filled pixels is suggested using the SEVIRI High-Resolution Visible spectral channel. Applications of the cloud and precipitation properties datasets exist in among others climate monitoring, weather forecasting, water balance studies, land surface–atmosphere interactions, and assimilation in weather and climate models. These applications can take full advantage of the high spatial and temporal sampling of SEVIRI.

# Bibliography


Adler, R. F. and A. J. Negri, 1988: Satellite infrared technique to estimate tropical convective and stratiform rainfall. *J. Appl. Meteorol.*, **27**, 30–71, doi:10.1175/1520-0450(1988)027<0030:ASITTE>2.0.CO;2.

Albrecht, B. A., 1989: Aerosols, Cloud Microphysics, and Fractional Cloudiness. *Science*, **245**, 1227–1230, doi:10.1126/science.245.4923.1227.

Alfieri, L., P. Claps, P. D'Odorico, F. Laio, and T. M. Over, 2008: An Analysis of the Soil Moisture Feedback on Convective and Stratiform Precipitation. *J. Hydrometeorol.*, **9**, 280–291, doi:10.1175/2007JHM863.1.

Ali, A., T. Lebel, and A. Amani, 2005: Rainfall Estimation in the Sahel. Part I: Error Function. *J. Atmos. Sci.*, **44**, 1691–1706, doi: 10.1175/JAM2304.1.

Allan, R. P. and B. J. Soden, 2008: Atmospheric Warming and the Amplification of Precipitation Extremes. *Science*, **321**, 1481–1484, doi:10.1126/science.1160787.

Alonge, C. J., K. I. Mohr, and W.-K. Tao, 2007: Numerical studies of wet versus dry soil regimes in the West African Sahel. *J. Hydrometeorol.*, **8**, 102–116, doi:10.1175/JHM559.1.

Andersson, E., P. Bauer, A. Beljaars, F. Chevallier, E. Hólm, M. Janisková, P. Kållberg, G. Kelly, P. Lopez, A. McNally, E. Moreau, A. J. Simmons, J.-N. Thépaut, and A. M. Tompkins, 2005: Assimilation and Modeling of the Atmospheric Hydrological Cycle in the ECMWF Forecasting System. *B. Am. Meteorol. Soc.*, **86**, 387–402, doi:10.1175/BAMS-86-3-387.

Arkin, P. A. and B. N. Meisner, 1987: The relationship between large scale convective rainfall and cold cloud over the western hemisphere during 1982–1984. *Mon. Wea. Rev.*, **115**, 51–74, doi:10.1175/1520-0493(1987)115<0051:TRBLSC>2.0.CO;2.

Arkin, P. A., T. M. Smith, M. R. P. Sapiano, and J. Janowiak, 2010: The observed sensitivity of the global hydrological cycle to changes in surface temperature. *Environ. Res. Lett.*, **5**, 35201–35206, doi:10.1088/1748-9326/5/3/035201.

Arkin, P. A. and P. Xie, 1994: The Global Precipitation Climatology Project: First Al-

gorithm Intercomparison Project. *B. Am. Meteorol. Soc.*, **75**, 401–420, doi:10.1175/1520-0477(1994)075<0401:TGPCPF>2.0.CO;2.

Arking, A., 1991: The Radiative Effects of Clouds and their Impact on Climate. *B. Am. Meteorol. Soc.*, **72**, 795–813, doi:10.1175/1520-0477(1991)072<0795:TREOCA>2.0.CO;2.

Arking, A. and J. D. Childs, 1985: Retrieval of cloud cover parameters from multispectral satellite images. *J. Clim. Appl. Meteor.*, **24**, 322–333, doi:10.1175/1520-0450(1985)024<0322:ROCCPF>2.0.CO;2.

Arrhenius, S., 1896: On the influence of carbonic acid in the air upon the temperature of the ground. *Philos. Mag.*, **41**, 237–275.

Ba, M. B. and A. Gruber, 2001: GOES Multispectral Rainfall Algorithm (GMSRA). *J. Appl. Meteorol.*, **40**, 1500–1514, doi:10.1175/1520-0450(2001)040<1500:GMRAG>2.0.CO;2.

Barker, H. W. and D. Liu, 1995: Inferring optical depth of broken clouds from Landsat data. *J. Climate*, **8**, 2620–2630, doi:10.1175/1520-0442(1995)008<2620:IODOBC>2.0.CO;2.

Barre, H. M. J. P., B. Duesmann, and Y. H. Kerr, 2008: SMOS: The Mission and the System. *IEEE T. Geosci. Remote*, **46**, 587–593, doi:10.1109/TGRS.2008.916264.

Bartalis, Z., W. Wagner, V. Naeimi, S. Hasenauer, K. Scipal, H. Bonekamp, J. Figa, and C. Anderson, 2007: Initial soil moisture retrievals from the METOP-A Advanced Scatterometer (ASCAT). *Geophys. Res. Lett.*, **34**, doi:10.1029/2007GL031088.

Basu, B. K., 2007: Diurnal variation in precipitation over India during the summer monsoon season: observed and model predicted. *Mon. Wea. Rev.*, **135**, 2155–2167, doi:10.1175/MWR3355.1.

Bauer, P., T. Auligné, W. Bell, A. Geer, V. Guidard, S. Heilliette, M. Kazumori, M.-J. Kim, E. H.-C. Liu, A. P. McNally, B. Macpherson, K. Okamoto, R. Renshaw, and L.-P. Riishøjgaard, 2011: Satellite cloud and precipitation assimilation at operational NWP centres. *Q. J. Roy. Meteor. Soc.*, doi:10.1002/qj.905.

Baum, B. A., R. A. Frey, G. G. Mace, M. K. Harkey, and P. Yang, 2003: Nighttime multilayered cloud detection using MODIS and ARM data. *J. Appl. Meteorol.*, **42**, 905–919, doi:10.1175/1520-0450(2003)042<0905:NMCDUM>2.0.CO;2.

Baum, B. A., P. F. Soulen, K. I. Strabala, M. D. King, S. A. Ackerman, W. P. Menzel, and P. Yang, 2000: Remote sensing of cloud properties using MODIS Airborne Simulator imagery during SUCCESS: 2. Cloud thermodynamic phase. *J. Geophys. Res.*, **105**, 11781–11792, doi:10.1029/1999JD901090.

Behrangi, A., K.-L. Hsu, B. Imam, S. Sorooshian, G. J. Huffman, and R. J. Kuligowski, 2009: PERSIANN-MSA: A precipitation estimation method from satellite-based multispectral analysis. *J. Hydrometeorol.*, **10**, 1414–1429, doi:10.1175/2009JHM1139.1.

Berk, A., L. S. Bernstein, and D. C. Robertson, 1987: MODTRAN: A moderate resolution model for LOWTRAN. Technical report, Space Science Instrumentation.

Betts, A. K., 2004: Understanding hydrometeorology using global models. *B. Am. Meteorol. Soc.*, **85**, 1673–1688, doi:10.1175/BAMS-85-11-1673.

Cahalan, R. F., W. Ridgway, W. J. Wiscombe, S. Gollmer, and Harshvardhan, 1994: Independent pixel and Monte Carlo estimates of stratocumulus albedo. *J. Atmos. Sci.*, **51**, 3776–3790, doi:10.1175/1520-0469(1994)051<3776:IPAMCE>2.0.CO;2.

Callendar, G. S., 1938: The artificial production of carbon dioxide and its influence on temperature. *Q. J. Roy. Meteor. Soc.*, **64**, 223–240, doi:10.1002/qj.49706427503.

Carbajal Henken, C. K., M. J. Schmeits, H. M. Deneke, and R. A. Roebeling, 2011: Using MSG-SEVIRI Cloud Physical Properties and weather radar observations for the detection of Cb/TCu clouds. *J. Appl. Meteorol. Clim.*, **50**, 1587–1600, doi:10.1175/2010JAMC2601.1.

Chambers, L. H., B. A. Wielicki, and K. F. Evans, 1997a: Accuracy of the independent pixel approximation for satellite estimates of oceanic boundary layer cloud optical depth. *J. Geophys. Res.*, **102**, 1779–1794, doi:10.1175/1520-0469(1997)054<1525:IPATDE>2.0.CO;2.

— 1997b: Independent pixel and two-dimensional estimates of Landsat-derived cloud field albedo. *J. Atmos. Sci.*, **54**, 1525–1532, doi:10.1029/96JD02995.

Chandrasekhar, S., 1960: *Radiative transfer*. New York: Dover, 1960, 393 pp.

Chang, F. L., 2003: Retrieving vertical profiles of water-cloud droplet effective radius: Algorithm modification and preliminary application. *J. Geophys. Res.*, **108**, 4763–4773, doi:10.1029/2003JD003906.

Chang, F. L. and Z. Li, 2002: Estimating the vertical variation of cloud droplet effective radius using multispectral near-infrared satellite measurements. *J. Geophys. Res.*, **107**, 4257–4268, doi:10.1029/2001JD000766.

Chepfer, H., S. Bony, D. Winker, M. Chiriaco, J.-L. Dufresne, and G. Sèze, 2008: Use of CALIPSO lidar observations to evaluate the cloudiness simulated by a climate model. *Geophys. Res. Lett.*, **35**, doi:10.1029/2008GL034207.

Chepfer, H., P. Goloub, J. Spinhirne, P. H. Flamant, M. Lavorato, L. Sauvage, G. Brogniez, and J. Pelon, 2000: Cirrus cloud properties derived from POLDER-1/ADEOS polarized radiances: First validation using a ground-based lidar network. *J. Appl. Meteorol.*, **39**, 154–168, doi:10.1175/1520-0450(2000)039<0154:CCPDFP>2.0.CO;2.

Clark, D. B., C. M. Taylor, A. J. Thorpe, R. J. Harding, and M. E. Nicholls, 2003: The influence of spatial variability of boundary-layer moisture on tropical continental squall lines. *Q. J. Roy. Meteor. Soc.*, **129**, 1101–1121, doi:10.1256/qj.02.122.

Coakley, J. A., M. A. Friedman, and W. R. Tahnk, 2005: Retrieval of cloud properties for partly

cloudy imager pixels. *J. Atmos. Ocean. Technol.*, **22**, 3–17, doi:10.1175/JTECH-1681.1.

Cook, K. H., 1999: Generation of the African Easterly Jet and Its Role in Determining West African Precipitation. *J. Climate*, **12**, 1165–1184, doi:10.1175/1520-0442(1999)012<1165:GOTAEJ>2.0.CO;2.

Dai, A., 2001: Global Precipitation and Thunderstorm Frequencies. Part II: Diurnal Variations. *J. Climate*, **14**, 1112–1128, doi:10.1175/1520-0442(2001)014<1112:GPATFP>2.0.CO;2.

De Haan, J. F., P. B. Bosma, and J. W. Hovenier, 1987: The adding method for multiple scattering calculations of polarized light. *Astron. Astrophys.*, **183**, 371–391.

de Rosnay, P., C. Gruhier, F. Timouk, F. Baup, E. Mougin, P. Hiernaux, L. Kergoat, and V. LeDantec, 2009: Multi-scale soil moisture meausurements at the Gourma meso-scale site in Mali. *J. Hydrol.*, **375**, 241–252, doi:10.1016/j.jhydrol.2009.01.015.

Del Genio, A. D., M. S. Yao, W. Kovari, and K. K. W. Lo, 1996: A prognostic cloud water parameterization for global climate models. *J. Climate*, **9**, 270–304, doi:10.1175/1520-0442(1996)009<0270:APCWPF>2.0.CO;2.

Deneke, H. M., A. J. Feijt, and R. A. Roebeling, 2008: Estimating surface solar irradiance from METEOSAT SEVIRI-derived cloud properties. *Remote Sens. Environ.*, **112**, 3131–3141, doi:10.1016/j.rse.2008.03.012.

Deneke, H. M. and R. A. Roebeling, 2010: Downscaling of METEOSAT SEVIRI 0.6 and 0.8 $\mu$m channel radiances utilizing the high-resolution visible channel. *Atmos. Chem. Phys.*, **10**, 9761–9772, doi:10.5194/acp-10-9761-2010.

Deneke, H. M., R. A. Roebeling, E. L. A. Wolters, A. J. Feijt, and C. Simmer, 2009: On the sensitivity of satellite-derived cloud properties to sensor resolution and broken clouds. *AIP Conf. Proc. 1100*, 376.

Dinku, T., P. Ceccato, E. Grover-Kopec, M. Lemma, S. J. Connor, and C. F. Ropelewski, 2007: Validation of satellite rainfall products over East Africa's complex topography. *Int. J. Remote Sens.*, **28**, 1503–1526, doi:10.1080/01431160600954688.

Diongue, A., J. P. Lafore, and J. L. Redelsperger, 2002: Numerical study of a Sahelian synoptic weather system: Initiation and mature stages of convection and its interactions with the large-scale dynamics. *Q. J. Roy. Meteor. Soc.*, **128**, 1899–1927, doi:10.1256/003590002320603467.

Dirmeyer, P. A., R. D. Koster, and Z. Guo, 2006: Do Global Models Properly Represent the Feedback between Land and Atmosphere? *J. Hydrometeorol.*, 1177–1198, doi:10.1175/JHM532.1.

Doelling, D. R., L. Nguyen, and P. Minnis, 2004: Calibration comparisons between SEVIRI, MODIS and GOES data. *EUMETSAT Meteorol. Sat. Conf.*, 77–83.

Douville, H., F. Chauvin, S. Planton, J. Royer, D. Salas-Mélia, and S. Tyteca, 2002: Sensitivity of

the hydrological cycle to increasing amounts of greenhouse gases and aerosols. *Clim. Dyn.*, **20**, 45–68, doi:10.1007/s00382-002-0259-3.

Downing, H. D. and D. Williams, 1975: Optical constants of water in the infrared. *J. Geophys. Res.*, **80**, 1656–1661, doi:10.1029/JC080i012p01656.

Ebert, E. E., J. E. Janowiak, and C. Kidd, 2007: Comparison of Near-Real-Time Precipitation Estimates from Satellite Observations and Numerical Models. *B. Am. Meteorol. Soc.*, **88**, 47–64, doi:10.1175/BAMS-88-1-47.

Efron, B. and R. J. Tibshirani, 1993: *An introduction to the bootstrap*. CRC Press Online, 436 pp.

Entekhabi, D., T. J. Jackson, E. Njoku, P. O'Neill, and J. Entin, 2008: Soil Moisture Active/-Passive (SMAP) Mission concept. *Society of Photo-Optical Instrumentation Engineers (SPIE) Conference Series*, volume 7085.

EUMETSAT, 2007: A planned change to the MSG Level 1.5 Image Production Radiance Definition. Technical report, EUM/OPS-MSG/TEN/06/0519.

Evans, K. F., 1998: The spherical harmonic discrete ordinate method for three-dimensional atmospheric radiative transfer. *J. Atmos. Sci.*, **55**, 429–446, doi:10.1175/1520-0469(1998)055<0429:TSHDOM>2.0.CO;2.

Ferguson, C. R. and E. F. Wood, 2011: Observed Land–Atmosphere Coupling from Satellite Remote Sensing and Reanalysis. *J. Hydrometeorol.*, **12**, 1221–1254, doi:10.1175/2011JHM1380.1.

Findell, K. L. and E. A. B. Eltahir, 1997: An analysis of the soil moisture–rainfall feedback, based on direct observations from Illinois. *Water. Resour. Res.*, **33**, 725–735, doi:10.1029/96WR03756.

— 2003a: Atmospheric controls on soil moisture–boundary layer interactions. Part I: Framework development. *J. Hydrometeorol.*, **4**, 552–569, doi:10.1175/1525-7541(2003)004<40552:ACOSML>2.0.CO;2.

— 2003b: Atmospheric controls on soil moisture–boundary layer interactions. Part II: Feedbacks within the continental United States. *J. Hydrometeorol.*, **4**, 570–583, doi:10.1175/1525-7541(2003)004<0570:ACOSML>2.0.CO;2.

Findell, K. L., P. Gentine, B. R. Lintner, and C. Kerr, 2011: Probability of afternoon precipitation in eastern United States and Mexico enhanced by high evaporation. *Nat. Geosci.*, **4**, 434–439, doi:10.1038/ngeo1174.

Fink, A. H. and A. Reiner, 2003: Spatiotemporal variability of the relation between African Easterly Waves and West African Squall Lines in 1998 and 1999. *J. Geophys. Res.*, **108**, 4332–4348, doi:10.1029/2002JD002816.

Garcia-Carreras, L., D. J. Parker, and J. H. Marsham, 2011: What is the Mechanism for the

Modification of Convective Cloud Distributions by Land Surface-Induced Flows? *J. Atmos. Sci.*, **68**, 619–634, doi:10.1175/2010JAS3604.1.

Glickman, T., 2000: *Glossary of Meteorology*. Am. Meteorol. Soc., 855 pp.

Goldberg, M., G. Ohring, J. Butler, C. Cao, R. Datla, D. Doelling, V. Gärtner, T. Hewison, B. Iacovazzi, D. Kim, T. Kurino, J. Lafeuille, P. Minnis, D. Renaut, J. Schmetz, D. Tobin, L. Wang, F. Weng, X. Wu, F. Yu, P. Zhang, and T. Zhu, 2011: The Global Space-Based Inter-Calibration System. *B. Am. Meteorol. Soc.*, **92**, 467–475, doi:10.1175/2010BAMS2967.1.

Govaerts, Y. M., S. Wagner, A. Lattanzio, and P. Watts, 2010: Joint retrieval of surface reflectance and aerosol optical depth from MSG/SEVIRI observations with an optimal estimation approach: 1. Theory. *J. Geophys. Res.*, **115**, D02203, doi:10.1029/2009JD011779.

Greuell, W. and R. A. Roebeling, 2009: Toward a Standard Procedure for Validation of Satellite-Derived Cloud Liquid Water Path: A Study with SEVIRI Data. *J. Appl. Meteorol. Clim.*, **48**, 1575–1590, doi:10.1175/2009JAMC2112.1.

Greuell, W., E. van Meijgaard, J. F. Meirink, and N. Clerbaux, 2011: Evaluation of model predicted top-of-atmosphere radiation and cloud parameters over Africa with observations from GERB and SEVIRI. *J. Climate*, **24**, 4015–4036, doi:10.1175/2011JCLI3856.1.

Gruhier, C., P. de Rosnay, S. Hasenauer, T. Holmes, R. de Jeu, Y. Kerr, E. Mougin, E. Njoku, F. Timouk, W. Wagner, and M. Zribi, 2010: Soil moisture active and passive microwave products: intercomparison and evaluation over a Sahelian site. *Hydrol. Earth Syst. Sci.*, **14**, 141–156, doi:10.5194/hess-14-141-2010.

Gruhier, C., P. de Rosnay, Y. Kerr., E. Mougin, E. Ceschia, J.-C. Calvet, and P. Richaume, 2008: Evaluation of AMSR-E soil moisture product based on ground measurements over temperate and semi-arid regions. *Geophys. Res. Lett.*, **35**, doi:10.1029/2008GL033330.

Hagos, S. M. and K. H. Cook, 2007: Dynamics of the West African Monsoon Jump. *J. Climate*, **20**, 5264–5284, doi:10.1175/2007JCLI1533.1.

Hansen, J., R. Ruedy, M. Sato, and K. Lo, 2010: Global surface temperature change. *Rev. Geophys.*, **48**, RG4004, doi:10.1029/2010RG000345.

Hansen, J. E. and J. B. Pollack, 1970: Near-infrared light scattering by terrestrial clouds. *J. Atmos. Sci.*, **27**, 265–281, doi:10.1175/1520-0469(1970)027<0265:NILSBT>2.0.CO;2.

Hansen, J. E., M. Sato, and R. Ruedy, 1997: Radiative forcing and climate response. *J. Geophys. Res.*, **108**, 6831–6864, doi:10.1029/96JD03436.

Hansen, J. E. and L. D. Travis, 1974: Light scattering in planetary atmospheres. *Space Sci. Rev.*, **16**, 527–610.

Held, I. M. and B. J. Soden, 2006: Robust responses of the hydrological cycle to global warming. *J. Climate*, **19**, 5686–5699, doi:10.1175/JCLI3990.1.

Hess, M., R. B. A. Koelemeijer, and P. Stammes, 1998: Scattering matrices of imperfect hexagonal ice crystals. *J. Quant. Spectrosc. Ra.*, **60(3)**, 301–308, doi:10.1016/S0022-4073(98)00007-7.

Hogan, R. J., A. J. Illingworth, J. P. V. Poiares-Baptista, and E. J. O'Connor, 2003: Characteristics of mixed-phase clouds, part II: A climatology from ground-based lidar. *Q. J. Roy. Meteor. Soc.*, **129**, 2117–2134, doi:10.1256/qj.01.209.

Hohenegger, C., P. Brockaus, C. S. Bretherton, and C. Schär, 2009: The soil moisture–precipitation feedback in simulations with explicit and parameterized convection. *J. Climate*, **22**, 5003–5020, doi:10.1175/2009JCLI2604.1.

Hsu, K.-L., X. Gao, S. Sorooshian, and H. V. Gupta, 1997: Precipitation estimation from remotely sensed information using artificial neural networks. *J. Appl. Meteorol.*, **36**, 1176–1190, doi:10.1175/1520-0450(1997)036<1176:PEFRSI>2.0.CO;2.

Huffman, G. J., R. F. Adler, D. T. Bolvin, G. Gu, E. J. Nelkin, K. P. Bowman, Y. Hong, E. F. Stocker, and D. B. Wolff, 2007: The TRMM Multisatellite Precipitation Analysis (TMPA): Quasi-Global, Multiyear, Combined-Sensor Precipitation Estimates at Fine Scales. *J. Hydrometeorol.*, **8**, 38–55, doi:10.1175/JHM560.1.

Huffman, G. J., R. F. Adler, M. M. Morrissey, D. T. Bolvin, S. Curtis, R. Joyce, B. McGavock, and J. Susskind, 2001: Global Precipitation at One-Degree Daily Resolution from Multisatellite Observations. *J. Hydrometeorol.*, **2**, 36–50, doi:10.1175/1525-7541(2001)002<0036:GPAODD>2.0.CO;2.

Iguchi, T., T. Kozu, R. Meneghini, J. Awaka, , and K. Okamoto, 2000: Rain Profiling Algorithm for TRMM Precipitation Radar Data. *J. Appl. Meteorol.*, **39**, 2038–2052, doi:10.1016/S0273-1177(99)00933-3.

Illingworth, A. J., R. J. Hogan, E. J. O'Connor, D. Bouniol, M. E. Brooks, J. Delanoë, D. P. Donovan, J. D. Eastment, N. Gaussiat, J. W. F. Goddard, M. Haeffelin, H. Klein Baltink, O. A. Krasnov, J. Pelon, J.-M. Piriou, A. Protat, H. W. J. Russchenberg, A. Seifert, A. M. Tompkins, G.-J. van Zadelhoff, F. Vinit, U. Willén, D. R. Wilson, and C. L. Wrench, 2007: Cloudnet: Continuous evaluation of cloud profiles in seven operational models using ground-based observations. *B. Am. Meteorol. Soc.*, **88**, 883–898, doi:10.1175/BAMS-88-6-883.

Iwabuchi, H. and T. Hayasaka, 2002: Effects of Cloud Horizontal Inhomogeneity on the Optical Thickness Retrieved from Moderate-Resolution Satellite Data. *J. Atmos. Sci.*, **59**, 2227–2242, doi:10.1175/1520-0469(2002)059<2227:EOCHIO>2.0.CO;2.

Jacobowitz, H., L. L. Stowe, G. Ohring, A. Heidinger, K. Knapp, and N. R. Nalli, 2003: The Advanced Very High Resolution Radiometer Pathfinder Atmosphere (PATMOS) climate dataset: A resource for climate research. *B. Am. Meteorol. Soc.*, **84**, 785–793, doi:10.1175/BAMS-84-6-785.

Janicot, S. and Coauthors, 2008: Large-scale overview of the summer monsoon over

West Africa during the AMMA field experiment in 2006. *Ann. Geophys.*, **26**, 2569–2595, doi:10.5194/angeo-26-2569-2008.

Jobard, I., F. Chopin, J. C. Bergès, and R. Roca, 2010: An intercomparison of 10-day precipitation satellite products during the West African Monsoon. *Int. J. Remote Sens.*, **32**, 2353–2376, doi:10.1080/01431161003698286.

Jolivet, D. and A. J. Feijt, 2005: Quantification of the accuracy of LWP fields derived from NOAA - 16 Advanced Very High Resolution Radiometer over three ground stations using microwave radiometers. *J. Geophys. Res.*, **110**, D11204, doi:10.1029/2004JD005205.

Joyce, R. J., J. E. Janowiak, P. A. Arkin, and P. Xie, 2004: CMORPH: A Method that Produces Global Precipitation Estimates from Passive Microwave and Infrared Data at High Spatial and Temporal Resolution. *J. Hydrometeorol.*, **5**, 487–503, doi:10.1175/1525-7541(2004)005<0487:CAMTPG>2.0.CO;2.

Karlsson, J., G. Svensson, and H. Rodhe, 2008: Cloud radiative forcing of subtropical low level clouds in global models. *Clim. Dyn.*, **30**, 779–788, doi:10.1007/s00382-007-0322-1.

Kawanishi, T., T. Sezai, Y. Ito, K. Imaoka, T. Takeshima, Y. Ishido, A. Shibata, M. Miura, H. Inahata, and R. W. Spencer, 2003: The Advanced Microwave Scanning Radiometer for the Earth Observing System (AMSR-E), NASDA's contribution to the EOS for global energy and water cycle studies. *IEEE T. Geosci. Remote*, **41**, 184–194, doi:10.1109/TGRS.2002.808331.

Kerr, Y. H., P. Waldteufel, J.-P. Wigneron, J. Martinuzzi, J. Font, and M. Berger, 2001: Soil moisture retrieval from space: the Soil Moisture and Ocean Salinity (SMOS) mission. *IEEE T. Geosci. Remote*, **39**, 1729–1735, doi:10.1109/36.942551.

Key, J. R. and J. M. Intrieri, 2000: Cloud particle phase determination with the AVHRR. *J. Atmos. Sci.*, **39**, 1797–1804, doi:10.1175/1520-0450-39.10.1797.

Kidd, C., 2001: Satellite rainfall climatology: a review. *Int. J. Climatol.*, **21**, 1041–1066, doi:10.1002/joc.365.

Kidd, C. and V. Levizzani, 2011: Status of satellite precipitation retrievals. *Hydrol. Earth Syst. Sci.*, **15**, 1109–1116, doi:10.5194/hess-15-1109-2011.

Kiehl, J. T. and K. E. Trenberth, 1997: Earth's annual mean energy budget. *B. Am. Meteorol. Soc.*, **78**, 197–208, doi:10.1175/1520-0477(1997)078<0197:EAGMEB>2.0.CO;2.

Knap, W. H., L. C. Labonnote, G. Brogniez, and P. Stammes, 2005: Modeling total and polarized reflectances of ice clouds: evaluation by means of POLDER and ATSR-2 measurements. *Appl. Optics*, **44**, 4060–4073, doi:10.1364/AO.44.004060.

Knap, W. H., P. Stammes, and R. B. A. Koelemeijer, 2002: Cloud thermodynamic phase determination from near-infrared spectra of reflected sunlight. *J. Atmos. Sci.*, **59**, 83–96, doi:10.1175/1520-0469(2002)059<0083:CTPDFN>2.0.CO;2.

Koster, R. D., P. A. Dirmeyer, Z. Guo, G. Bonan, E. Chan, P. Cos, C. T. Gordon, S. Kanae, E. Kowalczyk, D. Lawrence, P. Liu, C.-H. Lu, S. Malyshev, McAvaney, K. Mitchell, D. Mocko, T. Oki, K. Oleson, A. Pitman, Y.-C. Sud, C. M. Taylor, D. Verseghy, R. Vasic, Y. Xue, and T. Yamada, 2004: Regions of strong coupling between soil moisture and precipitation. *Science*, **305**, 1138–1140, doi:10.1126/science.1100217.

Kummerow, C., W. Barnes, T. Kozu, J. Shuie, and J. Simpson, 1998: The Tropical Rainfall Measuring Mission (TRMM) sensor package. *J. Atmos. Ocean. Technol.*, 809–817, doi:10.1175/1520-0426(1998)015<0809:TTRMMT>2.0.CO;2.

Laing, A. G., J. M. Fritsch, and A. J. Negri, 1999: Contribution of mesoscale convective complexes to rainfall in Sahelian Africa: Estimates from geostationary infrared and passive microwave data. *J. Appl. Meteorol.*, **38**, 957–964, doi:10.1175/1520-0450(1999)038<0957:COMCCT>2.0.CO;2.

Lenderink, G., B. J. J. M. van den Hurk, E. van Meijgaard, A. P. van Ulden, and J. Cuijpers, 2003: Simulation of present-day climate in RACMO2: First results and model developments. Technical report, KNMI WR-252.

Lenderink, G. and E. van Meijgaard, 2008: Increase in hourly precipitation extremes beyond expectations from temperature changes. *Nat. Geosci.*, **1**, 511–514, doi:10.1038/ngeo262.

— 2010: Linking increases in hourly precipitation extremes to atmospheric temperature and moisture changes. *Environ. Res. Lett.*, **5**, doi:10.1088/1748-9326/5/2/025208.

Liao, L. and R. Meneghini, 2009: Validation of TRMM Precipitation Radar through Comparison of Its Multiyear Measurements with Ground-Based Radar. *J. Appl. Meteorol. Clim.*, **48**, 804–817, doi:10.1175/2008JAMC1974.1.

Lin, W. Y. and M. H. Zhang, 2004: Evaluation of clouds and their radiative effects simulated by the NCAR community atmospheric model against satellite observations. *J. Climate*, **17**, 3302–3318, doi:10.1175/1520-0442(2004)017<3302:EOCATR>2.0.CO;2.

Liou, K. N., 2002: *An introduction to atmospheric radiation, Second Edition*. Elsevier Academic Press, San Diego, USA, 583 pp.

Lockwood, M., R. G. Harrison, T. Woollings, and S. K. Solanki, 2010: Are cold winters in Europe associated with low solar activity? *Environ. Res. Lett.*, **5**, doi:10.1088/1748-9326/5/024001.

Loeb, N. G. and J. A. Coakley, 1998: Inference of marine stratus cloud optical depths from satellite measurements: does 1D theory apply? *J. Climate*, **11**, 215–233, doi:10.1175/1520-0442(1998)011<0215:IOMSCO>2.0.CO;2.

Lohmann, U., 2006: Aerosol Effects on Clouds and Climate. *Space Sci. Rev.*, **125**, 129–137, doi:10.1007/s11214-006-9051-8.

Macke, A., D. L. Mitchell, and L. V. Bremen, 1999: Monte Carlo radiative transfer calculations

for inhomogeneous mixed phase clouds. *Phys. Chem. Earth*, **24**, 237–241, doi:10.1016/S1464-1909(98)00044-6.

Marshak, A., S. Platnick, T. Várnai, G. Wen, and R. F. Cahalan, 2006: Impact of three-dimensional radiative effects on satellite retrievals of cloud droplet sizes. *J. Geophys. Res.*, **111**, 9207–9218, doi:10.1029/2005JD006686.

Mathon, V., H. Laurent, and T. Lebel, 2002: Mesoscale Convective System rainfall in the Sahel. *J. Appl. Meteorol.*, **41**, 1081–1092, doi:10.1175/1520-0450(2002)041<1081:MCSRIT>2.0.CO;2.

McCabe, M. F., E. F. Wood, and H. Gao, 2005: Initial soil moisture retrievals from AMSR-E: Multiscale comparison using in situ data and rainfall patterns over Iowa. *Geophys. Res. Lett.*, **32**, doi:10.1029/2004GL021222.

Mecikalsi, J. R. and K. M. Bedka, 2006: Forecasting convective initiation by monitoring the evolution of moving cumulus in daytime GOES imagery. *Mon. Wea. Rev.*, **134**, 49–78, doi:10.1175/MWR3062.1.

Meirink, J. F., R. A. Roebeling, and P. Stammes, 2009: Atmospheric correction for the KNMI Cloud Physical Properties retrieval algorithm. Technical report, KNMI TR-304.

Merchant, C. J., P. Le Borgne, H. Roquet, and A. Marsouin, 2009: Sea surface temperature from a geostationary satellite by optimal estimation. *Remote Sens. Environ.*, **113**, 445–457, doi:10.1016/j.rse.2008.10.012.

Minnis, P., D. P. Garber, D. F. Young, R. F. Arduini, and Y. Takano, 1998: Parameterizations of reflectance and effective emittance for satellite remote sensing of cloud properties. *J. Atmos. Sci.*, **55**, 3313–3339, doi:10.1175/1520-0469(1998)055<3313:PORAEE>2.0.CO;2.

Minnis, P., D. F. Young, B. A. Wielicki, S. Sun-Mack, Q. Z. Trepte, Y. Chen, P. W. Heck, and X. Dong, 2003: A global cloud database from VIRS and MODIS for CERES. *Society of Photo-Optical Instrumentation Engineers (SPIE) Conference Series*, H.-L. Huang, D. Lu, & Y. Sasano, ed., volume 4891, 115–126.

Mittermaier, M. P. and A. J. Illingworth, 2003: Comparison of model-derived and radar-observed freezing-level heights: Implications for vertical reflectivity profile-correction schemes. *Q. J. Roy. Meteor. Soc.*, **129**, 83–95, doi:10.1256/qj.02.19.

Mohr, K. I., 2004: Interannual, monthly, and regional variability in the wet season diurnal cycle of precipitation in Sub-Saharan Africa. *J. Climate*, **17**, 2441–2453, doi:10.1175/1520-0442(2004)017<2441:IMARVI>2.0.CO;2.

Nakajima, T. and M. D. King, 1990: Determination of the optical thickness and effective particle radius of clouds from reflected solar radiation measurements, part 1: Theory. *J. Atmos. Sci.*, **47**, 1878–1893, doi:10.1175/1520-0469(1990)047<1878:DOTOTA>2.0.CO;2.

Nakajima, T. Y. and T. Nakajima, 1995: Wide-Area Determination of Cloud Microphysical

Properties from NOAA AVHRR Measurements for FIRE and ASTEX Regions. *J. Atmos. Sci.*, **52**, 4043–4059, doi:10.1175/1520-0469(1995)052<4043:WADOCM>2.0.CO;2.

Naud, C. M., A. D. Del Genio, and M. Bauer, 2006: Observational constraints on the cloud thermodynamic phase in midlatitude storms. *J. Climate*, **19**, 5273–5288, doi:10.1175/JCLI3919.1.

Negri, A. J. and R. F. Adler, 1993: An intercomparison of three satellite infrared rainfall techniques over Japan and surrounding waters. *J. Appl. Meteorol.*, **32**, 357–373, doi:10.1175/1520-0450(1993)032<0357:AIOTSI>2.0.CO;2.

Negri, A. J., R. F. Adler, and P. J. Wetzel, 1984: Satellite rain estimation: An analysis of the Griffith-Woodley technique. *J. Clim. Appl. Meteor.*, **26**, 1565–1576, doi:10.1175/1520-0450(1984)023<0102:REFSAE>2.0.CO;2.

Nicholson, S. E., B. Some, J. McCollum, E. Nelkin, D. Klotter, Y. Berte, B. M. Diallo, I. Gaye, G. Kpabeba, O. Ndiaye, J. N. Noukpozounkou, M. M. Tanu, A. Thiam, A. A. Toure, and A. K. Traore, 2003: Validation of TRMM and Other Rainfall Estimates with a High-Density Gauge Dataset for West Africa. Part II: Validation of TRMM Rainfall Products. *J. Appl. Meteorol.*, **42**, 1355–1368, doi:10.1175/1520-0450(2003)042<1355:VOTAOR>2.0.CO;2.

Nicholson, S. E., C. J. Tucker, and M. B. Ba, 1998: Desertification, drought, and surface vegetation: an example from the West African Sahel. *B. Am. Meteorol. Soc.*, **79**, 815–829, doi:10.1175/1520-0477(1998)079<0815:DDASVA>2.0.CO;2.

Njoku, E. G., P. Ashcroft, T. K. Chan, and L. Li, 2005: Global survey and statistics of radio-frequency interference in AMSR-E land observations. *IEEE T. Geosci. Remote*, **43**, 938–947, doi:10.1109/TGRS.2004.837507.

Oreopoulos, L. and R. Davies, 1998: Plane parallel albedo biases from satellite observations. part I: Dependence on resolution and other factors. *J. Climate*, **11**, 919–932, doi:10.1175/1520-0442(1998)011<0919:PPABFS>2.0.CO;2.

Oreopoulos, L., S. E. Platnick, G. Hong, P. Yang, and R. F. Cahalan, 2009: The shortwave radiative forcing bias of liquid and ice clouds from MODIS observations. *Atmos. Chem. Phys.*, **9**, 5865–5875, doi:10.5194/acp-9-5865-2009.

Owe, M., R. de Jeu, and T. Holmes, 2008: Multisensor historical climatology of satellite-derived global land surface moisture. *J. Geophys. Res.*, **113**, doi:10.1029/2007JF000769.

Pellarin, T., T. Tran, J.-M. Cohard, S. Galle, J.-P. Laurent, P. de Rosnay, and T. Vischel, 2009: Soil moisture mapping over West Africa with a 30-min temporal resolution using AMSR-E observations and a satellite-based rainfall product. *Hydrol. Earth Syst. Sci.*, **13**, 1887–1896, doi:10.5194/hess-13-1887-2009.

Petty, G. W., 2001: Physical and Microwave Radiative Properties of Precipitating Clouds. Part II: A Parametric 1D Rain-Cloud Model for Use in Microwave Radiative Transfer Simulations. *J. Appl. Meteorol.*, **40**, 2115–2129, doi:10.1175/1520-0450(2001)040<2115:PAMRPO>2.0.CO;2.

Pilewskie, P. and S. Twomey, 1987: Discrimination of ice from water clouds by optical remote sensing. *Atmos. Res.*, **21**, 113–122, doi:10.1016/0169-8095(87)90002-0.

Platnick, S., J. Y. Li, M. D. King, H. Gerber, and P. V. Hobbs, 2001: A solar reflectance method for retrieving the optical thickness and droplet size of liquid water clouds over snow and ice surfaces. *J. Geophys. Res.*, **106**, 15185–15199, doi:10.1029/2000JD900441.

Platnick, S. E., M. D. King, S. A. Ackerman, W. P. Menzel, B. A. Baum, J. C. Riédi, and R. A. Frey, 2003: The MODIS cloud products: Algorithms and examples from Terra. *IEEE T. Geosci. Remote*, **41**, 459–473, doi:10.1109/TGRS.2002.808301.

Pruppacher, H. R. and J. D. Klett, 1997: *Microphysics of Clouds and Precipitation, 2nd rev. and enl. ed.*. Kluwer Academic Publishers, 954 pp.

Ramel, R., H. Gallée, and C. Messager, 2006: On the northward shift of the West African Monsoon. *Clim. Dyn.*, **26**, 429–440, doi:10.1007/s00382-005-0093-5.

Rauber, R. M. and A. Tokay, 1991: An explanation for the existence of supercooled water at the top of cold clouds. *J. Atmos. Sci.*, **48**, 1005–1023, doi:10.1175/1520-0469(1991)048<1005:AEFTEO>2.0.CO;2.

Redelsperger, J., C. D. Thorncroft, A. Diedhiou, T. Lebel, D. J. Parker, and J. Polcher, 2006: African Monsoon Multidisciplinary Analysis: An International Research Project and Field Campaign. *B. Am. Meteorol. Soc.*, **87**, 1739–1746, doi:10.1175/BAMS-87-12-1739.

Riédi, J. C., P. Goloub, and R. T. Marchand, 2001: Comparison of POLDER cloud phase retrievals to active remote sensor measurements at the ARM SGP site. *Geophys. Res. Lett.*, **28**, 2185–2188, doi:10.1029/2000GL012758.

Roca, R., P. Chambon, I. Jobard, P.-E. Kirstetter, M. Gosset, and J.-C. Bergès, 2010: Comparing satellite and surface rainfall products over West Africa at meteorologically relevant scales during the AMMA campaign using error estimates. *J. Appl. Meteorol. Clim.*, **49**, 715–731, doi:10.1175/2009JAMC2318.1.

Roebeling, R. A., A. Berk, A. J. Feijt, W. Frerichs, D. Jolivet, A. Macke, and P. Stammes, 2005: Sensitivity of cloud property retrievals to differences in radiative transfer simulations. Technical report, KNMI WR 2005-02.

Roebeling, R. A., H. M. Deneke, and A. J. Feijt, 2008: Validation of Cloud Liquid Water Path Retrievals from SEVIRI Using One Year of CloudNET Observations. *J. Appl. Meteorol. Clim.*, **47**, 206–222, doi:10.1175/2007JAMC1661.1.

Roebeling, R. A., A. J. Feijt, and P. Stammes, 2006a: Cloud property retrievals for climate monitoring: Implications of differences between Spinning Enhanced Visible and Infrared Imager (SEVIRI) on METEOSAT-8 and Advanced Very High Resolution Radiometer (AVHRR) on NOAA-17. *J. Geophys. Res.*, **111**, doi:10.1029/2005JD006990.

Roebeling, R. A. and I. Holleman, 2009: Validation of rain rate retrievals from SEVIRI using weather radar observations. *J. Geophys. Res.*, **114**, doi:10.1029/2009JD12102.

Roebeling, R. A., N. A. J. Schutgens, and A. J. Feijt, 2006b: Analysis of uncertainties in SEVIRI cloud property retrievals for climate monitoring. *AMS Cloud Phys. Rad. Conf.*, Am. Meteor. Soc., Madison, WI, CD–ROM, P4.51.

Roebeling, R. A. and E. van Meijgaard, 2009: Evaluation of the Daylight Cycle of Model-Predicted Cloud Amount and Condensed Water Path over Europe with Observations from MSG SEVIRI. *J. Climate*, **22**, 1749–1766, 10.1175/2008JCLI2391.1.

Roelofs, G.-J. and S. Jongen, 2004: A model study of the influence of aerosol size and chemical properties on precipitation formation in warm clouds. *J. Geophys. Res.*, **109**, doi:10.1029/2004JD004779.

Rosenfeld, D., E. Cattani, S. Melani, and V. Levizzani, 2004: Considerations on Daylight Operation of 1.6- versus 3.7-$\mu$m Channel on NOAA and Metop Satellites. *B. Am. Meteorol. Soc.*, **85**, 873–881, doi:10.1175/BAMS-85-6-873.

Rosenfeld, D. and G. Gutman, 1994: Retrieving microphysical properties near the tops of potential rain clouds by multispectral analysis of AVHRR data. *Atmos. Res.*, **34**, 259–284, doi:10.1016/0169-8095(94)90096-5.

Rosenfeld, D. and I. M. Lensky, 1998: Satellite-based insights into precipitation formation processes in continental and maritime convective clouds. *B. Am. Meteorol. Soc.*, **79**, 2457–2476, doi:10.1029/2004JD004779.

Rosenfeld, D. and Y. Mintz, 1988: Evaporation of Rain Falling from Convective Clouds as Derived from Radar Measurements. *J. Appl. Meteorol.*, **27**, 209–215, doi:10.1175/1520-0450(1988)027<0209:EORFFC>2.0.CO;2.

Rossow, W. B. and R. A. Schiffer, 1999: Advances in understanding clouds from ISCCP. *B. Am. Meteorol. Soc.*, **80**, 2261–2287, doi:10.1175/1520-0477(1999)080<2261:AIUCFI>2.0.CO;2.

Rudolf, B., 1993: Management and analysis of precipitation data on a routine basis. Technical report, Proc. Int. WMO/IAHS/ETH Symp. on Precipitation and Evaporation, Bratislava, Slovakia, Slovak Hydrometeorology Institute.

Sapiano, M. R. P. and P. A. Arkin, 2009: An Intercomparison and Validation of High-Resolution Satellite Precipitation Estimates with 3-Hourly Gauge Data. *J. Hydrometeorol.*, **10**, 149–166, doi:10.1175/2008JHM1052.1.

Schiffer, R. A. and W. B. Rossow, 1983: The International Satellite Cloud Climatology Project (ISCCP) - The first project of the World Climate Research Programme. *B. Am. Meteorol. Soc.*, **64**, 779–784.

Schmetz, J., P. Pili, S. Tjemkes, D. Just, J. Kerkmann, S. Rota, and A. Ratier, 2002: An Introduction

to Meteosat Second Generation (MSG). *B. Am. Meteorol. Soc.*, **83**, 977–992, doi:10.1175/1520-0477(2002)083<0977:AITMSG>2.3.CO;2.

Schulz, J., P. Albert, H. D. Behr, D. Caprion, H. Deneke, S. Dewitte, B. Dürr, P. Fuchs, A. Gratzki, P. Hechler, R. Hollmann, S. Johnston, K.-G. Karlsson, T. Manninen, R. Müller, M. Reuter, A. Riihelä, R. Roebeling, N. Selbach, A. Tetzlaff, W. Thomas, M. Werscheck, E. Wolters, and A. Zelenka, 2009a: Operational climate monitoring from space: the EUMETSAT Satellite Application Facility on Climate Monitoring (CM-SAF). *Atmos. Chem. Phys.*, **9**, 1687–1709, doi:10.5194/acp-9-1687-2009.

Schulz, J., A. Devasthale, R. Hollmann, K. G. Karlsson, M. Lockhoff, J. F. Meirink, and R. A. Roebeling, 2009b: Annual validation report 2008. *SAF/CM/DWD/VAL/OR4*, 68 pp., available from http://www.cmsaf.eu.

Schutgens, N. A. J. and R. A. Roebeling, 2009: Validating the Validation: The Influence of Liquid Water Distribution in Clouds on the Intercomparison of Satellite and Surface Observations. *J. Atmos. Ocean. Technol.*, **26**, 1457–1474, doi:10.1175/2009JTECHA1226.1.

Solomon, S., D. Qin, M. Manning, Z. Chen, M. Marquis, K. B. Averyt, M. Tignor, and H. L. Miller, eds., 2007: *Climate Change 2007: The Physical Science basis. Contribution of Working Group I to the Fourth Assessment Report of the Intergovernmental Panel on Climate Change*. Cambridge Univ. Press, Cambridge (United Kingdom) and New York (USA), 996 pp.

Sorooshian, S., K.-L. Hsu, X. Gao, H. V. Gupta, B. Imam, and D. Braithwaite, 2000: Evaluation of PERSIANN system satellite-based estimates of tropical rainfall. *B. Am. Meteorol. Soc.*, **81**, 2035–2046, doi:10.1175/1520-0477(2000)081<2035:EOPSSE>2.3.CO;2.

Stammes, P., 2001: Spectral radiance modelling in the UV-Visible range. *Int. Rad. Symp.*, W. L. Smith and Y. M. Timofeyev, eds., A. Deepak, Hampton, VA, 385–388.

Stamnes, K., S. C. Tsay, W. Wiscombe, and K. Jayaweera, 1988: Numerically stable algorithm for discrete-ordinate-method radiative transfer in multiple scattering and emitting layered media. *Appl. Optics*, **27**, 2502–2509, doi:10.1364/AO.27.002502.

Stengel, M., P. Undén, M. Lindskop, P. Dahlgren, N. Gustafsson, and R. Bennartz, 2009: Assimilation of SEVIRI infrared radiances with HIRLAM 4D-Var. *Q. J. Roy. Meteor. Soc.*, **135**, 2100–2109, doi:10.1002/qj.501.

Stephens, G. L., 1978: Radiation Profiles in Extended Water Clouds. II: Parameterization Schemes. *J. Atmos. Sci.*, **35**, 2123–2132, doi:10.1175/1520-0469(1978)035<2123:RPIEWC>2.0.CO;2.

Stephens, G. L. and J. M. Haynes, 2007: Near global observations of the warm rain coalescence process. *Geophys. Res. Lett.*, **34**, doi:10.1029/2007GL030259.

Stephens, G. L. and Y. Hu, 2010: Are climate-related changes to the character of global-mean precipitation predictable? *Environ. Res. Lett.*, **5**, doi:10.1088/1748-9326/5/2/025209.

Stephens, G. L. and C. D. Kummerow, 2007: The Remote Sensing of Clouds and Precipitation from Space: A Review. *J. Atmos. Sci.*, **64**, 3742–3765, doi:10.1175/2006JAS2375.1.

Stephens, G. L., D. G. Vane, R. J. Boain, G. G. Mace, H. Sassen, Z. Wang, A. J. Illingworth, E. J. O'Connor, W. B. Rossow, S. L. Durden, S. D. Miller, R. T. Austin, A. Benedetti, C. Mitrescu, and the Cloudsat Team, 2002: The CloudSat mission and the A-train. *B. Am. Meteorol. Soc.*, **83**, 1771–1790, doi:10.1175/BAMS-83-12-1771.

Strabala, K. I., S. A. Ackerman, and W. P. Menzel, 1994: Cloud properties inferred from 8-12 $\mu$m data. *J. Appl. Meteorol.*, **33**, 212–229, doi:10.1175/1520-0450(1994)033<0212:CPIFD>2.0.CO;2.

Su, Z., 2002: The surface energy balance system (SEBS) for estimation of turbulent heat fluxes. *Hydrol. Earth Syst. Sci.*, **6**, 85–100, doi:10.5194/hess-6-85-2002.

Su, Z., W. Dorigo, D. Fernández-Prieto, M. Van Helvoirt, K. Hungershöfer, R. de Jeu, R. Parinussa, J. Timmermans, R. Roebeling, M. Schröder, J. Schulz, C. Van der Tol, P. Stammes, W. Wagner, L. Wang, P. Wang, and E. Wolters, 2010: Earth observation Water Cycle Multi-Mission Observation Strategy (WACMOS). *Hydrol. Earth Syst. Sci. Discuss.*, **7**, 7899–7956, doi:10.5194/hessd-7-7899-2010.

Sultan, B. and S. Janicot, 2003: The West African Monsoon Dynamics. Part II: The 'Preonset' and 'Onset' of the Summer Monsoon. *J. Climate*, **16**, 3407–3427, doi:10.1175/1520-0442(2003)016<3407:TWAMDP>2.0.CO;2.

Sultan, B., S. Janicot, and P. Drobinski, 2007: Characterization of the diurnal cycle of the West African Monsoon around the monsoon onset. *J. Climate*, **20**, 4014–4032, doi:10.1175/JCLI4218.1.

Szczodrak, M., P. H. Austin, and P. B. Krummel, 2001: Variability of Optical Depth and Effective Radius in Marine Stratocumulus Clouds. *J. Atmos. Sci.*, **58**, 2912–2926, doi:10.1175/1520-0469(2001)058<2912:VOODAE>2.0.CO;2.

Szyndel, M. D. E., G. Kelly, and Thépaut, 2005: Evaluation of potential benefit of SEVIRI water vapour radiance data from Meteosat-8 into global numerical weather prediction analyses. *Atmos. Res. Lett.*, **6**, 105–111, doi:10.1002/asl.98.

Tao, W.-K., X. Li, A. Khain, T. Matsui, S. Lang, and J. Simpson, 2007: Role of atmospheric aerosol concentration on deep convective precipitation: Cloud resolving model simulations. *J. Geophys. Res.*, **112**, doi:10.1029/2007JD008728.

Taylor, C. M. and R. J. Ellis, 2006: Satellite detection of soil moisture impacts on convection at the mesoscale. *Geophys. Res. Lett.*, **33**, doi:10.1029/2005GL025252.

Taylor, C. M., A. Gounou, F. Guichard, P. P. Harris, R. J. Ellis, F. Couvreux, and M. de Kauwe, 2011: Frequency of Sahelian storm initiation enhanced over mesoscale soil-moisture patterns. *Nat. Geosci.*, **4**, 430–433, doi:10.1038/ngeo1173.

Taylor, C. M., P. P. Harris, and D. J. Parker, 2010: Impact of soil moisture on the development of a Sahelian mesoscale convective system: a case-study from the AMMA special observing period. *Q. J. Roy. Meteor. Soc.*, **136**, 456–470, doi:10.1002/qj.465.

Taylor, C. M., E. F. Lambin, N. Stephenne, R. J. Harding, and R. L. H. Essery, 2002: The Influence of Land Use Change on Climate in the Sahel. *J. Climate*, **15**, 3615–3629, doi:10.1175/1520-0442(2002)015<3615:TIOLUC>2.0.CO;2.

Taylor, C. M., D. J. Parker, and P. P. Harris, 2007: An observational case study of mesoscale atmospheric circulations induced by soil moisture. *Geophys. Res. Lett.*, **34**, doi:10.1029/2007GL030572.

Thies, B., T. Nauß, and J. Bendix, 2008: Precipitation process and rainfall intensity differentiation using Meteosat Second Generation Spinning Enhanced Visible and Infrared Imager data. *J. Geophys. Res.*, **113**, doi:10.1029/2008JD010464.

Thomas, G. E., S. M. Dean, E. Carboni, R. G. Grainger, C. A. Poulsen, R. Siddans, and B. J. Kerridge, 2007: An optimal estimation aerosol retrieval scheme for (A)ATSR. Technical report, Technical Memorandum University of Oxford.

Tian, Y., C. D. Peters-Lidard, R. F. Adler, T. Kubota, and T. Ushio, 2010: Evaluation of GSMAP Precipitation Estimates over the Contiguous United States. *J. Hydrometeorol.*, **11**, 566–574, doi:10.1175/2009JHM1190.1.

Tian, Y., C. D. Peters-Lidard, B. J. Choudhury, and M. Garcia, 2007: Multitemporal Analysis of TRMM-Based Satellite Precipitation Products for Land Data Assimilation Applications. *J. Hydrometeorol.*, **8**, 1165–1183, doi:10.1175/2007JHM859.1.

Trenberth, K. E., J. T. Fasullo, and J. T. Kiehl, 2009: Earth's global energy budget. *B. Am. Meteorol. Soc.*, **90**, 311–323, doi:10.1175/2008BAMS2634.1.

Trenberth, K. E., L. Smith, T. Qian, A. Dai, and J. Fasullo, 2007: Estimates of the global water budget and its annual cycle using observational and model data. *J. Hydrometeorol.*, **8**, 758–769, doi:10.1175/JHM600.1.

Turner, D. D., 2005: Arctic mixed-phase cloud properties from AERI lidar observations: algorithm and results from SHEBA. *J. Appl. Meteorol.*, **44**, 427–444, doi:10.1175/JAM2208.1.

Turner, D. D., S. A. Ackerman, B. A. Baum, P. E. Rivercombe, and P. Yang, 2003: Cloud phase determination using ground-based AERI observations at SHEBA. *J. Appl. Meteorol.*, **42**, 701–715, doi:10.1175/1520-0450(2003)042<0701:CPDUGA>2.0.CO;2.

van de Hulst, H. C., 1980: *Multiple light scattering, Tables, Formulas, and Applications, Vols. 1 and 2*. Academic Press, New York, 722 pp.

van den Hurk, B. J. J. M. and E. van Meijgaard, 2010: Diagnosing Land–Atmosphere interaction from a regional climate model simulation over West Africa. *J. Hydrometeorol.*, **11**, 467–481,

doi:10.1175/2009JHM1173.1.

Wagner, W., G. Lemoine, and H. Rott, 1999: A method for estimating soil moisture from ERS scatterometer and soil data. *Remote Sens. Environ.*, **70**, 191–207, doi:10.1016/S0034-4257(99)00036-X.

Wang, M. and J. E. Overland, 2009: A sea ice free summer Arctic within 30 years? *Geophys. Res. Lett.*, **36**, 7502–7506, doi:10.1029/2009GL037820.

Warren, S. G., 1984: Optical constants of ice from the ultraviolet to the microwave. *Appl. Optics*, **23**, 1206–1225, doi:10.1364/AO.23.001206.

Weidle, F. and H. Wernli, 2008: Comparison of ERA40 cloud top phase with POLDER-1 observations. *J. Geophys. Res.*, **113**, doi:10.1029/2007JD009234.

Wentz, F. J. and R. W. Spencer, 1998: SSM/I rain retrievals within a unified all-weather ocean algorithm. *J. Atmos. Sci.*, **55**, 1613–1627, doi:10.1175/1520-0469(1998)055<1613:SIRRWA>2.0.CO;2.

Wolters, D., C. C. van Heerwaarden, J. Vilá-Guerau de Arellano, B. Cappelaere, and D. Ramier, 2010a: Effects of soil moisture gradients on the path and the intensity of a West African squall line. *Q. J. Roy. Meteor. Soc.*, **136**, 2162–2175, doi:10.1002/qj.712.

Wolters, E. L. A., H. M. Deneke, B. J. J. M. van den Hurk, J. F. Meirink, and R. A. Roebeling, 2010b: Broken and inhomogeneous cloud impact on satellite cloud particle effective radius and cloud-phase retrievals. *J. Geophys. Res.*, **115**, doi:10.1029/2009JD012205.

Wolters, E. L. A., R. A. Roebeling, and A. J. Feijt, 2008: Evaluation of cloud-phase retrieval methods for SEVIRI on Meteosat-8 using ground-based lidar and cloud radar data. *J. Appl. Meteorol. Clim.*, **47**, 1723–1738, doi:10.1175/2007JAMC1591.1.

Wolters, E. L. A., R. A. Roebeling, and P. Stammes, 2006: Cloud reflectance calculations using DAK: study on required integration points. Technical report, KNMI TR-292.

Wolters, E. L. A., B. J. J. M. van den Hurk, and R. A. Roebeling, 2011: Evaluation of rainfall retrievals from SEVIRI reflectances using TRMM-PR and CMORPH. *Hydrol. Earth Syst. Sci.*, **15**, 437–451, doi:10.5194/hess-15-437-2011.

Xiong, X., A. Wu, B. Wenny, J. Choi, and A. Angal, 2011: Progress and lessons from MODIS calibration intercomparison using ground test sites. *Can. J. Remote Sens.*, **36**, 540–552, doi:10.5589/m10-082.

Yamaguchi, Y. T., Y. Yokoyama, H. Miyahara, and T. Nakatsuka, 2010: Synchronized Northern Hemisphere climate change and solar magnetic cycles during the Maunder Minimum. *Proc. Natl. Acad. Sci.*, **107**, 20697–20702, doi:10.1073/pnas.1000113107.

Yang, S. and E. A. Smith, 2006: Mechanisms for diurnal variability of global tropical rainfall observed from TRMM. *J. Climate*, **19**, 5190–5226, doi:10.1175/JCLI3883.1.

Zinner, T., H. Mannstein, and A. Tafferner, 2008: Cb-TRAM: Tracking and monitoring severe convection from onset over rapid development to mature phase using multi-channel Meteosat-8 SEVIRI data. *Meteorol. Atmos. Phys.*, **101**, 191–210, 10.1007/s00703-008-0290-y.

Zinner, T. and B. Mayer, 2006: Remote sensing of stratocumulus clouds: Uncertainties and biases due to inhomogeneity. *J. Geophys. Res.*, **111**, 14209–14222, doi:10.1029/2005JD006955.

Zribi, M., M. Pardé, P. De Rosnay, F. Baup, N. Boulain, L. Descroix, T. Pellarin, E. Mougin, C. Ottlé, and B. Decharme, 2009: ERS scatterometer surface soil moisture analysis of two sites in the south and north of the Sahel region of West Africa. *J. Hydrol.*, **375**, 253–261, doi:10.1016/j.jhydrol.2008.11.046.

# Dankwoord

Toen ik eind 1999 een aanbod voor een functie in de ICT aanvaardde, leek op dat moment een terugkeer naar de meteorologie ver weg, laat staan dat ik toen dacht aan een promotie. Toch begon gaandeweg mijn werkzaamheden als programmeur het besef te groeien dat ik op termijn zou terugkeren naar mijn vakgebied, hetgeen in 2002 dan ook geschiedde. Na een tweetal jaren als meteoroloog in de Centrale Weerkamer van het KNMI maakte ik in april 2004 de overstap naar het klimaatonderzoek. Dit nadat ik werd getipt over een vrije positie bij de toenmalige afdeling Atmosferisch Onderzoek. Na een verkennend gesprek met afdelingshoofd Arnout Feijt over de inhoud van de werkzaamheden binnen de Climate Monitoring Satellite Application Facility (CM-SAF) was mijn interesse gewekt. Ik sprak de ambitie uit om niet alleen projectwerkzaamheden te doen, maar ook om aan een promotie te werken. Toen dit geregeld was, sprak Arnout de profetische woorden: "Zo, jij mag ook die berg gaan beklimmen...". Arnout, bedankt voor het bieden van deze mogelijkheid en de begeleiding bij de wankele eerste stappen als onderzoeker.

De eerste jaren bestond het SEVIRI-wolkenonderzoeksgroepje uit twee personen: mijn co-promotor Rob Roebeling en ondergetekende. Van Rob heb ik gaandeweg steeds meer kneepjes van het onderzoeksvak geleerd, ondanks zijn vaak drukke werkzaamheden stond hij altijd klaar om de nieuwe en niet altijd even begrijpelijke resultaten te bekijken, te becommentariëren en suggesties voor nieuwe onderzoeksrichtingen te doen. Vooral op het gebied van doel- en toepassingsgericht werken, dataverwerking en het helder en beknopt opschrijven van resultaten heb ik een hoop van hem geleerd. Gedurende mijn verblijf bij de afdeling Atmosferisch Onderzoek (later Regionaal Klimaat) en Aardobservatie Klimaat is de wolkengroep flink gegroeid en heb ik verder prettig samengewerkt met Hartwig Deneke, Wouter Greuell, Jan Fokke Meirink, Ping Wang, Paul de Valk, Bastiaan Jonkheid en Brent Maddux.

Het eerste jaar was formeel Bert Holtslag mijn promotor, eenvoudigweg omdat het ook Rob's promotor was. Bert was echter van mening dat het voor mij als beginnende promovendus beter was wanneer ik een promotor had die zich zowel inhoudelijk als fysiek op kortere afstand bevond. Bert, bedankt voor deze suggestie! Nadat ik Bart van den Hurk bereid had gevonden mij onder zijn hoede te nemen, heeft deze een grote rol gespeeld in mijn ontwikkeling als onderzoeker en dan vooral in het opstellen van een goede hypothese voordat ik aan een onderzoek begon. Ik wil Bart bedanken voor het geduldig wachten op nieuwe of verbeterde

teksten en resultaten, om deze vervolgens kritisch te beoordelen en mij te stimuleren om nog een stapje extra te doen. Nooit heeft hij harde woorden laten vallen wanneer ik andermaal om een paar dagen/weken uitstel vroeg omdat ik een onderzoek te optimistisch had benaderd en het genereren van resultaten en/of het beschrijven ervan langer duurde dan gepland.

Iemand wiens bijdrage aan dit proefschrift alleen maar onderschat kan worden is die van Piet Stammes. De beginselen van het stralingstransport werden geduldig en begrijpelijk door Piet steeds weer uitgelegd en -getekend. Daarbij heeft hij ook een belangrijke rol gespeeld als promovenduscoach. Zeker in het laatste jaar, toen er nog een theoretisch hoofdstuk, een laatste inhoudelijke hoofdstuk én de perspectives geschreven moesten worden, heeft hij er steeds voor gezorgd dat ik mijn focus bleef houden en had hij altijd een stimulerend woordje paraat.

Het groeien tot een volwaardig onderzoeker is een pad vol oneffenheden, waarbij de eerste paar jaar soms een harde leerschool zijn, omdat je je een weg moet zien te vinden in hoe zinvolle resultaten te verkrijgen uit enorme hoeveelheden data. Mijn eerste kamergenoot, Gerd-Jan van Zadelhoff, heeft ruim 3 jaar daarin een belangrijke rol gespeeld door me een boel IDL-kennis bij te brengen, mee te denken en door een luisterend oor te bieden wanneer het niet helemaal meezat c.q. tegenzat. Zijn goed gevoel voor (bij tijden cynische) humor plaatste vaak alles in het juiste perspectief. Het jarenlange verblijf op de derde verdieping van het B-gebouw werd tussen de bedrijven door verder veraangenaamd door de fijne collega's van Regionaal Klimaat: Wouter ("Gutenmorgen Herrschaften!") Knap (vooral voor het moeten aanhoren van mijn flauwe woordgrappen), Dave, Martin, Janneke, Irene, Roeland, Bert, Roel, Geert, Erik en Bastiaan. Ook de collega's bij Aardobservatie Klimaat wil ik bedanken voor hun steun, interesse en gezellige koffiepraatjes: onder andere Jos, Folkert, Gijs, Ronald, Bas, Tim, Piet, Pieternel, Jacqueline en Maarten (de laatste vooral ook voor alle LaTeX tips and tricks), bedankt!

Na Gerd-Jan was Jan Fokke mijn volgende kamergenoot. Hoewel er steevast hard werd gewerkt, werd het begin van de maandagochtend, onder het genot van een bakje koffie of cappuccino (dat mag tot 11 uur...), steevast ingeruimd voor een analyse van het afgelopen eredivisieweekend, waarbij soms de deskundige analisten Wouter en Folkert aanschoven en hun licht over de wedstrijden lieten schijnen. Als er geen voetbal te analyseren viel, dan wel wielrennen, tennis, schaatsen of een andere sport. Als nuchtere Friese kamergenoot heeft Jan Fokke vele versies van mijn schrijfsels gecorrigeerd en heb ik zeer prettig het CM-SAF werk voortgezet.

For more than seven years I have worked on the CM-SAF. Karl-Göran, Joe, Abhay, Anke (all SMHI), Martin, Maarit, Anke, Rainer, and Frank (all DWD), it has been a pleasure working with you! I especially appreciate Karl-Göran attending my defense, I look forward sharing some beers and some updates on the latest progressive rock developments! I also want to acknowledge the project colleagues from WACMOS: Joris, Marcel, Christiaan, Bob (all ITC Enschede), Wouter (TU Vienna), Richard, Robert (both VU Amsterdam), Jörg (then DWD, now EUMETSAT), Marc, Katja (both DWD), and Diego (ESA). We achieved quite a lot in a rather short period and I especially remember the good project meetings, which were followed by good dinners and drinks.

A big ‘thank you’ is certainly there for Bryan Baum, who invited me early 2008 to come to Madison for a five-week visit to work on some MODIS stuff. It was really nice having you as my supervisor during those weeks and I feel honored that you accepted to be a member of the evaluation committee. Your slogan is ‘work hard, play hard’, which meant that the hard work at the Space Science and Engineering Center was sometimes (or should I say regularly?) interrupted to have a coffee at the Union South, a discussion about life, the universe, and music, or biking to the Bratfest. Weatherwise, it was also a very good stay, with lots of severe thunderstorms and nearby tornadoes during the last week, a very special experience! Also the other colleagues, Andy, Mike, Bob, Dave, Sarah, and Pat, thank you for the stimulating discussions, the beers, and the running (even up to 10 km during working time...). Iliana, thank you for sharing your house and car for my weekend trips.

Muziek is voor mij altijd een goede uitlaatklep geweest en met plezier denk ik dan ook terug aan de jamsessies met Remy in Haarlem/IJmuiden. Hoeveel materiaal staat er ondertussen wel niet op disk? Ook op het KNMI heb ik zeer geregeld tijdens de lunchpauze muzikaal aan de weg getimmerd in het Rockhok met Bert, Nico, Martin, en Siebren. Het hoogtepunt was toch wel het nooit meer geëvenaarde optreden tijdens de kerstborrel van 2005. Ook mijn vrienden en familie wil ik bedanken voor hun steun, relativerende woorden en interesse over de voortgang van het promotietraject. Mijn neef Mark wil ik bedanken voor het bezoeken van rockconcerten, lezingen en al het andere interessants dat op ons pad komt. Martijn, we hebben in dik 20 jaar al aardig wat tennispotjes tegen elkaar gespeeld, waarbij de constante factor is dat we aan het eind van de wedstrijd moeten constateren dat er aan ons twee tennistalenten verloren zijn gegaan, iets wat steeds minder strookt met ons vertoonde spel. Kosta, je nuchtere en humoristische kijk op de zaken hebben zeker haar uitwerking gehad gedurende deze periode. We moeten binnenkort maar weer eens ouderwets Italiaans gaan tafelen “in de buurt” van Bergamo. Ralph, het gezellige stappen in Maastricht hebben we al een aardige tijd ingeruild voor bier/wijn en goede gesprekken in de huiselijke omgeving, maar de gezelligheid en droge humor blijven. Inge, super dat je je broer bijstaat als paranimf, als zus ben je voor mij een belangrijke steunpilaar geweest. Ook haar vriend Mark wil ik danken voor alle steun en interesse. Verder dank aan andere familieleden: Hub, Marleen, Jo, Lenie, Hans, Antoinette, Hub en Truus. Pap en mam, ut mènke det es kindj altied nao de lóch mos kieke en mit ut waer bezig woor haet unne lange waeg bewanjeldj, maar haet ut noe eindelijk aaf. Christel, dank voor het luisterend oor en begrip wanneer het eens niet meezat en er weer de nodige avonden thuis moest worden doorgewerkt. Lars, kleine boef, je zult straks aardig onder de indruk zijn van het hele gebeuren, ik ben benieuwd welk pad jij gaat bewandelen!

## Curriculum vitae

Erwin Leonardus Antonius Wolters werd geboren op 1 februari 1976 in Roermond en groeide op in het iets zuidelijker gelegen Linne. Na het doorlopen van de lagere school ging hij in 1988 naar het Bisschoppelijk College Schöndeln in Roermond, waar in 1994 het Atheneum-B diploma werd behaald. Dit opende de weg voor een studie Bodem, Water en Atmosfeer aan de toenmalige Landbouwuniversiteit in Wageningen. In 1999 studeerde hij af in de specialisatie meteorologie met scripties in de grenslaagmeteorologie (low-level jet in de stabiele nachtelijke grenslaag) en agrometeorologie (koppeling van een gewasklimaatsmodel aan een plantenziektenmodel bij DLV Meteo, het huidige Weeronline). Het vele programmeerwerk bij DLV Meteo beviel goed en een uitstapje van 2 1/2 jaar naar de ICT-wereld volgde. Het bloed kruipt echter waar het niet gaan kan en in mei 2002 keerde hij terug naar het vakgebied en werd hij meteoroloog in de Centrale Weerkamer van het KNMI. In april 2004 volgde een overstap naar de sector Klimaat en Seismologie van het KNMI als wetenschappelijk projectmedewerker. Hier werkte hij tot en met 2011 voor de Climate Monitoring Satellite Application Facility (CM-SAF) en tevens in 2009 en 2010 voor het Water Cycle Multi-Mission Observation Strategy (WACMOS) project. Naast deze projectwerkzaamheden werd de gelegenheid geboden om aan een promotie te werken, hetgeen in het voorgaande is beschreven. Sinds 1 februari 2012 werkt hij bij de afdeling Klimaatdata en -Advies in het Generator of Rainfall and Discharge Extremes (GRADE) project aan de extremenstatistiek van neerslag in de stroomgebieden van Rijn en Maas.